

ABSTRACT

Title of Document: LANTHANOID ISOTOPIC COMPOSITION OF
PRE AND POST-DETONATION NUCLEAR
MATERIAL

Nicholas Eugene Sharp, Doctor of Philosophy, 2014

Directed By: Professor Alice C. Mignerey, Chemistry and
Biochemistry
Professor William F. McDonough, Geology

Analysis of lanthanoid isotopic composition of pre and post-nuclear detonation materials provides information on the type of device, origin of fissile material, and in the case of spent nuclear fuel, the operating history of the reactor. Prior to analysis, the lanthanoids must be separated from bulk materials to reduce exposure to harmful radiation and to remove isobaric interferences. Trinitite and spent nuclear fuel rods are appropriate analogues for post and pre-detonation nuclear materials, respectively. Compositional analysis of trinitite glass, fused silicate material produced by the Trinity test, reveal non-normal Nd isotope composition, with deviations of $-1.66 \pm 0.48 \text{ } \epsilon$ (differences in parts in 10^4) in $^{142}\text{Nd}/^{144}\text{Nd}$, $+2.24 \pm 0.32 \text{ } \epsilon$ in $^{145}\text{Nd}/^{144}\text{Nd}$, and $+1.00 \pm 0.66 \text{ } \epsilon$ in $^{148}\text{Nd}/^{144}\text{Nd}$ (2σ) relative to natural reference materials. Greater isotopic deviations are found in Gd, with enrichments of $+4.28 \pm 0.72 \text{ } \epsilon$ in $^{155}\text{Gd}/^{160}\text{Gd}$, $+4.19 \pm 0.56 \text{ } \epsilon$ in $^{156}\text{Gd}/^{160}\text{Gd}$, and $+3.59 \pm 0.37 \text{ } \epsilon$ in $^{158}\text{Gd}/^{160}\text{Gd}$. The isotopic deviations are consistent with a ^{239}Pu based fission device

with additional ^{235}U fission contribution and a thermal neutron fluence between 0.97 and 1.4×10^{15} neutrons/cm².

Separation and analysis of spent nuclear material is a difficult challenge in both logistics and sample handling. Lanthanoids were removed from the bulk spent nuclear fuel at Savannah River National Laboratories, while the separation of Gd, Sm and Nd was carried out at the University of Maryland. The isotopic composition of Nd and Sm were compared to predicted values calculated using two programs that were developed for modeling the burning cycle of traditional power-reactors: Oak Ridge Isotope GENERation (ORIGEN-S) and Monte Carlo N-particle transport code (MONTEBURNS). The isotopic composition of Nd agreed with predicted values within 10% with the exception of ^{142}Nd , while only ^{150}Sm had agreement within 10% of prediction. These results show that the typical calculation codes are not adequately modeling the intense neutron flux present in research reactors, and further work will need to be done before source reactors can be identified using reverse modeling algorithms.

LANTHANOID ISOTOPIC COMPOSITION OF PRE AND POST-DETONATION
NUCLEAR MATERIAL

By

Nicholas Eugene Sharp

Dissertation submitted to the Faculty of the Graduate School of the
University of Maryland, College Park, in partial fulfillment
of the requirements for the degree of
Doctor of Philosophy
2014

Advisory Committee:
Professor Alice C. Mignerey Chair
Professor William F. McDonough
Dr. Brian W. Ticknor
Professor William Walters
Professor Andrei Vedernikov
Dean's Representative Professor Richard J. Walker

© Copyright by
Nicholas Eugene Sharp
2014

Preface

The work presented in this dissertation was completed between August 2009 and March 2014 during my tenure as a graduate student in the Department of Chemistry and Biochemistry at University of Maryland, with the summers of 2011 through 2013 spent at the Nuclear Forensics Technical Center at Savannah River National Laboratory. The chemistry and analyses for trinitite from Chapter 4 were conducted by coauthors in that paper. The chemistry performed on the bulk spent nuclear fuel rods was performed by technicians under my observation at the Shielded Cells Facility at Savannah River National Laboratory. All other chemistry and analyses were conducted by myself at the University of Maryland. Chapter 4 has been submitted in the form of a journal article in the *Journal of Radioanalytical and Nuclear Chemistry* and is currently under revision. All other chapters represent original work.

Acknowledgements

I would like to acknowledge the funding support of DNDO HSHQDC-10-X-00652 and SRNL subcontract #0000092329.

I would also like to thank my advisors Alice Mignerey and Bill McDonough for their help and support throughout my graduate student tenure. Additionally I would like to thank Richard Ash and Brian Ticknor for their invaluable discussions concerning the day-to-day operation of mass spectrometers and their troubleshooting help. Also this work would not have been accomplished without the support and facilities of the Radiation Safety Office, specifically Mary Dorman, Edward Case, and Brian Zidek.

Finally, I would like to thank my friends and family for their emotional support while performing this work and for the writing process. Most of all, I would like to thank my wife Miriam Sharp for all of her extensive proof-reading help, listening to me excessively talk through my problems, and for overall mental and health well-being during the writing process.

Table of Contents

Preface.....	ii
Acknowledgements.....	iii
Table of Contents	iv
List of Tables	vi
List of Figures	viii
List of Abbreviations	x
Chapter 1: Introduction	1
1.1 Purpose of Work	1
1.2 Post-detonation Material - Trinitite	3
1.3 Pre-detonation Material – Spent Nuclear Fuel	4
1.3.1 Material Test Reactors	5
1.4 Dissertation Outline	6
1.4.1 Chapter 2.....	6
1.4.2 Chapter 3.....	6
1.4.3 Chapter 4.....	7
1.4.4 Chapter 5.....	7
1.4.5 Chapter 6.....	8
Chapter 2: Nuclear Fundamentals.....	9
2.1 Nuclear Structure and Stability.....	9
2.2 Neutron Capture.....	15
2.3 Neutron Induced Fission.....	21
2.4 Direct and Indirect Lanthanoid Fission Production.....	24
2.5: Stable Lanthanoid Isotopic Composition.....	27
2.6: Mixing of Fission Products and Natural Lanthanoid Isotopes	29
Chapter 3: Lanthanoid Separation and Mass Spectrometry.....	33
3.1 Mass Spectrometry	33
3.1.1 Basic Theory	34
3.1.2 Instrument Induced Mass Fractionation Correction	38
3.1.3 Sample Measurement Procedure.....	43
3.2 Justification for Separation of Lanthanoids	46
3.2.1 Composition of pre- and post-detonation materials.....	46
3.3 Separation Method.....	50
3.3.1 Trinitite Digestion and Matrix Removal.....	51
3.3.2 Fuel Rod Sampling and Matrix Removal	54

3.3.3 Chromatographic Separation of the Lanthanoids	63
Chapter 4: Trinitite ¹	70
4.1 Abstract.....	70
4.2 Introduction.....	71
4.3 Experimental methods	73
4.3.1 Electron microprobe.....	75
4.3.2 Sample Digestion and Chromatography	75
4.3.3 LA-ICP-MS and MC-ICP-MS	76
4.4 Results.....	81
4.5 Discussion.....	88
4.5.1 Nd and Gd Isotopic Composition	89
4.6 Conclusion	98
Chapter 5: Sm and Nd Isotopic Composition in Three Research Reactor Fuels	100
5.1 Introduction.....	100
5.2 Materials and Methods.....	102
5.2.1 Fuel Rod Sampling and Lanthanoid Separation	102
5.2.2 MC-ICP-MS.....	105
5.3 Results.....	107
5.4 Discussion.....	111
5.4.1 Yields and Blanks	111
5.4.2 Nd and Sm Isotope Abundances	113
5.4.3 Fluence Calculations.....	120
5.5 Conclusions.....	123
Chapter 6: Summary	124
6.1 Lanthanoid Separation Method.....	124
6.2 Pre and Post-detonation Material Analyses	126
6.2.1 Trinitite	126
6.2.2 MTR Fuel.....	126
6.3 Conclusions.....	127
Bibliography	128

List of Tables

Chapter 2

Table 2.1. Neutron orbital configuration and thermal neutron capture cross sections for stable, even proton number lanthanoids.....	17
Table 2.2. List of neutron energy regions.....	19
Table 2.3. Cumulative fission yields of lanthanoids via thermal (0.025 eV) and fission (0.5 MeV) neutron induced fission of ^{235}U and ^{239}Pu	25
Table 2.4. List of independent and cumulative yields of lanthanoids of interest in ^{239}Pu fission.....	27
Table 2.5. Natural isotopic abundances of Nd, Sm, and Gd.....	29
Table 2.6. Isotopic composition of Nd, Sm, and Gd in Oklo sample.	31

Chapter 3

Table 3.1. Long term reproducibility of Nd, Sm, and Gd standards using internal mass fractionation correction terms.....	42
Table 3.2. The instrumental conditions for MC-ICP-MS analyses at UMD and SRNL.....	44
Table 3.3. Isobaric interferences in natural and fission produced lanthanoids.	47
Table 3.4. Concentration and activity of selected elements in the 2010 fuel rod stock solution in SRNL Shielded Cells.....	48
Table 3.5. Major element oxide composition obtained via EPMA analysis of various locations on a trinitite sample.	52
Table 3.6. Information on the three fuel rods sampled at SRNL.....	55
Table 3.7. Results from a cursory HPGE analysis on 1 mL aliquots of the lanthanoid section removed from Shielded Cells.	63
Table 3.8. Final separation method for trinitite and fuel samples.	69

Chapter 4

Table 4.1. The instrument operational conditions used for LA-ICP-MS analysis.....	78
Table 4.2. The instrument operational conditions used for MC-ICP-MS analysis....	80
Table 4.3. Major element oxide composition obtained via EPMA analysis of trinitite.....	83
Table 4.4. Trace element results obtained via LA-ICP-MS with concentrations in $\mu\text{g/g}$ obtained via ablation yield normalizations.....	85
Table 4.5. Nd and Gd isotopic ratios for standards and trinitite sample.....	87
Table 4.6. List of independent and cumulative yields of lanthanoids of interest.	91

Chapter 5

Table 5.1. Instrument operational conditions used for MC-ICP-MS analysis of MTR samples.....	106
Table 5.2. Concentration of Nd and Sm ($\mu\text{g/mL}$) in stock solutions at SRNL.....	108
Table 5.3. Nd and Sm isotopic ratios in MTR samples and natural materials with 2σ uncertainties.....	109
Table 5.4. Isotope abundances of Nd and Sm in the three MTR fuels.	110
Table 5.5. ORIGEN-S predicted isotope abundances of Nd, Sm, and Gd in the three MTR fuels.	111
Table 5.6. Initial and final ^{235}U enrichment of the three MTR fuel rods.	118
Table 5.7. Neutron fluence results using the listed isotopic ratios and Eq. 5-1.....	122

List of Figures

Chapter 2

Figure 2.1. Nuclear shell model with magic numbers circled.	10
Figure 2.2. Mass vs binding energy per nucleon.	12
Figure 2.3. Capture cross section dependency on neutron energy for ^{147}Sm	19
Figure 2.4. Cumulative thermal neutron fission yields for ^{235}U and ^{239}Pu	22
Figure 2.5. Cumulative fission yields of neutron induced fission of ^{235}U with thermal and 14 MeV neutrons.	23
Figure 2.6. Lanthanoid region of the cumulative thermal neutron yield of ^{235}U and ^{239}Pu	24

Chapter 3

Figure 3.1. Schematic of the torch region of an ICP-MS.	35
Figure 3.2. Typical sample of trinitite.	50
Figure 3.3. Lanthanoid separation procedure for trinitite samples.	54
Figure 3.4. Nitric acid column calibration for nuclear fuel samples.	56
Figure 3.5. Mixed acid column calibration for nuclear fuel samples.	57
Figure 3.6. Column calibration prior to separation of nuclear fuel samples.	59
Figure 3.7. Column apparatus inside Shielded Cells.	60
Figure 3.8. Dried down 2009 fuel rod sample inside Shielded Cells.	61
Figure 3.9. Separation using HCl with Ln resin.	65
Figure 3.10. Column calibration with A) 0.15 M α -HIBA and B) 0.225 M α -HIBA .	67

Chapter 4

Figure 4.1. BSE image of the two pieces of trinitite mounted in epoxy.	74
-----------------------------------------------------------------------------	----

Figure 4.2. Cross section BSE image of trinitite.	82
Figure 4.3. Comparison of lanthanoid concentrations obtained with LA-ICP-MS on trinitite and reference materials.	84
Figure 4.4. Isotopic composition of Gd analyzed with LA-ICP-MS.	86
Figure 4.5. Isotopic deviations of Gd in trinitite obtained with MC-ICP-MS.	95
Figure 4.6. Isotopic deviations of Nd in trinitite obtained with MC-ICP-MS.	96

Chapter 5

Figure 5.1. Percent difference of Nd isotope abundances compared to ORIGEN-S model.	114
Figure 5.2. Percent difference of Sm isotope abundances compared to ORIGEN-S model.	115
Figure 5.3. (A)Nd and (B) Sm isotope abundance percent differences in MTR 2009 and MTR 2011 compared to MTR 2010.	117
Figure 5.4. Percent difference of measured isotope abundance of (A) Nd and (B) Sm in MTR 2010 compared to ORIGEN-S and MONTEBURNS models.	119
Figure 5.5. Modeled isotopic abundances of Gd in MTR 2009, 2010, and 2011 using ORIGEN-S.	120

List of Abbreviations

α :	${}^4\text{He}^{2+}$ nucleus
α -HIBA:	α -hydroxyisobutyric acid
AG-50W:	Analytical grade cation exchange resin
ASTM:	American Society for Testing and Materials
β^- :	electron particle emitted from a radioactive nucleus
β^+ :	Anti-electron; positron
BE/n:	Binding Energy per nucleon
BHVO-2:	Hawaiian basalt standard reference material
BIR:	Icelandic basalt standard reference material
BSE:	Backscatter electron
CPS:	Counts per second
dpm:	Decays per minute
ϵ :	Deviations in 1 part in 10,000
EPMA:	Electron probe micro-analysis
ESA:	Electrostatic analyzer
HDEHP:	di(2-ethylhexyl) orthophosphoric acid
HEU:	Highly enriched Uranium
HPGE:	High purity germanium detector
HPLC:	High performance liquid chromatography
IAEA:	International Atomic Energy Agency
LA-ICP-MS:	Laser ablation inductively coupled plasma mass spectrometer
LAMTRACE:	Computer program for calculating elemental concentration from LA-ICP-MS data
LEU:	Low enriched Uranium
MBF:	Mass bias factor
MC-ICP-MS:	Multi-collector inductively coupled plasma mass spectrometer
MONTEBURNS:	Monte Carlo particle burnup code
MTR:	Material test reactor
ORIGEN:	Oak Ridge Isotope GENeration code
RDD:	Radiological dispersal device
RF:	Radio-frequency
σ_n :	Neutron capture cross section
SC-ICP-MS:	Single-collector inductively coupled plasma mass spectrometer
SEMF:	Semi-empirical mass formula
SRM:	Standard reference material
SRNL:	Savannah River National Laboratory
TIMS:	Thermal ionization mass spectrometer
UMD:	University of Maryland
ν_e :	Electron-neutrino
$\bar{\nu}_e$:	Anti-electron-neutrino
ZAF:	Atomic number, absorption, and fluorescence correction algorithm for EPMA

Chapter 1: Introduction

1.1 Purpose of Work

Interdiction of nuclear materials have been ongoing for the last two decades with the quantities of nuclear material involved ranging from gram to kilogram amounts (ITDB, 2013). The nuclear materials being smuggled range from vials of highly-enriched uranium (HEU) (Wallenius et al., 2006) to components of reprocessed nuclear fuel (Moody et al., 2005). From a national security standpoint the most likely use of nuclear material in a terrorist-based attack would be in the form of a radiological dispersal device (RDD). These devices are simple and usually incorporate a highly-radioactive source, such as spent nuclear fuel, and conventional explosives with the goal to contaminate a large region with high-activity radioisotopes. The potential for destruction is only on the order of a building or two, but the potential difficulty in dealing with the radioactive contamination can be very expensive and challenging, not to mention the public panic that such a device might produce.

The other, more serious, use of nuclear material is in the development of a nuclear fission weapon. These are very complex devices and would require a very sophisticated organization or state support to engineer such a device. The destructive potential of such a nuclear device is large, with yields ranging from kilotons to megatons of TNT.

Detonation of both RDD and fission devices would leave traces of their original components in the resulting debris that could potentially be used to determine the types of devices as well as their starting materials. Samples of this nature are

known as post-detonation materials. They can be very complex to analyze due to changes in the chemical and isotopic makeup of the materials as a result of the detonation process. While a simple RDD would most likely only adjust the elemental compositions of the samples, based on the volatility of the source elements, a fission device imparts changes on the isotopic level from different fission product yields as well as the release of neutrons that undergo neutron capture events with the original material. In either type of device the original material will be mixed with natural background materials.

To determine the source nuclear material of a RDD or a fission device, the lanthanoids are an ideal elemental group to analyze. The lanthanoids are produced via neutron induced fission of both ^{235}U and ^{239}Pu , but in different amounts and isotopic abundances. This allows investigators to analyze the lanthanoid isotopic composition of materials that have been subjected to fission events and determine the fissile isotopes (Fujii et al., 2000; Hidaka and Masuda, 1988; Loss et al., 1988; Maas and McCulloch, 1990). Lanthanoids also contain a number of isotopes with extremely large neutron absorption cross sections. These high capture cross sections result in depletion of certain isotopes (e.g., ^{157}Gd) followed by a corresponding enrichment in the A+1 mass isotopes (e.g., ^{158}Gd). By comparing the enrichments and depletions in certain isotopic ratios relative to their natural ratios, the neutron fluence (n/cm^2) can potentially be calculated. Therefore, the measurement of the isotopic composition of lanthanoid elements using mass spectrometry can be a powerful tool for nuclear forensic investigators.

1.2 Post-detonation Material - Trinitite

Urban post-detonation debris is extremely limited, as the only occasions that have produced such debris were in the nuclear bombing of Nagasaki and Hiroshima. The only other type of post-detonation samples originated from nuclear weapon tests conducted during the Cold War era. However, many of those sites and their debris are unavailable for researchers to sample. An exception is the Trinity test site.

In the early hours of July 16 1945 the Trinity device was detonated at the White Sands Proving Ground, New Mexico. Trinity was an experimental ^{239}Pu implosion device with a ^{239}Pu subcritical core surrounded by high-explosives. The explosives were detonated, crushing the core into a critical geometry and exposing a previously shielded initiator (Be) that produced neutrons after capture of an alpha particle (one of the main decay particles emitted by ^{239}Pu). This initiator provided the pulse of neutrons that started the chain reaction, ultimately resulting in a ~20 k ton explosion.

The Trinity test resulted in a fireball with temperatures approaching 10^4 K that vitrified the surrounding desert floor. The resulting glassy material is known as trinitite and contains melted and un-melted components of the original desert floor, initial fissile material, bomb components, and fission products. Trinitite can be viewed as a surrogate material for future nuclear device debris, and can be analyzed to determine the original fissile material and neutron fluence by examining the isotopic composition of the lanthanoid elements. For this work a sample of trinitite was digested and the lanthanoid fraction was separated using column chromatography. The Nd and Gd cuts were analyzed using multi-collector

inductively coupled plasma mass spectrometry (MC-ICP-MS) to determine the type of fissile material used in Trinity, along with the total number of thermal neutrons emitted from the explosion.

1.3 Pre-detonation Material – Spent Nuclear Fuel

Spent nuclear fuel from research reactors are important sources of pre-detonation materials that are modeled for understanding how their compositions evolved during their burning and cooling history. This material differs from spent fuel from power reactors due to the typically higher enrichment levels required for research reactors (90-20% vs < 8%). Previously, research reactors used HEU (>90% ²³⁵U) fuels, however, with concerns over the security of these fuels prompted the US to transition to LEU (20% ²³⁵U) fuels. Higher enrichment levels are required to produce the neutron field necessary for experiments such as neutron activation analysis and neutron diffraction studies, carried out at most research reactors. However, these enriched fuels make research reactor sites a target for theft. The high-level of radiation from fission products in spent nuclear fuel also makes this material an ideal candidate for an RDD as well.

The composition of spent nuclear fuel from power reactors is modeled using programs such as Oak Ridge Isotope GENERation (Groff, 1980) (ORIGEN) and a multi-step Monte Carlo burnup code (Trellue, 2003) (MONTEBURNS). These codes function by simulating the amount of fission events caused by a neutron flux on the fuel rods. In each step the fission products are mathematically exposed to the neutron field and the resulting net isotopic composition is calculated. This result is then fed

back into the program, along with decay data, before the next cycle of fission events are calculated, resulting in an iterative process to determine the final composition of the fuel rod. These codes rely on knowledge of the neutron field to which the entire fuel rod has been subjected.

In the case of power reactors, the models have been benchmarked against analyzed spent nuclear fuel and have been shown to provide accurate results (Xulubana et al., 2008, Gauld et al., 2006; Ezure 1989; Tait et al., 1995). This is due, in part, to power reactors having consistent nuclear core geometries. In contrast, research reactors can have core geometries that vary as a result of the experiments being conducted. These variations in geometry can affect the neutron fields via absorption of thermal neutrons (e.g., activation experiments and boron-neutron capture) or the reflectors arranged in the core to maximize neutron fluxes at certain experimental locations. The effect of these non-consistent geometries on the accuracy of ORIGEN and MONTEBURNS is unknown, but the analysis of lanthanoid isotopic ratios can provide information to assess this issue.

1.3.1 Material Test Reactors

The goal of this work is to develop a method to determine the composition of spent nuclear fuel, which in turn can be used to inform studies on the type of facility that produced an intercepted spent nuclear fuel rod. Before these methods can be fully applied, the current accuracy of the modeled results must be tested against actual spent nuclear fuel rods from several different types of reactors to provide a more thorough sample set. To that end, three spent nuclear fuels from material test reactors

(MTR) have been analyzed. The results will be used to determine the accuracy of ORIGEN and MONTEBURNS for spent nuclear fuel from research reactors. The operating history of each of the MTRs is well known, and an average neutron field was determined and used in the models to produce a theoretical nuclear fuel rod of certain lanthanoid composition. The lanthanoids were then extracted from the sampled fuel rods at Savannah River National Laboratory (SRNL) and analyzed via MC-ICP-MS to determine their isotopic composition. The isotopic composition was then compared to the modeled results to determine the accuracy of the codes and whether neutron experiments conducted at the MTR affected the lanthanoid compositions.

1.4 Dissertation Outline

1.4.1 Chapter 2

This chapter introduces the fundamental nuclear processes and properties that are required to understand aspects of this research. Differences in fission yields between ^{235}U and ^{239}Pu , including the effect of incident neutron energy, are described. The neutron capture cross sections are given for thermal neutrons for the stable lanthanoid elements and a discussion is presented of the importance of incorporating resonance capture cross sections.

1.4.2 Chapter 3

Here I review the method developed and processes implemented for the chemical separation of the lanthanoids from both the trinitite and the three MTR spent

nuclear fuels. Chemical separation was achieved using cation exchange chromatography to isolate the lanthanoids from the bulk trinitite and spent nuclear fuel matrices. Subsequently, a chelator was used to separate individual lanthanoids based on ionic radii, prior to analysis on MC-ICP-MS to avoid isobaric interferences. For trinitite, instrumental mass fractionation was corrected using both standard-bracketing and isotope ratio internal correction, while the fuel rod samples required standard-bracketing.

1.4.3 Chapter 4

Results and interpretation of a full suite of analyses of the trinitite sample, as well as the Nd and Gd isotopic composition are presented in this chapter. The trinitite sample showed significant elemental variability and vesicle abundance with increasing depth in the melt pool. The Nd and Gd isotopic compositions revealed non-normal ratios, a sign of fission product contributions and neutron capture effects, with the Nd isotopes being more sensitive to fission yields, while the Gd isotopes were more sensitive to neutron capture effects. Signs of a ^{235}U contribution to Trinity's overall ^{239}Pu fission were also identified in the isotopic composition of Nd.

1.4.4 Chapter 5

Results and discussion of the Nd and Sm isotopic analysis of the spent nuclear fuel rods from the three MTR are presented in this chapter. The Gd cuts were not analyzed due to the absence of a detectable signal. The Nd and Sm isotopes show obvious deviations from natural isotopic composition but the Nd isotopes agree within 10% of modeled results. The model does not predict Sm isotopic abundances

as well as Nd, with differences ranging from 1% to 225%. These large discrepancies in model predictions are due to neutron capture reactions that are evidently not modeled precisely. This is possibly a by-product of an incorrect neutron energy spectrum being used to generate the ORIGEN results.

1.4.5 Chapter 6

Conclusions of the lanthanoid isotopic analysis of trinitite and the three MTR spent fuels are presented here. Future work outside the scope of this project is also described. Recommendations of method adjustments are described to improve the yield and throughput of the presented methods.

Chapter 2: Nuclear Fundamentals

This chapter details the physical processes involved in exposing material to a fission event and the resulting changes in isotopic composition that occur. Specifically the fission events are explained at a nuclear level; including the role of neutron energy on both fission and neutron capture events. To understand these processes the shell model structure of nuclei is introduced and then radioactive decay processes are described in order to give context to neutron capture and fission events.

2.1 Nuclear Structure and Stability

Determining significant information from material having a mixture of natural and fissionogenic isotopic abundances of lanthanoids requires a thorough understanding of nuclear orbital structure, particle-nucleus interactions, and radioactive decay. Atomic nuclei consist of protons and neutrons that occupy independent orbitals in what is known as the Shell Model (Choppin et al., 2002). The nuclear orbitals are arranged according to Fig. 2.1 and, in general, atomic nuclei are more stable when they have full or half-full nuclear orbitals, similar to full and half-shell electron orbitals. Neutrons and protons fill nuclear orbitals independently of one another and also will pair up while filling an orbital. There are regions where groups of nuclear orbitals are separated by large differences in energy. This separation of nuclear shells gives rise to “magic numbers” that are completely full nuclear shells that are below the next level’s large energy barrier.

Insight into the stability and reactivity of a nucleus is a function of the arrangement and number of nucleons. If a nucleus is close to a full or half-full

orbital, then the nucleus is more likely to participate in a reaction with a free nucleon in an attempt to reach a full or half-full orbital. Nuclei that have a magic number of neutrons or protons are typically stable and resistant to any process which would change the number of nucleons present.

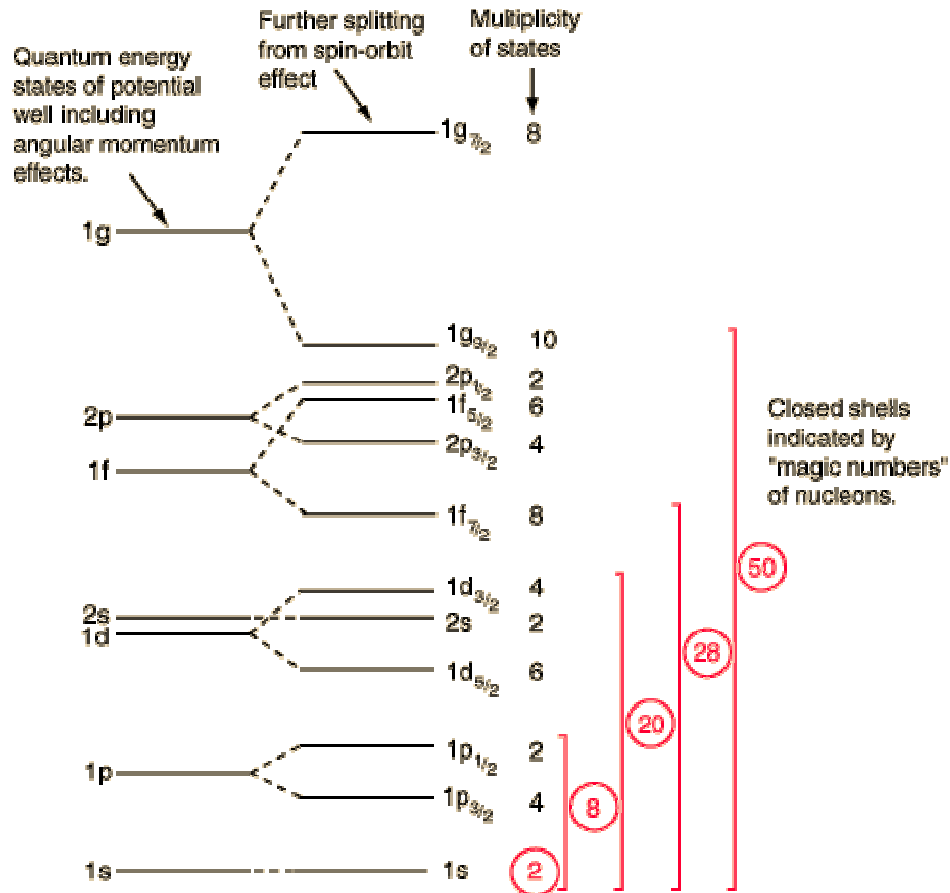


Figure 2.1: Nuclear shell model with magic numbers circled from Cohen (1971).

A nucleus, formed from its component nucleons, has a final mass that is less than its components. This “missing” mass, known as the mass defect, can be calculated using Eq. 2-1:

$$Zp + Nn = {}^A_ZX_N + \Delta m \quad (2-1)$$

where Z represents the number of protons (atomic number), N represents the number of neutrons, A represents the atomic mass, and Δm represents the mass deficiency. The mass defect is the binding energy that holds nucleons together. The conversion from mass to energy units is accomplished by applying Einstein's $E=mc^2$ equation. The theoretical value of the binding energy (E_B) of a perfectly spherical nucleus can be calculated based on the number of neutrons (N), number of protons (Z), mass of the nucleus (A , amu), and several experimentally derived constants (a_V, a_C, a_S, a_δ) using the semi-empirical mass formula (SEMF) given by Eq. 2-2:

$$E_B (MeV) = a_V A - a_a \frac{(N-Z)^2}{A} - a_C \frac{Z^2}{A^{2/3}} - a_S A^{2/3} \pm \frac{a_\delta}{A^{3/4}} \quad (2-2)$$

The five constants can be determined by comparing calculated binding energies with actual binding energies with resulting values of: $a_V = 15.5$; $a_a = 23$; $a_C = 0.72$, $a_S = 16.8$, and $a_\delta = 34$. The SEMF gives good agreement for masses when $A > 40$ and has five major terms. The first term describes the proportionality of binding energy to the total number of nucleons in the nucleus and is known as the volume energy term. The second term describes the balance in the number of protons and neutrons and is known as the asymmetry term. The third term represents the Coulomb repulsion force from protons and the fourth term describes the effect of surface tension. The final term describes additional stability and instability caused by even – even N:Z nuclei and odd-odd N:Z nuclei. The term is added to the SEMF when the binding energy of an even – even nucleus is calculated and subtracted for an odd – odd nucleus. When a nucleus is even – odd (N:Z or Z:N) there is no overall effect on the binding energy, and the last term is then set to zero.

Total binding energy alone does not provide much insight to the stability of a nucleus as smaller nuclei have lower binding energies compared to heavier nuclei, due to the first term in the SEMF. Therefore, more information is gained by investigating the binding energy per nucleon (BE/n) when discussing nuclei stability. The trend of BE/n with mass can be observed in Fig. 2.2 where nuclei with BE/n to the left of the maximum (^{62}Ni , close to ^{56}Fe) gain more stability (higher BE/n) with increased mass (increasing x values), compared to the heavier mass nuclei, which gain stability by losing mass (decreasing x values). The peak at ^{62}Ni represents the point at which the volume term no longer outweighs the other destabilizing terms, resulting in overall decreasing stability with increased mass.

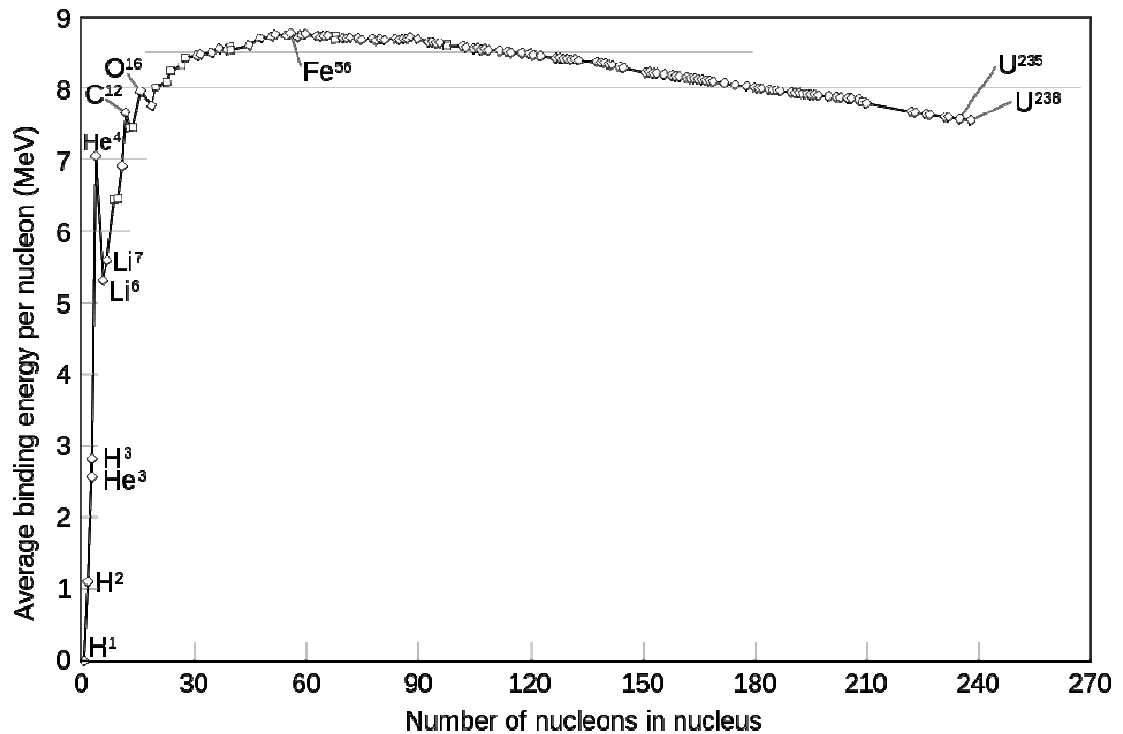


Figure 2.2: Mass vs binding energy per nucleon from Wikimedia Commons (2009).

Observing the asymmetry term on the SEMF shows that as the mass of the nucleus increases the stability of maintaining a 1:1 N:Z ratio begins to decrease.

Nuclei with mass < 20 are most stable when their proton to neutron values are equal. However, when nuclei begin to have masses greater than 20 the Coulomb effect results in stable nuclei having a N/Z ratio close to 1.2-1.4 (Choppin et al., 2002), thus, there is a balancing of the asymmetry term with the Coulomb energy term. If a nucleus is too large or if there are an excess of neutrons or protons, compared to their stable mass isotopes, the nucleus will undergo radioactive decay.

There are multiple types of radioactive decay that a nucleus can undergo to return to stability, depending on the mass and N/Z ratio of the unstable nucleus. As the Coulomb term is directly related to Z^2 while the asymmetry term is related to $(N-Z)^2$, the most obvious method of reducing instability is by reducing the number of protons. The most direct method to reduce the number of protons while not significantly affecting the asymmetry term is via emitting an α -particle (helium nucleus) as illustrated in Eq. 2-3:

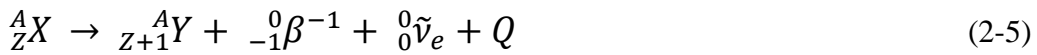


The Q value in the Eq. 2-3 represents the energy released from radioactive decay. If the Q value is positive then the reaction is favored to occur, whereas if the value is negative the decay will not occur. The Q value is the amount of mass lost from the reaction converted to energy using Eq. 2-4:

$$Q(\text{MeV}) = 931.5[m({}^A_ZX) - m({}^{A-4}_{Z-2}Y) - m({}^4_2a)] \quad (2-4)$$

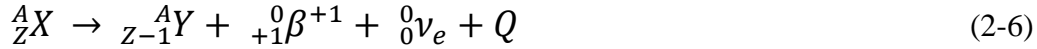
where the 931.5 is the conversion factor from atomic mass units to MeV. Alpha decay removes two protons and, thus, lowers the nuclei's Coulomb repulsion while the BE/n remains essentially unchanged due to the α -particle having approximately the same BE/n as the parent nucleus (Loveland et al., 2006). An example of this is the alpha decay of ^{238}U to ^{234}Th with a change of BE/n from 7.58 MeV to 7.61 MeV with the alpha particle having a BE/n of 7.08 MeV.

In many unstable nuclei the Q value for alpha decay is positive, but not large enough to enable the alpha particle to tunnel out of the Coulomb barrier from the nucleus (potential energy wall) in an observable time scale. Therefore, a different radioactive decay mode, known as β -decay, occurs that changes the number of neutrons or protons. In the event of an excess of neutrons the atom will undergo radioactive decay to convert a neutron to a proton. This mode of radioactive decay is known as β^- decay and is illustrated in Eq. 2-5:



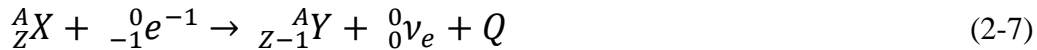
Two particles are emitted from the nucleus during β^- decay: a β^- particle (e^-) and an electron anti-neutrino ($\tilde{\nu}_e$). The presence of the anti-neutrino means that β^- decay is a 2-particle decay and thus the β^- particle has a continuum of energy instead of being mono-energetic like alpha particles. This becomes important later on when discussing safety due to ionizing radiation from radioactive samples.

There is also the β^+ decay mode, which is the decay of a proton to a neutron. This occurs in proton-rich nuclei in the form of Eq. 2-6:



Again two particles are emitted from the nucleus following β^+ decay: a β^+ particle (e^+ , positron) and an electron neutrino (ν_e). The β^+ particle annihilates upon contact with an electron and therefore has a very short lifetime.

A competing reaction to β^+ decay involves the nucleus “capturing” an electron which subsequently reacts with a proton to form a neutron and an electron neutrino, as shown in Eq. 2-7:



This reaction occurs in nuclei not unstable enough to have the energy potential to create a positron. For the purpose of this work, the neutrino and anti-neutrino will be ignored as these particles play no direct role in neutron capture reactions, and both particles have a relatively small potential to interact with matter compared to neutron reactions of interest.

2.2 Neutron Capture

Neutron capture involves a nucleus, A_ZX , capturing a nearby free neutron, as shown in Eq. 2-8, and results in the formation of a compound nucleus ${}^{A+1}_ZX^*$:



When a nucleus captures a neutron the neutron populates an energy level corresponding to the combined neutron’s kinetic energy and the Q value for the

capture reaction. The Q value for the capture reaction is the binding energy of the last nucleon captured. This means that when a neutron is captured by a nucleus, the compound nucleus, ${}^{A+1}_{Z}X^*$, is formed and immediately exists at excitation levels on the order of 3-6 MeV. Depending on the energy of the excited state the compound nucleus can reach the ground state via a variety of actions, such as loss of one or more nucleons, emission of gamma rays, or fission. For nuclei in the lanthanoid mass region the predominant reaction is gamma ray emission and a resulting nucleus one mass larger than the original nucleus.

The likelihood that a nucleus captures a neutron is defined as its neutron capture cross-section (σ_c), which is measured in barns (1 barn is equivalent to 10^{-24} cm²). This capture cross-section parameter is influenced by the neutron orbital configuration of the original nucleus as well as the neutron's energy. Due to the tendency of nucleons to want to exist in pairs, typically nuclei with unpaired neutrons are more likely to capture free neutrons and not have their compound nuclei decompose. This tendency is observed when focusing on natural isotopes of Nd, Sm, and Gd, as shown in Table 2.1, where all the non-paired neutron isotopes have considerably larger neutron capture cross-sections compared to their paired counterparts.

Table 2.1: Neutron orbital configuration and thermal neutron capture cross sections for stable, even proton number lanthanoids (Dunford and Burrows, 1999).

Element	Neutrons	Neutron Shell	Saturation	Cross section (b)
¹⁴² Nd	82	1h11/2	12/12	18.7
¹⁴³ Nd	83	1h9/2	1/10	325
¹⁴⁴ Nd	84	1h9/2	2/10	3.6
¹⁴⁵ Nd	85	1h9/2	3/10	50
¹⁴⁶ Nd	86	1h9/2	4/10	1.5
¹⁴⁸ Nd	88	1h9/2	6/10	2.6
¹⁵⁰ Nd	90	1h9/2	8/10	1.04
¹⁴⁴ Sm	82	1h11/2	12/12	1.63
¹⁴⁷ Sm	85	1h9/2	3/10	57
¹⁴⁸ Sm	86	1h9/2	4/10	2.4
¹⁴⁹ Sm	87	1h9/2	5/10	40,000
¹⁵⁰ Sm	88	1h9/2	6/10	100
¹⁵² Sm	90	1h9/2	8/10	206
¹⁵⁴ Sm	92	1h9/2	10/10	8
¹⁵² Gd	88	1h9/2	6/10	735
¹⁵⁴ Gd	90	1h9/2	8/10	85
¹⁵⁵ Gd	91	1h9/2	9/10	60,000
¹⁵⁶ Gd	92	1h9/2	10/10	2
¹⁵⁷ Gd	93	2f7/2	1/8	250,000
¹⁵⁸ Gd	94	2f7/2	2/8	2
¹⁶⁰ Gd	96	2f7/2	4/8	1

If a nuclei's neutron shell is one neutron away from a half or full-shell, the capture cross section can be greatly enhanced compared to neighboring isotopes. This enhancement is due to a resonance level equal to the Q value for the capture of a neutron by the target nucleus, which decays rapidly to the ground state through emission of gamma rays. Examples of this include ¹⁵⁵Gd (one less neutron) and ¹⁵⁷Gd + ¹⁴³Nd (one excess neutron), all of which possess larger cross sections than their full shell counterparts when considering thermal (0.025 eV neutrons). It is important to note that, while ¹⁴⁹Sm exists in a half-shell configuration, the stability gained by having that lone neutron paired with another free neutron results in that

isotope having a capture cross section of 40,000 b, ~40 times greater than any other Sm isotopes.

Neutron capture cross sections are dependent on neutron energy (E), width of excited nucleus energy levels (Γ), and momentum of the neutron (k). The neutron capture cross section ($\sigma_{n,\gamma}$) can be calculated using the spin of the target and compound nuclei ($J_{A,C}$) and the energy of a single isolated level (E_0) by using the Breit-Wigner equation given by Eq 2-9:

$$\sigma_{n,\gamma} = \frac{\pi}{k^2} \frac{(2J_C+1)}{(2J_A+1)(2)} \frac{\Gamma_n \Gamma_\gamma}{(E-E_0)^2 + \left(\frac{\Gamma}{2}\right)^2} \quad (2-9)$$

As neutron energy decreases to thermal (0.025 eV) the $(E - E_0)^2$ term is no longer dependent on neutron energy and therefore Eq 2-9 simplifies to $\frac{\Gamma_n}{k^2}$. However, Γ_n is dependent on neutron energy and therefore the cross section ultimately goes to $1/k$ and therefore increases with decreasing neutron energy. This can be observed by the overall decreasing neutron capture value with increasing neutron energy for ^{147}Sm shown in Fig. 2.3.

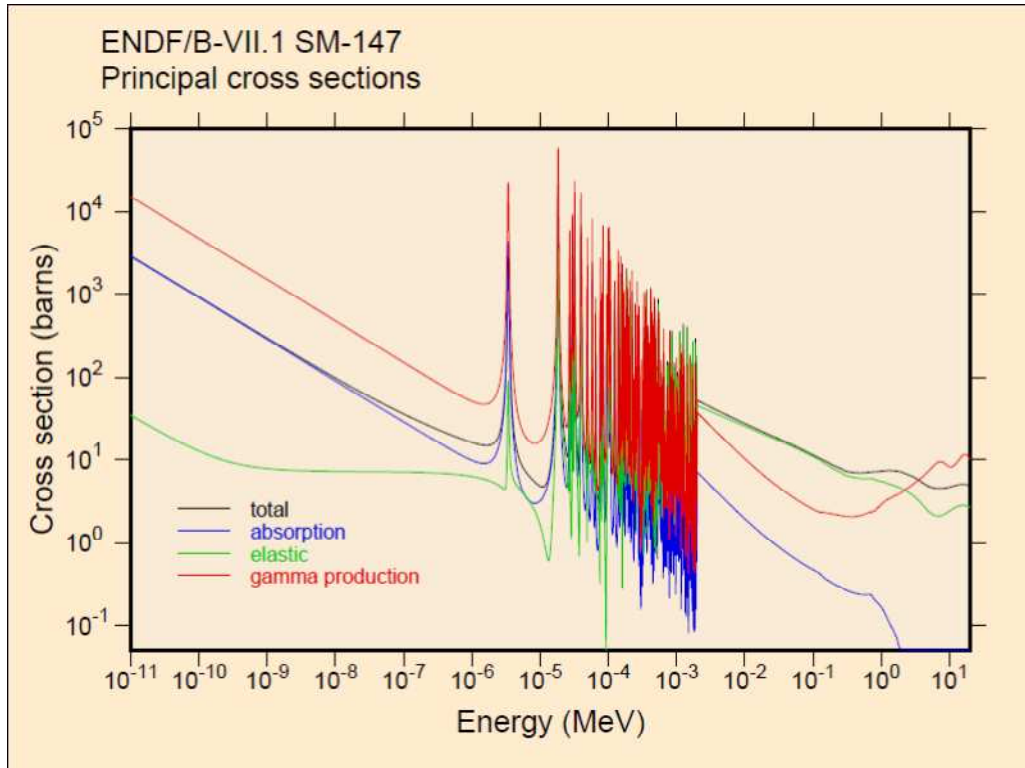


Figure 2.3: Capture cross section dependency on neutron energy for ^{147}Sm from Chadwick et al. (2011).

The overall trend corresponds to a decrease in neutron capture cross section with increasing neutron energy. We will consider 3 distinct energy regions of neutrons: thermal, slow/intermediate, and fast. Table 2.2 breaks down the energy spectrums associated with the 3 regions.

Table 2.2: List of neutron energy regions.

Region	Energy Range (MeV)
Thermal	2.5×10^{-8}
Slow/Intermediate	$2.5 \times 10^{-8} - 0.5$
Fast	≥ 0.5

Nuclei have the largest capture cross sections for thermal neutrons. This is primarily due to the wave-particle duality of neutrons. When a neutron is at low energies, in this case $\sim 0.025\text{eV}$, the neutron's de Broglie wavelength becomes larger than its physical cross section. Therefore, cross sections increase with decreasing energy at sub-thermal neutron energy levels.

In the slow/intermediate region of Fig. 2.3 there are marked oscillations in capture cross sections, which are known as resonance levels. Resonance levels represent single energy levels which are exactly equal to the energy of the incoming neutron and the binding energy for that neutron ($E = E_0$), resulting in a sharp increase and decrease in neutron capture cross. In the case of ^{147}Sm the resonance peaks populate the 2 eV – 2000 eV energy range and can be higher than the cross section value at thermal energies. The largest resonance peak at $\sim 2.5\text{ eV}$ is $\sim 3 \times 10^3\text{ b}$ which is significantly greater than the thermal cross section value of $\sim 50\text{ b}$. Therefore, calculations requiring high accuracy and precision concerning neutron capture by ^{147}Sm must consider thermal and slow/intermediate neutrons as possible capture targets. The resonance at $\sim 2.5\text{ eV}$ must be taken into account, as well as that for thermal energies.

Neutrons in the fast region have neutron capture cross-sections that are orders of magnitude lower than lower energy neutrons for all isotopes of interest investigated for this study. Therefore, fast neutrons are assumed to be inconsequential for this study. Fast neutrons are more likely to undergo inelastic collisions with surrounding nuclei and lose energy. After multiple collisions, typically 20 collisions which occur in the millisecond range (Marmier, 1969), fast

neutrons will thermalize and begin to participate in neutron capture reactions with isotopes of interest. There will be some loss of neutrons during the thermalization process due to (n, particle) reactions or escape of neutrons from the sampling environment prior to capture reactions.

2.3 Neutron Induced Fission

Fission occurs when the parent nucleus can achieve a higher Be/N by forming two smaller nuclei. As shown in Fig. 2-2 the binding energy per nuclei reaches a maximum around ^{62}Ni and then subsequently decreases with increasing mass. This decrease in binding energy per nucleon means that heavy nuclei can achieve additional stability by splitting into two smaller nuclei. There exists a fission energy barrier which must be exceeded before fission can occur. For some neutron capture reactions the resulting compound nucleus is formed with enough energy to overcome the barrier and subsequently fission.

Neutron induced fission of ^{235}U and ^{239}Pu is a significant research topic as these are the prominent fissile materials for research reactors and fission weapons. With thermal neutrons (0.025 eV) the corresponding excitation energies for the compound nuclei ^{236}U and ^{240}Pu (^{235}U and ^{239}Pu post-neutron capture) are both 6.5 MeV and the fission barriers are between 5-6 MeV (Choppin et al., 2002) so these compound nuclei typically undergo fission.

Thermal Neutron Induced Fission

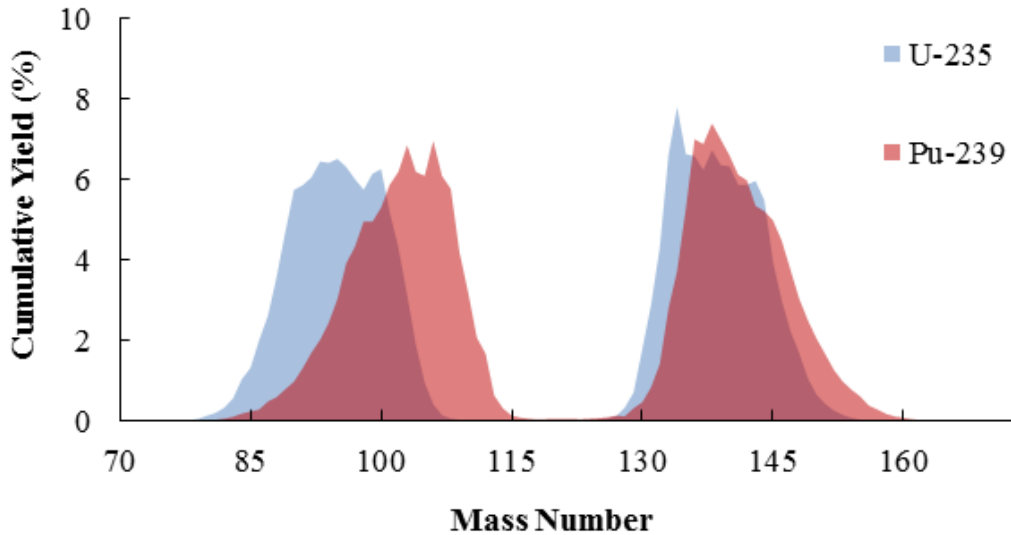


Figure 2.4: Cumulative thermal neutron fission yields for ^{235}U and ^{239}Pu . Data modified from Nichols et al. (2008).

Fission products have differing yields depending on the parent fissile nucleus and the energy of the incident neutron. The fission product distributions shown in Fig. 2.4 reveal two distinct mass regions of products that do not follow a Gaussian distribution around the half mass of the fissile nucleus. Instead, the fission products group into light and heavy-fission products clustered around neutron magic numbers of 50 and 82, which correspond roughly to masses 90 and 137.

When a fissile nucleus captures a thermal neutron, the compound nucleus exists in an excited state comparable to its fission barrier. The excited nucleus, which behaves somewhat like a drop of liquid, oscillates into two semi-stable nuclei, which will then break free of the compound nucleus during the fission event. When a fast neutron is captured the resulting compound nucleus exists in an excited state far above its fission barrier, and exists for too short a period of time to form two semi-stable fission fragments and instead breaks apart. The influence of neutron energy is

apparent in Fig. 2.5 where the 14 MeV neutron induced fission of ^{235}U has a much more symmetrical distribution around mass 118 compared to thermal neutron induced fission.

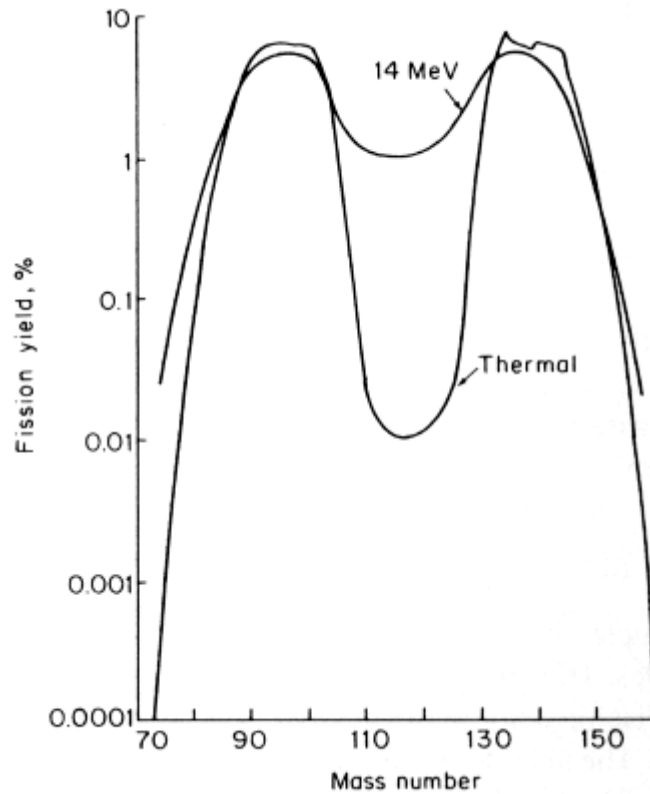


Figure 2.5: Cumulative fission yields of neutron induced fission of ^{235}U with thermal and 14 MeV neutrons from Lamarsh (1966).

Constraining the energy of the fission inducing neutron is very important when attempting to determine the influence of fission products on natural isotopic abundance materials. Higher energy incident neutrons can change cumulative fragment production by up to 30% (Chadwick et al., 2006). It is also important to precisely identify the parent fissile material as different fissile materials will also produce different fission yield spectrums (Fig. 2.4).

The light-mass and heavy-mass fragments have combined proton numbers equal to the fissile nucleus. The neutron numbers, however, are different due to 2-3 neutrons being released per fission event. The release of more than 1 neutron per fission event is what drives the chain reactions that sustain nuclear reactors and form the massive energy release found in fission weapons.

2.4 Direct and Indirect Lanthanoid Fission Production

Lanthanoids populate the tail-end of the heavy-mass fragment curve. Their mass abundances spectra reflect both the type of fissile material, shown in Fig. 2.6 and Table 2.3, and the energy of the neutron environment. When compared to ^{235}U fissioning, ^{239}Pu results in a relative decrease of the fission production of the light lanthanoids from La to Sm and an increase in the production of Eu and Gd. Some light lanthanoid isotopes can only be generated via fission of ^{239}Pu compared to ^{235}U , such as ^{142}Nd which has a $1.09 \times 10^{-6}\%$ yield from ^{239}Pu fission compared to $4.63 \times 10^{-9}\%$ in ^{235}U .

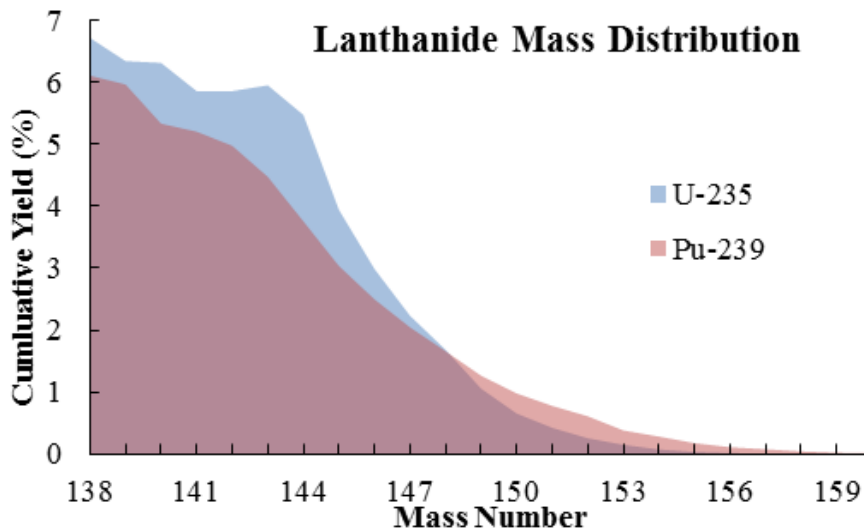


Figure 2.6: Lanthanoid region of the cumulative thermal neutron yield of ^{235}U and ^{239}Pu . Data modified from Nichols et al. (2008).

The Gd fission yield from ^{239}Pu is greater compared to ^{235}U fission (Table 2.3), whereas the yields of Nd and Sm are roughly equivalent for both ^{239}Pu and ^{235}U . Therefore, Gd isotopic abundances can provide a clear indicator of ^{239}Pu vs ^{235}U fission.

Table 2.3: Cumulative fission yields of lanthanoids via thermal (0.025 eV) and fission (0.5 MeV) neutron induced fission of ^{235}U and ^{239}Pu . Data modified from Chadwick et al. (2011).

	Thermal Neutrons		Fission Neutrons	
	^{235}U	^{239}Pu	^{235}U	^{239}Pu
^{142}Nd	$4(6) \times 10^{-9}\%$	$1(1) \times 10^{-6}\%$	$2(2) \times 10^{-9}\%$	$1(1) \times 10^{-6}\%$
^{143}Nd	5.96(4)%	4.41(4)%	5.73(6)%	4.33(3)%
^{144}Nd	5.50(4)%	3.74(2)%	5.27(7)%	3.69(5)%
^{145}Nd	3.93(3)%	2.99(2)%	3.78(4)%	3.00(3)%
^{146}Nd	3.00(2)%	2.46(2)%	2.92(3)%	2.46(2)%
^{148}Nd	1.67(1)%	1.64(2)%	1.68(2)%	1.66(1)%
^{150}Nd	0.653(6)%	0.966(6)%	0.686(6)%	0.99(1)%
^{144}Sm	0.00%	0.00%	0.00%	0.00%
^{146}Sm	$2(1) \times 10^{-10}\%$	$3(3) \times 10^{-9}\%$	$3(3) \times 10^{-12}\%$	$6(7) \times 10^{-9}\%$
^{147}Sm	2.25(3)%	2.00(4)%	2.14(3)%	2.01(3)%
^{148}Sm	$1(2) \times 10^{-8}\%$	$6(7) \times 10^{-6}\%$	$5(6) \times 10^{-8}\%$	$2(2) \times 10^{-5}\%$
^{149}Sm	1.08(2)%	1.22(2)%	1.04(1)%	1.24(1)%
^{150}Sm	$3(4) \times 10^{-5}\%$	0.001(1)%	$3(3) \times 10^{-5}\%$	0.002(3)%
^{152}Sm	0.267(5)%	0.58(1)%	0.271(7)%	0.63(2)%
^{154}Sm	0.074(1)%	0.260(6)%	0.072(1)%	0.267(7)%
^{152}Gd	$1(4) \times 10^{-10}\%$	$7(8) \times 10^{-8}\%$	$5(6) \times 10^{-11}\%$	$9(10) \times 10^{-8}\%$
^{154}Gd	$2(2) \times 10^{-7}\%$	$3(3) \times 10^{-5}\%$	$6(8) \times 10^{-8}\%$	$5(6) \times 10^{-5}\%$
^{155}Gd	0.032(3)%	0.17(3)%	0.039(8)%	0.21(4)%
^{156}Gd	0.0149(8)%	0.12(1)%	0.0203(8)%	0.15(1)%
^{157}Gd	0.006(1)%	0.074(8)%	0.011(5)%	0.11(2)%
^{158}Gd	0.0033(6)%	0.04(1)%	0.006(2)%	0.07(2)%
^{160}Gd	$3(2) \times 10^{-4}\%$	0.010(3)%	0.0011(3)%	0.02(1)%

Differences in the incident neutron energy can also alter the yields of the lanthanoids. The degree of change in yields fluctuates between a factor of 2 decrease in Nd, compared to an overall increase in Sm and Gd. While the degree of change is

small, the resulting effect on isotopic ratios requires constraining the incident neutron energy. Measuring the ratio of $^{147}\text{Sm}/^{152}\text{Sm}$ from ^{239}Pu fission is 3.45 or 3.19, depending on whether the incident neutron had thermal or fission energy. This level of change is detectable using MC-ICP-MS, so it is critical to have some understanding of the neutron energy spectrum in the samples being analyzed.

Another variable that affects the lanthanoid fission product yield is time since the fission events took place. Fission products are neutron rich, as they generally have similar N/Z ratios as the original fissile material. Neutron rich isotopes typically decay towards the valley of nuclear stability via β^- decays, by increasing their proton number while maintaining a stable mass. For the lanthanoid isotopes, very few stable lanthanoids are produced immediately following a fission event (independent yield), as observed in Table 2.4. Instead, lower Z isotopes are produced with half-lives varying from seconds to minutes. The entire β^- decay path from the original fission product to a stable lanthanoid can take hours to days, which results in changing isotopic ratios depending on how recently the sample underwent a fission event. The final yield is known as cumulative yield and takes into account the sum independent yields for all isotopes that have decayed to the final stable isotope. For our samples the materials last experienced fission events 30-60 years ago, more than enough time for complete β^- decay, with the exception of some long-lived isotopes such as ^{90}Sm and $^{152,154,155}\text{Eu}$.

Table 2.4: List of independent and cumulative yields of lanthanoids of interest in ^{239}Pu fission. Data taken from Chadwick et al. (2011).

Stable Isotope	Independent Yield (%)	Cumulative Yield (%)	Parent Isotope	Half-life (minutes)
^{142}Nd	$2\pm 1\times 10^{-10}$	$1.2\pm 0.7\times 10^{-6}$	^{142}Pr	2×10^3
^{144}Nd	$2.8\pm 0.9\times 10^{-9}$	3.69 ± 0.03	^{144}Ba	6×10^5
^{145}Nd	$4\pm 2\times 10^{-6}$	3.00 ± 0.02	^{145}La	3×10^1
^{146}Nd	$8\pm 5\times 10^{-5}$	2.46 ± 0.01	^{146}Ce	3×10^1
^{148}Nd	$7\pm 4\times 10^{-3}$	1.658 ± 0.006	^{148}Ce	3×10^0
^{150}Nd	$1.0\pm 0.6\times 10^{-1}$	0.993 ± 0.005	^{150}Pr	1×10^{-1}
^{146}Sm	0	$3\pm 2\times 10^{-9}$	^{146}Pm	3×10^6
^{147}Sm	$2\pm 1\times 10^{-11}$	2.00 ± 0.02	^{147}Ce	1×10^0
^{148}Sm	$2\pm 1\times 10^{-9}$	$6\pm 4\times 10^{-6}$	^{148}Ce	1×10^0
^{149}Sm	$8\pm 5\times 10^{-8}$	1.217 ± 0.008	^{149}Pr	2×10^0
^{150}Sm	$3\pm 2\times 10^{-6}$	$1.2\pm 0.7\times 10^{-3}$	^{150}Pr	1×10^{-1}
^{152}Sm	$4\pm 3\times 10^{-4}$	5.763 ± 0.006	^{152}Nd	1×10^1
^{154}Sm	$9\pm 6\times 10^{-3}$	2.598 ± 0.004	^{154}Nd	5×10^{-1}
^{155}Gd	$3\pm 2\times 10^{-7}$	0.21 ± 0.02	^{155}Pm	4×10^6
^{156}Gd	$7\pm 2\times 10^{-7}$	0.154 ± 0.006	^{156}Pm	3×10^4
^{157}Gd	$3\pm 2\times 10^{-5}$	0.106 ± 0.008	^{157}Sm	1×10^3
^{158}Gd	$2\pm 1\times 10^{-4}$	0.06 ± 0.01	^{158}Sm	5×10^2
^{160}Gd	$1.1\pm 0.7\times 10^{-3}$	0.016 ± 0.005	^{160}Eu	9×10^{-1}

2.5: Stable Lanthanoid Isotopic Composition

Like all natural elements, the stable isotopic composition of the lanthanoids is a product of red giant and supernovae processes. Specifically, the lanthanoids formed via neutron capture processes during the lifetime of a red giant star and during supernovae events, respectively. The slow process, or s-process, is the slow neutron capture that occurs throughout the lifetime of some stars. Due to the long timescales involved in neutron captures in the s-process, isotopes with short half-lives decay before capturing another neutron, effectively reducing the abundance of the heavier

stable isotopes. An example of this can be found in Nd, where the abundances of the isotopes from 142-150 are similar with the exceptions of $^{145,148,150}\text{Nd}$. The high neutron capture cross section of ^{145}Nd results in a lower abundance compared to its neighboring isotopes while ^{148}Nd and ^{150}Nd exist after the short-lived ^{147}Nd and ^{149}Nd which do not exist long enough to be produced via the s-process. The s-process builds up to ^{146}Nd , and when it reaches ^{147}Nd , the 11 day half-life results in ^{147}Nd β^- decaying to ^{147}Pm and then ^{147}Sm before another neutron could be captured. The result of this evolutionary process is that ^{148}Nd and ^{150}Nd have abundances greatly reduced compared to the other Nd isotopes.

Neutron-rich isotopes that are less commonly produced via s-process are instead created during supernovae events in what is known as the rapid process, or r-process. During a supernova event a large flux of neutrons is released, on the order of 1×10^{24} neutrons/cm²/second. This neutron flux results in a rapid series of neutron captures that halt only when the neutron drip line has been reached for an element. Once there the isotope undergoes β^- decay and subsequent additional neutron captures, resulting in the r-process creating the neutron rich isotopes. In our previous example, ^{148}Nd and ^{150}Nd would be produced as lower Z mass isotopes of 148 and 150, respectively, elements with highly unstable neutron/proton ratios and subsequently undergo β^- decays.

The natural Nd, Sm, and Gd isotopic abundances are given in Table 2.5. These are due to a combination of the s and r-processes. The variability in stable naturally occurring lanthanoid isotopes is small, varying less than 0.04% for most isotopes (Berglund and Wieser, 2009). There are some larger variations in ^{143}Nd and

^{147}Sm due to the alpha decay of ^{147}Sm , which has a half-life of 1×10^{11} years; resulting in abundances in the range of 12.18% to 12.06% (Faure and Mensing, 2005).

Table 2.5: Natural isotopic abundances of Nd, Sm, and Gd from Berglund and Wieser (2009).

Element	Isotope	Abundance (%)
Nd	142	27.152(40)
	143	12.174(26)
	144	23.798(19)
	145	8.293(12)
	146	17.189(32)
	148	5.756(21)
	150	5.638(28)
Sm	144	3.07(7)
	147	14.99(18)
	148	11.24(10)
	149	13.82(7)
	150	7.38(1)
	152	26.75(16)
	154	22.75(29)
Gd	152	0.20(1)
	154	2.18(3)
	155	14.8(12)
	156	20.47(9)
	157	15.65(2)
	158	24.84(7)
	160	21.86(19)

2.6: Mixing of Fission Products and Natural Lanthanoid Isotopes

There are locations on Earth where naturally occurring fission events have resulted in mixing of natural lanthanoid isotopic composition with fission lanthanoids. Rocks from these settings have depletions and enrichments in all lanthanoid isotopic ratios, especially in Nd, Sm, and Gd systems. These alterations

due to mixing of fission product and natural material provide predictions of what the lanthanoid isotopic compositions may resemble in the trinitite and spent nuclear fuel rods analyzed in this work.

The most iconic site of fission product and natural material mixing was discovered at Oklo, a uranium mine in Gabon, Africa. In 1972 it was discovered that some of the uranium ore had a ^{235}U content as low as 0.29% compared to the normal value of 0.72%. Further analyses determined that approximately 2 billion years ago a uranium rich mineral region contained enough ^{235}U (~3% abundant at that time) that the ground water in the region provided enough moderation to initiate a chain reaction (IAEA, 1975). The natural nuclear reactor would fission until a sufficient temperature had been reached where the moderating water would be boiled away and the chain reactions would shut down. After the area had cooled, water could begin flowing again and the fission events would restart. This cycling occurred for ~200,000 years and resulted in a total neutron fluence of 10^{21} n/cm² and a total energy released of about 10^{11} kWh (IAEA, 1975).

More in-depth investigation of Oklo revealed that the isotopic compositions of the lanthanoid elements, notably Nd, Sm, and Gd, had changed significantly when compared to their natural abundances (Hidaka and Masuda, 1988). The degree of change can be observed in Table 2.6 (data reproduced from Hidaka and Masuda, 1988), which shows the isotopic abundances of lanthanoids found in two separate samples from different regions at Oklo analyzed by Hidaka and Masuda, 1988. Based on Gd isotopic ratios, they estimated the neutron fluence exposure of their two samples was approximately 1×10^{20} n/cm². While Oklo samples do not reflect the

fissionogenic nature of spent nuclear fuel, it is likely more altered than one would expect for trinitite due to the more sustained exposure to fission events compared to the singular blast of Trinity.

Table 2.6: Isotopic composition of Nd, Sm, and Gd in Oklo sample reproduced from Hidaka and Masuda, 1988.

Element	Isotope	Abundance (%)
Nd	142	4.97(2)
	143	24.44(3)
	144	27.18(6)
	145	16.81(3)
	146	15.13(1)
	148	7.74(1)
	150	3.73(1)
Sm	144	0.343(9)
	147	52.76(1)
	148	2.54(1)
	149	1.04(1)
	150	25.88(2)
	152	12.96(1)
	154	4.48(1)
Gd	152	13.73(3)
	154	4.38(3)
	155	0.844(1)
	156	32.69(4)
	157	0.146(1)
	158	31.92(4)
	160	16.29(2)

Another uranium deposit at the Nabarlek deposit in the Alligator River Uranium Field, Australia was affected by the spontaneous fission of ^{238}U (Maas and McCulloch, 1990), and shows lesser degrees of lanthanoid isotopic alteration due to fission product and neutron effects when compared to Oklo. The most notable

isotopic alterations are observed as depletions in $^{149}\text{Sm}/^{152}\text{Sm}$ and $^{155,157}\text{Gd}/^{160}\text{Gd}$, where ^{149}Sm , ^{155}Gd , and ^{157}Gd are known for having large thermal neutron cross sections of 4×10^4 b, 6×10^4 b, and 2×10^5 b, respectively. These depletions, highest of $-16 \text{ } \epsilon$ compared to natural, were caused by a neutron fluence of $\sim 1 \times 10^{14}$ n/cm², which was primarily due to spontaneous fission of ^{238}U instead of the neutron induced fission of ^{235}U found at Oklo. The lower neutron fluence and subsequent smaller amount of fission events seen in the Nabarlek ores more closely represent the degree of lanthanoid isotopic alterations present in trinitite compared to the Oklo samples.

Chapter 3: Lanthanoid Separation and Mass Spectrometry

This chapter details the separation and measurement method for trinitite and the research reactor spent nuclear fuel samples. In summary, the lanthanoids were separated from the sample matrix and individually isolated through a two-step chromatography system using cation exchange resins with a variety of eluents. The isotopic compositions of Nd and Sm in trinitite and the nuclear fuels were analyzed using a multi-collector inductively coupled plasma mass spectrometer (MC-ICP-MS) at the University of Maryland (UMD), while the isotopic composition of Gd in trinitite was analyzed using an identical instrument at Savannah River National Laboratory (SRNL). Results for trinitite and the nuclear fuels are reported and interpreted in Chapters 4 and 5, respectively.

3.1 Mass Spectrometry

High precision isotopic measurements of nanogram amounts of lanthanoids were first achieved using thermal ionization mass spectrometry (TIMS) (Wasserburg et al. 1981; Wasserburg et al. 1969; DePaolo and Wasserburg 1976). Sample analysis with TIMS involves loading the purified element of interest onto a filament which is heated while under vacuum. Heating the filament ionizes the sample, resulting in a very stable ion beam. A multi collector configuration allows simultaneous measurements of multiple ion beams, reducing fluctuations in the ion beams and

lowering the uncertainty in the measurements and allowing high precision results to be obtained.

Another technique for measuring lanthanoid isotopic ratios with comparable precision and detection limits to TIMS is MC-ICP-MS (Weis et al., 2005; Baker et al., 2002). The use of a plasma as the ionization source decreases the time necessary for sample preparation as the sample only needs to be dissolved in an acidic solution compared to loading the sample onto a filament. However, there is an increase in the instability of the signal compared to TIMS. Instrument induced mass fractionation is also higher in MC-ICP-MS compared to TIMS, however proper correction terms and stable measurement conditions results in comparable results from MC-ICP-MS and TIMS (Weis et al., 2006). Instrument induced mass fractionation results in measuring more of the heavier mass isotopes compared to the lighter mass isotopes. The decision was made to use MC-ICP-MS for our sample analyses due to the simpler sample preparation and instrument availability at both SRNL and UMD.

3.1.1 Basic Theory

The MC-ICP-MS has a plasma ionization source, illustrated in Fig. 3.1, typically produced with a 1 L/min Ar gas flow passed through a torch surrounded by a radio-frequency (RF) load coil which is used to generate the plasma. A tesla coil sends a pulse of electrons up to the torch region which provides the seed for initiating ionization of the Ar gas, producing Ar^+ and free electrons. The electrons then interact with the RF field and cause additional collisions with neutral Ar atoms, resulting in additional ionization events. The cascade of ionization events forms a plasma, a

neutral association of positively charged ions and free electrons, reaching temperatures of 6,000 - 8000 K.

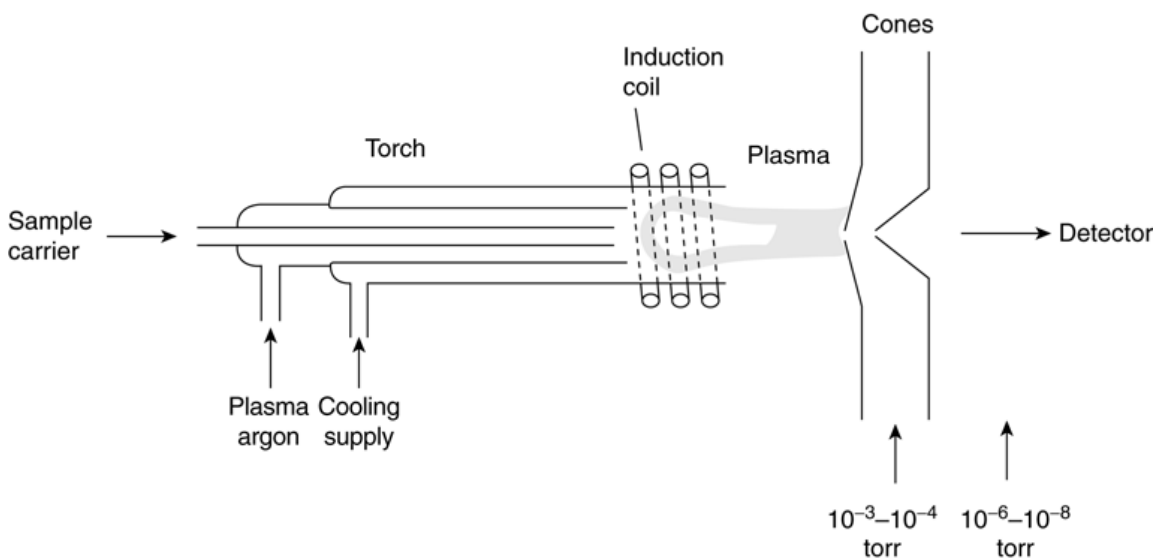


Figure 3.1: Schematic of the torch region of an ICP-MS from Group, 2012.

Sample analysis with MC-ICP-MS is carried out via dry-plasma mode sample introduction the mass spectrometer via a desolvating unit, the Aridus I and DSN-100 (UMD and SRNL, respectively). The sample is brought into the desolvator via a self-aspirating nebulizer as a spray of droplets typically at a rate of $\sim 50 \mu\text{L}/\text{min}$. The aerosol is sprayed into a heated spray chamber resulting in rapid drying of the aerosol into solution vapors and analyte particles. These vapors and particles travel into the desolvating membrane, where a countercurrent N_2 - Ar gas mixture removes the vapors, resulting in only the analyte particles entering the mass spectrometer. Treating the sample solution through a desolvator is preferable to directly aspirating the sample solution into the plasma (wet-plasma), as the latter enhances molecular oxide production, and molecular isobaric interferences. Dry-plasma mode

significantly reduces the presence of non-analyte molecules, resulting in lower production of molecular species.

As the plasma is dominantly made up of Ar^+ ions, any elemental species with an ionization potential below 15.76 eV, which includes the majority of the periodic table (Atkins and de Paula 2006), are ionized to at least the 1+ state. Neutral atoms ionize by absorbing thermal energy from the plasma environment. If an atom has a higher ionization potential than Ar the ion will remove an electron from the abundant neutral Ar atoms and revert to a neutral state.

Positive ions are preferentially extracted through a ~1 mm aperture in the sampling cone, held at positive bias (4,000 V and 6,000 V for UMD and SRNL, respectively) and by the differential pressure between the atmospheric plasma region and the 2 mbar region behind the sampler cone. The electrons are attracted to the surface of the sampler cone due to the positive bias and are removed from the plasma, resulting in only neutral and positively charged particles emerging through the cone. The sampler cone then acts as an accelerator for the charged species, pushing them through the less positively charged skimmer cone. A large percentage of ions (~99%) are lost at this stage due to gas expansion, space-charge effects and the smaller aperture on the skimmer cone, 0.7 mm. The remaining ions are focused through a series of extraction lenses into a spot onto the entrance slit.

After the focusing optics and the entrance slit, the ion beam passes through the electrostatic analyzer (ESA), filtering the ion beam based on its spread in kinetic energies. This filtering insures that the remaining ions all have about the same kinetic energy, enabling magnet separation based on the ion's mass/charge ratio. Lighter

mass/charge isotopes are deflected more than larger mass/charge isotopes. This difference in deflection causes the isotopes to be spatially separated into individual beams. The resulting ion beams pass through two zoom lenses (Quad 1 and 2 on the Nu Plasma) which adjust the spatial separation between the ion beams by focusing the ion beams on to the collector array. The spatial separations of the ion beams are adjusted until their spatial separation aligns with the required detector arrangement on the mass spectrometer, resulting in simultaneous analysis of multiple isotopes.

The Nu Plasma MC-ICP-MS has a series of 12 faraday cups and 3 electron multiplier ion counters available as detectors. Signal detection on the faraday cups is obtained by a digital voltmeter measuring the potential difference across a 10^{11} ohm resistor caused by the impact of the positive ion beam. The entrance to the faraday cups has a negative bias to prevent loss of electrons produced through secondary processes caused by the impact of positive ions on the faraday cup's surface. Faraday cups on this instrument can measure signals in the 10 – 0.003 V range, but for this work the preferred voltage range was 2 – 0.01 V to conserve the lifetime of the faraday cups while still producing sufficient signal to obtain high-precision counting statistics. All measurements taken for this work were conducted on the faraday cups.

The precision of isotopic ratios measured with an MC-ICP-MS follows a Poisson counting statistic distribution, where uncertainties are calculated by taking the square root of the total number of ions detected (N) as expressed in:

$$\sigma = \frac{1}{\sqrt{N}} \quad (3-1)$$

The number of ions striking the detector can be calculated from the reported voltage by converting from voltage to current and dividing by the elementary charge constant (e) given by:

$$\frac{\text{Ions}}{\text{second}} = \frac{\text{Voltage (Volts)}}{\text{Resistor (Ohms)} * e(\text{Coulombs})} \quad (3-2)$$

A 1 V signal represents 6×10^7 ions/sec and with a target of epsilon level precision, the uncertainty on a single measurement would need to be less than 0.5σ (2σ). Therefore, assuming zero noise and background, it would take at a minimum 26 seconds to obtain the number of ions required to achieve the Poisson's uncertainty. However, isotope beams was significantly lower, then the uncertainty would be dominated by the lower abundance isotope and therefore the measurement time would have to be increased (e.g. 0.01 V signal needs 43 minutes to reach 0.5σ).

The major source of background noise on faraday cups comes from thermal or Johnson noise. With a $1 \times 10^{11} \Omega$ resistor the thermal noise will have a value of ~ 0.23 mV, therefore, signals will need to be greater than 3 mV to enable quantitative analyses. Fluctuations in the beam and sample gas flows can also cause additional beam instability, increasing the measurement uncertainty. However, these can be minimized by optimizing the instrument settings prior to analysis.

3.1.2 Instrument Induced Mass Fractionation Correction

All mass spectrometers introduce a phenomenon where some of the isotopes of an element are under or over represented in the detected signal. This phenomenon is known as instrument induced mass fractionation. In ICP-MS systems the cause of

this mass fractionation is due to space-charge effects, which occur in the region immediately after the first sampler cone. Prior to the sampler cone the plasma can be considered to be net-neutral, as there are equal numbers of electrons and positive ions. However, due to the positively charged sampler cone, electrons are removed from the plasma, resulting in a net-positive ion beam immediately after the sampler cone. As positive ions repel each other, the lighter isotopes are kinetically scattered further away from the central ion channel relative to the heavier isotopes. The result is that the lighter isotopes are under-represented in the final ion beams reaching the detectors.

For isotopes k and j , the mass fractionation in ICP instruments can be corrected by applying an exponential law correction where the measured isotopic ratio (R_{kj}^m) is multiplied by the ratio of its component masses ($m_{k,j}$) raised to a mass bias factor (MBF – α):

$$R_{kj}^C = R_{kj}^m * \left(\frac{m_k}{m_j}\right)^\alpha \quad (3-3)$$

The R_{kj}^C term refers to the corrected isotopic ratio. The MBF (α) requires a “true” value for a specific isotopic ratio (R_{ij}^N where i and j are two isotopes of a given element) to be known or at least accepted in the community as shown in:

$$\alpha = \frac{\ln \left[\frac{R_{kj}^M}{R_{ij}^N} \right]}{\ln \left[\frac{m_k}{m_j} \right]} \quad (3-4)$$

The assumed isotope ratio used for fractionation correction is typically determined via a consensus among the mass spectrometry community (Berglund and Wieser, 2009). For Nd measurements the typical isotopic ratio used is $^{146}\text{Nd}/^{144}\text{Nd} = 0.7219$ while in Sm it is $^{148}\text{Sm}/^{154}\text{Sm} = 0.49419$ (Wasserburg et al., 1981). The ideal isotopic ratios for mass fractionation are ratios with a value close to unity, which reduces the uncertainty of the measurement, and ratios which encompass the largest mass region (Wasserburg et al., 1981). Other methods involve the use of different mass fractionation ratios chosen based on the similarity of the control average mass with the measured ratio's average mass (Brennetot et al., 2005), (e.g. $^{155}\text{Gd}/^{160}\text{Gd}$ as the correcting ratio for the measured $^{157}\text{Gd}/^{158}\text{Gd}$).

Analyses can be corrected for fractionation in two methods: internal correction and standard-sample-standard bracketing. For the bulk of sample analyses instrument induced mass fractionation is corrected by monitoring a specific isotopic ratio and correcting the measured isotopic ratio to the “true” value using Eq. 3-4. An α value is calculated and applied to all other measured isotopic ratios using Eq. 3-3 and the corrected ratios are obtained. This method is preferred due to the ability to correct for changing fractionation conditions which may occur during an analysis (non-stable MBF fluctuations vs time).

Standard-sample-standard bracketing is necessary when the isotopic composition of a sample has been altered in such a way that the “true” value is no longer valid, such as fission and neutron capture events. In these cases standard-sample-standard bracketing is preferred. A sample analysis would be preceded and

followed by analysis of a standard with a known or well-characterized isotopic composition. The standard would be corrected using the internal correction method and the calculated MBF would then be applied to the measured ratios in the sample. This method is more sensitive to changing conditions during a series of analyses as the MBF may drift from sample to standard. The standard also should go through the same chemistry as the sample to ensure that no matrix effects or column induced fractionation effects are present that might produce different MBF in a clean standard versus a sample. A standard solution was taken through the same separation process and its MBF value was used for sample mass fractionation corrections during the fuel sample analyses.

Mass fractionation for Nd, Sm, and Gd was corrected using $^{146}\text{Nd}/^{144}\text{Nd} = 0.7219$ obtained from Wasserburg et al. (1981), $^{148}\text{Sm}/^{154}\text{Sm} = 0.49419$ from Wasserburg et al. (1981), and $^{156}\text{Gd}/^{160}\text{Gd} = 0.9361$ from Eugster et al. (1970). These correction terms have been used consistently in the mass spectrometry community. The reproducibility of Nd, Sm, and Gd analyses at UMD and SRNL are $\pm 2 \square$ (2σ) over the course of multiple years and after several analyses as shown in Table 3.1.

Table 3.1: Long term reproducibility of Nd, Sm, and Gd standards using internal mass fractionation correction terms

Nd ^a	¹⁴² Nd/ ¹⁴⁴ Nd	±2σ	¹⁴³ Nd/ ¹⁴⁴ Nd	±2σ	¹⁴⁵ Nd/ ¹⁴⁴ Nd	±2σ	¹⁴⁸ Nd/ ¹⁴⁴ Nd	±2σ	¹⁵⁰ Nd/ ¹⁴⁴ Nd	±2σ
n=35	1.14173	0.00019	0.512127	0.000038	0.348405	0.000022	0.241534	0.000022	0.236314	0.000037
Sm ^a	¹⁴⁴ Sm/ ¹⁵⁴ Sm	±2σ	¹⁴⁷ Sm/ ¹⁵⁴ Sm	±2σ	¹⁴⁹ Sm/ ¹⁵⁴ Sm	±2σ	¹⁵⁰ Sm/ ¹⁵⁴ Sm	±2σ	¹⁵² Sm/ ¹⁵⁴ Sm	±2σ
n=13	0.13520	0.00017	0.65922	0.00021	0.60762	0.00010	0.324478	0.000053	1.175477	0.000031
Gd ^b	¹⁵² Gd/ ¹⁶⁰ Gd	±2σ	¹⁵⁴ Gd/ ¹⁶⁰ Gd	±2σ	¹⁵⁵ Gd/ ¹⁶⁰ Gd	±2σ	¹⁵⁷ Gd/ ¹⁶⁰ Gd	±2σ	¹⁵⁸ Gd/ ¹⁶⁰ Gd	±2σ
n=52	0.00926	0.00011	0.099710	0.000029	0.676778	0.000082	0.715867	0.000037	1.135908	0.000089

^aMeasured on Nu Plasma MC-ICP-MS at UMD

^bMeasured on Nu Plasma MC-ICP-MS at SRNL

3.1.3 Sample Measurement Procedure

Before any sample measurements are performed a series of instrumental parameters must be optimized to obtain high sample sensitivity and signal stability. The parameters that must be tuned are: i) gas flows on the Aridus I and DSN-100; ii) torch position; iii) extraction lens potentials; and iv) zoom optics potentials. Typically the optimization procedure for the instrument at UMD and SRNL begins by adjusting the Ar sweep gas (sample gas) and the N₂ auxiliary gasses to obtain a stable signal. The torch position is then adjusted in the x, y, and z planes to maximize signal intensity while the gas flows are again adjusted if necessary to improve the signal stability. The torch position and the desolvator (Aridus and DSN-100) gas flows are adjusted iteratively until the signal intensity and stability have been optimized. The extraction lenses are then adjusted to enhance the sample intensity with the gas flows again being adjusted if necessary to remain at optimum stability. Typical operating parameters (excluding the torch position and extraction lens voltages) are in Table 3.2.

Table 3.2: The instrument operation al conditions for MC-ICP-MS analyses at UMD and SRNL.

Nu Plasma HR MC-ICP-MS parameters^a	
RF power	1300 W
Reflected power	5 W
Accelerating voltage	4000 V
Cool gas flow	13 L min ⁻¹ Ar
Auxiliary gas flow	1 L min ⁻¹ Ar
Sweep gas flow ^b	2.75 L min ⁻¹ Ar
N ₂ gas	10 mL min ⁻¹ N ₂
Aspiration rate	50 µL min ⁻¹
Integration time	10s
Blocks	5
Background time	30s between blocks
Nu Plasma HR MC-ICP-MS parameters^c	
RF power	1300 W
Reflected power	0 W
Accelerating voltage	6000 V
Cool gas flow	13 L min ⁻¹ Ar
Auxiliary gas flow	0.8 L min ⁻¹ Ar
Sample gas flow ^d	4.5 L min ⁻¹ Ar
Aspiration rate	100 µL min ⁻¹
Integration time	10s
Blocks	5
Background time	30s between blocks

^a University of Maryland – Nd isotopes

^b Gas flows were set using an Aridus I

^c Savannah River National Laboratory – Gd isotopes

^d Gas flows were set using a DSN-100

Zoom optics are positioned after the magnetic sector and adjust the relative dispersion and focal plane of the beam with respect to the faraday cup array.

Whereas the torch position, gas flows, and extraction potentials are essentially uniform for multiple elemental species, the zoom optics are specific for each individual element and also for the isotope-faraday cup detection arrangements. Adjusting the quad values affects both the coincidence and shape of the separate ion beams. Coincidence refers to the alignment of the ion beams to ensure they enter the faraday cups simultaneously. The zoom lenses focuses the ion beams by adjusting the spacing between each ion beam; adjusting the quad values results in increasing or decreasing the separation until they are in-line with the fixed spacing of the detector. If the coincidence is not optimized for all the isotope peaks then the resulting measurements will not be centered in the cups and additional noise could be introduced to the measurement.

The ion beam peak shapes are flat topped with sharp slopes and are created by scanning the ion beam across the cup entrance slits, via adjustment of the magnetic field, into the faraday cup. As the ion beam enters the cup the signal quickly increases until the ion beam is no longer attenuated by the cups slit, resulting in the aforementioned flat top. As the ion beam begins to be attenuated by the other side of the cup slit the signal begins to drop quickly to background. The beam's width is proportional to the two breaks in slope at background and flat top. The peak's narrow aspect and sharp slope indicates how well the beam has been focused. Flat top peaks indicate that the entire ion beam is in the cup and is the critical region for obtaining high-precision isotopic ratios. Adjusting the zoom optics can affect the beam's focusing and result in non-flat topped peaks due to increasing the beam's width.

Conversely the zoom optics can also decrease the beam's width and are typically the first parameter adjusted if peak shapes are non-ideal.

3.2 Justification for Separation of Lanthanoids

3.2.1 Composition of pre- and post-detonation materials

Lanthanoids exist at trace concentrations in natural materials, typically on the order of parts per million (ppm $\mu\text{g/g}$) in average bulk continental crust (Rudnick and Gao, 2003). In unburned nuclear fuel elements the lanthanoids are required by American Society for Testing and Materials (ASTM), standards to exist at the sub ppm level. This is due to the high neutron absorption cross section that Sm and Gd exhibit in the thermal neutron energy spectrum. A high concentration of lanthanoids could result in "poisoning" the fuel and causing detrimental effects in the nuclear reactor core. Poisoning the fuel refers to reducing the neutron flux ($\text{n/cm}^2/\text{sec}$) due to neutron captures on non-fissile nuclei. The lanthanoids possess isotopes with large neutron capture cross sections (^{149}Sm , ^{155}Gd , and ^{157}Gd on the order of 1×10^4 b and greater) which can severely attenuate the neutron flux, and could cause the chain reaction events to halt.

Assuming the simplest case of a post-detonation material which has decayed over a sufficient time that the fission product's radioactivity is at its least harmful, as is the case in trinitite, the sample would still have to undergo chemical processes to isolate the lanthanoid group. This need is due to the presence of several isobaric interferences in the lanthanoids as shown in Table 3.3, including a few isobaric interferences that do not exist in natural materials but were produced during fission

processes. Isobaric interferences can be either atomic or molecular species which have the same mass/charge ratio as the isotope of interest ($^{158}\text{Dy}^+$ and $^{142}\text{Nd}^{16}\text{O}^+$ vs $^{158}\text{Gd}^+$). Mass spectrometry analyses typically require that all isobaric interferences be removed before analysis; however, in some instances it is possible to deconvolute isobaric effects provided that the isotopic composition of the sample is unaltered from its natural abundance. In the case of both fission events in nuclear fuel and post-nuclear detonation samples, this assumption is no longer valid; therefore the isobaric interferences must be removed from the sample.

Table 3.3: Isobaric interferences in natural and fission produced lanthanoids.

Isotope Mass	Natural Elements	Non-natural Isobars
142	Nd, Ce	Pr
143	Nd	Ce
144	Nd, Sm	Ce
145	Nd	
146	Nd	Sm
147	Sm	
148	Nd, Sm	
149	Sm	
150	Nd, Sm	
151	Eu	Sm
152	Sm, Gd	Eu
153	Eu	
154	Sm, Gd	Eu
155	Gd	Eu
156	Gd, Dy	
157	Gd	
158	Gd, Dy	
159	Tb	
160	Gd, Dy	

In spent nuclear fuel elements there is an additional critical need for isolating the lanthanoid elements. The fuel will contain short-lived fission products, listed in Table 3.4, in quantities that are a serious health hazard due to the amount of emitted radioactivity (in decays per minute – dpm). The radioactivity produced via short-lived radionuclides (Table 3.4) requires that the lanthanoids be separated from the bulk dissolved fuel rod before any mass spectrometry can be attempted. Until the short-lived fission products can be removed, all chemistry involving the nuclear fuel samples must be conducted in Shielded Cells at SRNL.

Table 3.4: Concentration and activity of selected elements in the 2010 fuel rod stock solution in SRNL Shielded Cells.

Element	Concentration	Activity (dpm/mL) ^a
Al	1.40%	0
U	0.06%	1E+04
La	16 ppm ^b	0
Ce	31 ppm	0
Pr	15 ppm	0
Nd	55 ppm	0
Sm	11 ppm	7E+06
Eu	702 ppb	5E+06
Gd	280 ppb	0
Tb	3 ppb	0
Cs	25 ppm	2E+09
Ba	24 ppm	2E+09
Sr	11 ppm	2E+09
Y	8 ppm	2E+09

^aValues calculated based off of modeled abundances and activities.

^bwt %

Post-detonation materials typically do not contain uniform concentrations of short-lived fission products due to the dispersive nature of the debris cloud produced in a nuclear explosion compared to the contained fuel rod environment in a reactor core. However, some post-detonation samples may still be too radioactive to process by hand immediately following a nuclear event, and for this reason the lanthanoids must be separated from the bulk material. In other materials that have radioactivity below safety thresholds, due to either low concentrations of short-lived fission products or adequate time for radioisotopes to decay away, there are other reasons for isolating the lanthanoids from the bulk post-detonation material. These materials have the potential to be extremely varied, ranging from urban debris to vitrified sand. Lanthanoid concentrations ($\mu\text{g/g}$) in possible post-detonation materials are comparable to that in the upper crust and in urban dust (Angelone et al., 2007; Celo et al., 2011), thus, highlighting the importance of trinitite as a post-detonation analogue material.

Trinitite samples studied in this project were provided to the UMD Geology Department by the Smithsonian National Museum of Natural History. The samples have a glassy upper surface (Ross, 1948), and often some of the original desert sand on the bottom, as shown in Fig. 3.2. For the isotopic analyses, only pieces of the glassy material were sampled, as only the glassy material contains direct fallout particles and fission products at high enough concentrations to change the naturally occurring isotopic signatures. Including the original desert sand found on the bottom of the sample would dilute the isotopic signature of the fission event and was therefore avoided.



Figure 3.2: Typical sample of trinitite with smooth glassy top region and signs of original desert floor on the bottom from Wikimedia Commons (2009).

The three nuclear fuel samples examined come from separate research reactors. These research reactors differed in regards to their reactor core designs and the initial enrichment ^{235}U . For the purposes of this work the samples will be referred to as reactor 2009, 2010, and 2011, which are references to when each reactor fuel rod was sampled at SRNL Shielded Cells. Each sampling event was conducted in a containment vessel which served to minimize contamination of the samples from the shielded cells environment and a blank that was processed simultaneously with each sampling event. The blanks and samples were then dissolved in 150 mL of ~50% aqua regia and stored in Shielded Cells.

3.3 Separation Method

Due to the trace amounts of lanthanoids in both spent nuclear fuel and post-detonation materials, and health concerns inherent in highly radioactive samples, the lanthanoids should be separated from the bulk material before any analytical measurements are performed. To successfully measure the lanthanoid isotopic

compositions in spent nuclear fuel and trinitite the samples must go through: i) chemical digestion, ii) lanthanoid separation from matrix and iii) chromatographic separation of the lanthanoids.

All digestion processes, apart from the nuclear fuel rods, were carried out in a class 1000 (ISO, 1999) clean lab located in the Geology Department at UMD. The acids used in the digestion and chromatography processes were ultra-high purity, either generated in-house using a quartz and subsequent teflon distillation process or ordered directly from suppliers. Resins and columns were rinsed with several column volumes 6 M HCl and 6 M HNO₃ prior to use. The fuel rods were sampled and digested in the Shielded Cells Facility at SRNL along with the lanthanoid separation chemistry. The separation of Nd, Sm, and Gd for the fuel rods was conducted in a radiation hood at UMD.

3.3.1 Trinitite Digestion and Matrix Removal

Trinitite samples, BHVO-2 standards (a geological reference material), and an analytical blank were digested and separated in the clean lab at UMD. Digestion of trinitite was carried out in teflon containers which went through a prior cleaning process involving two cycles of a reagent grade acid bath followed by 18 M Ω water rinse. The trinitite sample, BHVO-2 standards, and blanks were treated with a 5 mL 4:1 mixture of high-purity concentrated HF and HNO₃ and 100 μ L of HClO₄ in sealed 15 mL teflon beakers. The samples were heated on a hotplate to 180°C for three days, then opened and taken to dryness. To convert the residual perchlorates to

chlorides the dried samples were treated with 6 M HCl and sealed. The samples were heated overnight and taken to dryness again. This process was repeated three times and the final samples were dissolved with 2 mL of 2.5 M HCl.

Trinitite's matrix predominantly consists of SiO₂ and other major oxides which can be found in Table 3.5 (see Chapter 4 for more details). The important detail to note in Table 3.5 is that only Al and a fraction of Fe share the same 3⁺ oxidation state as the lanthanoids. The bulk of the other elements exist in the 2⁺ and 1⁺ oxidation states. Differences in the oxidation states between bulk material and the lanthanoid group allows the application of cation exchange chromatography to isolate the lanthanoids.

Table 3.5: Major element oxide composition obtained via EPMA analysis of various locations on a trinitite sample.

	E1	E2	E3	E4	E5	E6	E7	E8	E9
<i>Oxide wt%</i>									
SiO ₂	64.74	64.96	65.43	67.72	68.14	65.52	57.10	65.03	96.42
TiO ₂	0.08	0.03	0.08	0.54	0.45	0.37	0.92	0.62	b.d.*
Al ₂ O ₃	18.81	19.46	18.21	15.25	13.86	17.31	13.25	11.82	0.15
FeO	1.15	0.28	1.05	3.15	2.53	2.71	6.57	2.55	0.16
MnO	0.02	b.d.*	0.02	0.07	0.06	0.06	0.09	0.05	b.d.*
MgO	0.39	0.03	0.44	1.30	1.06	1.00	2.74	0.94	0.06
CaO	0.38	1.27	4.62	6.66	7.00	7.10	15.15	8.68	0.32
Na ₂ O	2.14	2.61	2.05	2.09	1.82	2.21	1.71	2.04	0.20
K ₂ O	10.25	10.32	7.92	3.55	3.32	3.17	2.32	3.05	0.30
Total	97.96	98.96	99.82	100.33	98.24	99.45	99.85	94.78	97.61

*below detection limit

Cation exchange resin consists of a styrene divinylbenzene copolymer lattice with sulfonic acid functional groups attached. The sulfonic acid groups are negatively charged and attract cations, bonding them to the resin while anions and neutral species are not selected. The cation exchange resin when placed in a column

holds cations while the liquid phase washes the neutral and anion species off the resin. Cations are selectively removed from the resin by varying the strength and nature of the eluent (e.g., decreasing pH), thus increasing the number of H⁺ ions, which will wash off the cations. The extent to which the cations are bound to the resin is based on their ionic radii and total charge, with ions having greater charge held preferentially compared to lower charge species. The 3⁺ ion lanthanoids are held on the resin with the initial, relatively weak acid, while lower charge species are washed off. Later, using a more concentrated acid, the lanthanoids are removed as a group, resulting in a purified sample.

The separation method used to isolate the lanthanoids from the sample matrix involved a quartz column with an internal diameter of 2 cm and a length of 12 cm filled with AG50W-x8 200-400 mesh resin purchased from Bio-Rad. The resin was cleaned by passing several column volumes of quartz-distilled 6 M HCl through the column several times. After the resin was cleaned it was treated with 3 column volumes of 2 M HNO₃ to equilibrate the resin. The sample was then loaded onto the resin and 55 mL of 2 M HNO₃ was passed through the column to strip out most of the matrix ions. The acid concentration was increased to 4 M HNO₃ and after 5 mL the lanthanoids were collected in the next 30 mL eluted. The above process was chosen after performing a variety of column calibrations to determine the most effective combination of acid volumes and concentrations. The final column calibration is shown in Fig. 3.3 and was measured using a single collector inductively coupled plasma mass spectrometer (SC-ICP-MS). Following elution of the 30 mL lanthanoid

cut, the solution was consolidated into one teflon beaker and dried to completion in preparation for the next column chromatography step.

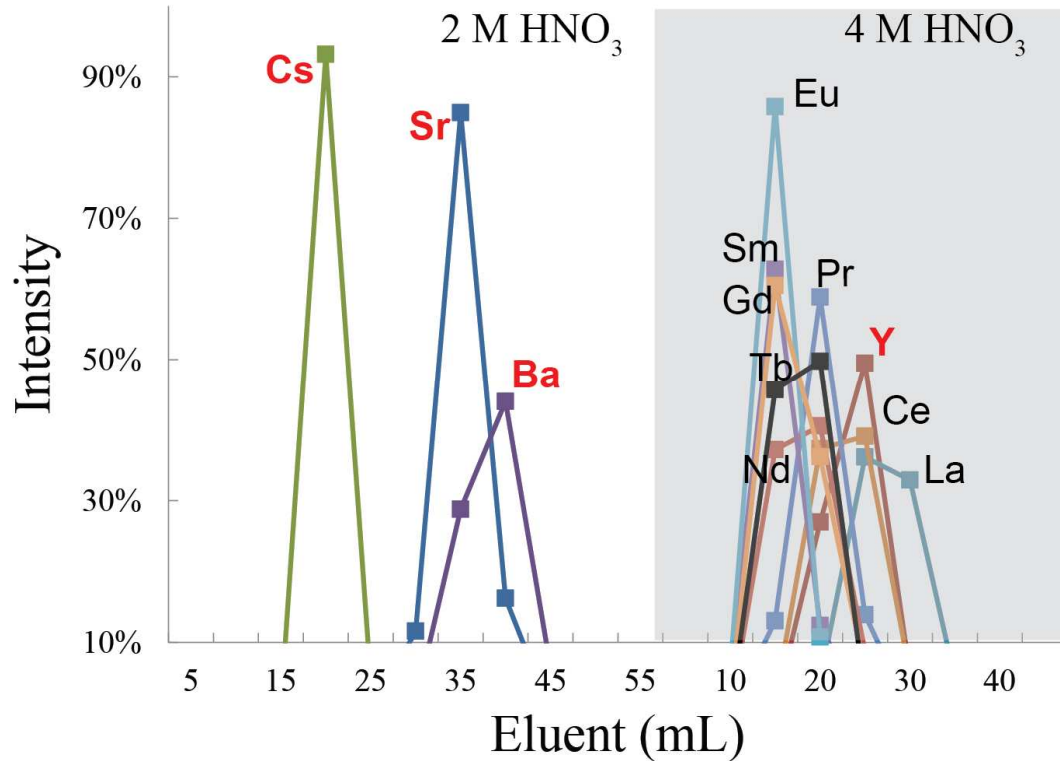


Figure 3.3: Lanthanoid separation procedure for trinitite samples. Column cuts were taken every 5 mL and analyzed using a SC-ICP-MS. Intensity is the ratio of the cut signal over the total signal produced by the entire chromatogram.

3.3.2 Fuel Rod Sampling and Matrix Removal

As a radiation safety requirement the three fuel rods were sampled remotely using the Shielded Cells facility at SRNL individually in 2009, 2010, and 2011. Each sampling required that the fuel rod be inserted into a custom made containment unit which was sealed to keep cross contamination to a minimum. Ideally sampling the fuel rod would consist of coring through all the uranium fuel plates (~19 per fuel rod) to obtain a truly representative aliquot of the entire fuel rod. However, this would result in solutions with high radioactivity levels which would necessitate large

dilution volumes, resulting in large amounts of highly radioactive liquid which is logistically very challenging. A compromise was achieved by coring only the first layer of uranium fuel using a 3/8th inch drill bit to a depth of 0.05 cm resulting in sampled masses recorded in Table 3.6. This resulted in obtaining a representative aliquot of the first uranium fuel layer while also keeping the radioactivity level within workable limits. After the aliquot was taken from the fuel rod it was dissolved in aqua regia and diluted to ~110 mL and stored in Shielded Cells.

Table 3.6: Information on the three fuel rods sampled at SRNL.

	Sampled Mass (g)	Uranium Mass (g)	Solution Volume (mL)	Initial Enrichment	Final Enrichment
2009 Fuel	~2	0.3242	100	93%	70%
2010 Fuel	1.6743	0.1389	100	93%	75%
2011 Fuel	1.42	0.27	100	45%	33%

The dissolved fuel rod samples are challenging to work with due to the high amount of radioactivity being emitted from the samples as well as the Al and U rich matrix from which the lanthanoids are isolated. The fuel presents challenges to find a proper non-radioactive analogue for the sample to test separation methods, and the high radioactivity requires the separation technique be simple enough that it can be conducted remotely in Shielded Cells by technicians operating manipulators, while still resulting in excellent removal of several key elements, specifically: Al, U, Pu, Cs, Ba, Sr, and Y. The chromatographic separation used for isolating the lanthanoids from trinitite was used as a starting condition to determine the first stage separation for the fuel rod samples.

The initial steps of 2.5 M HNO₃ to 4 M HNO₃ used in the method for trinitite resulted in acceptable separation of the lanthanoids (see Chapter 4), however, for the

fuel rods the Al rich matrix presented a problem. In 2.5M HNO₃, Al³⁺ has a K_d value (partition coefficient) of ~17, comparable to the lanthanoids at ~35 (Strelow et al., 1965). Calibrations performed at SRNL with BHVO-2 (a basalt rock standard) and analyzed with their MC-ICP-MS showed significant elution of Al³⁺ into the lanthanoid section as shown in Fig. 3.4. With a major component of the nuclear fuel sample consisting of Al, this co-elution is unacceptable for subsequent lanthanoid separations.

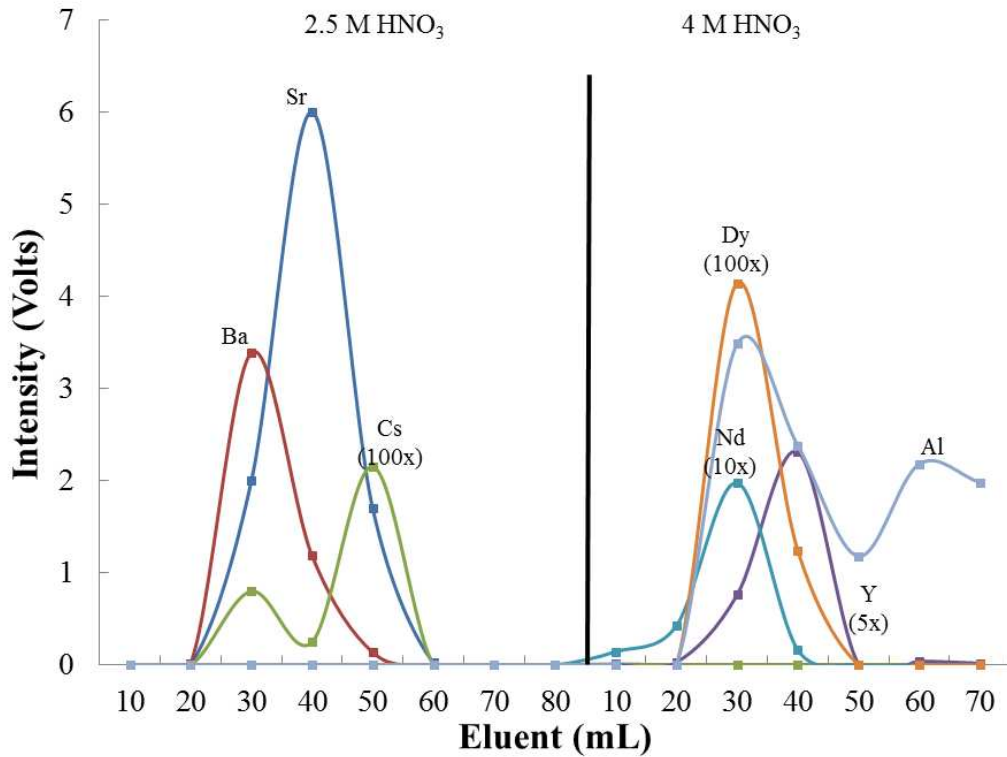


Figure 3.4: Nitric acid column calibration for nuclear fuel samples using BHVO-2 surrogate solution. Samples collected in 10 mL cuts and analyzed on a MC-ICP-MS at SRNL with the intensities reported as voltages.

Switching the starting solution to 2.5M HCl and keeping the 4M HNO₃ final solution was attempted at SRNL to correct for the Al contamination, based on the

lower K_d value of Al^{3+} in HCl compared to HNO_3 (Strelow, 1960). Separation of a surrogate solution using the aforementioned procedure revealed that the Sr cut was eluting with the lanthanoids as shown in Fig. 3.5. Co-elution of Sr with the lanthanoids carries with it additional complications as ^{90}Sr ($t_{1/2} = 30$ years) is a significant source of long-term radiation by producing its daughter product ^{90m}Y ($t_{1/2} = 64$ hours), with a high energy gamma ray.

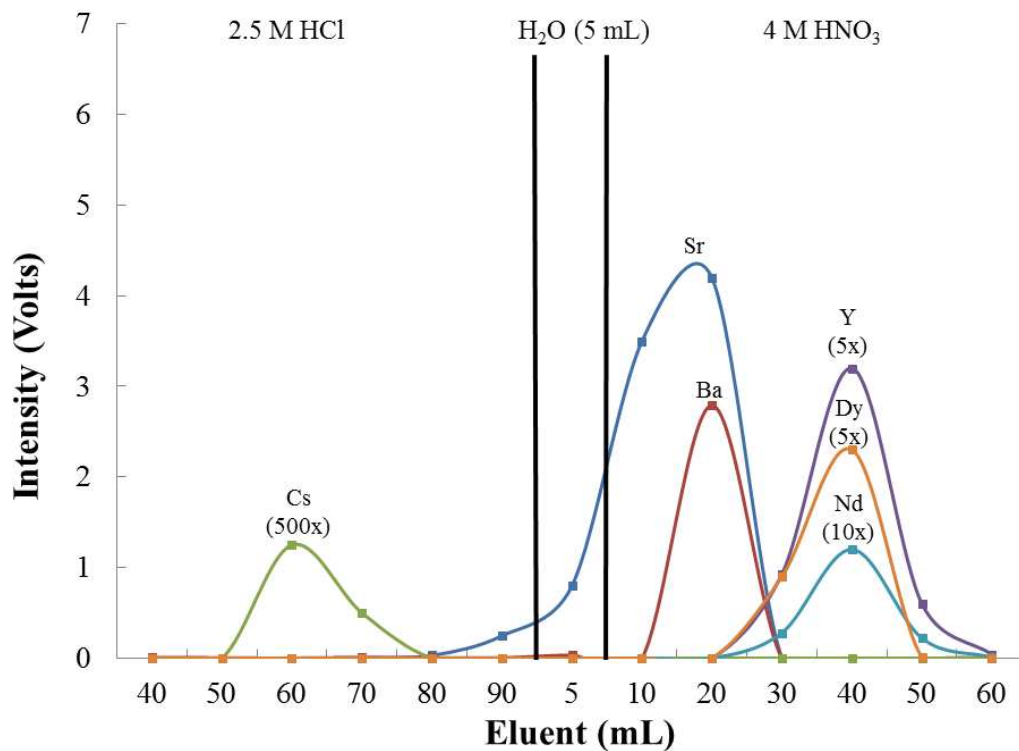


Figure 3.5: Mixed acid column calibration for the nuclear fuel samples using BHVO-2 as a surrogate solution with cuts taken every 10 mL and measured on the MC-ICP-MS with intensities reported as voltages. The first 30 mL showed clear signs of $AlCl_4^-$ and therefore were not measured to protect the instrument.

Separation of a surrogate solution using a combination of the previous two methods proved fruitful for isolating the lanthanoids from the Al and U rich matrix along with separate isolation of the high activity fission products as shown in Fig. 3.6. Uranium has similar K_d s in HCl and HNO_3 of ~ 7 and 10 , respectively (Strelow, 1965;

Strelow, 1959), so is eluted well before the lanthanoids. Due to the shared chemistry of Y and the lanthanoids their separation was not accomplished. After isolating Y from Sr, the 64 hour half-life of $^{90\text{m}}\text{Y}$ enables a wait of ~1 month (720 hours, 11.25 half-lives) for the short-lived species to decay to stable ^{90}Y and no longer pose any health concern. For this work logistical constraints resulted in a wait of 1 year before the next column chromatography could be implemented, more than enough time for $^{90\text{m}}\text{Y}$ to decay away. However, ^{241}Am also has similar chemistry to the lanthanoids and has a particularly long half-life, 432.6 years. The decay of ^{241}Am involves emission of an alpha particle and emission of very weak (<50 keV) gamma rays and therefore does not pose a significant health hazard. Due to alpha emission ^{241}Am does pose a significant contamination risk that must be accounted for in future chemistry. Additionally, the elution of Nd occurring prior to the 4.0 M HNO_3 transition required a change from 2.5 M to 2.0 M HCl and HNO_3 . The reasoning was that by reducing the concentrations of the first two acids the lanthanoids would not elute until after the addition of 4.0 M HNO_3 .

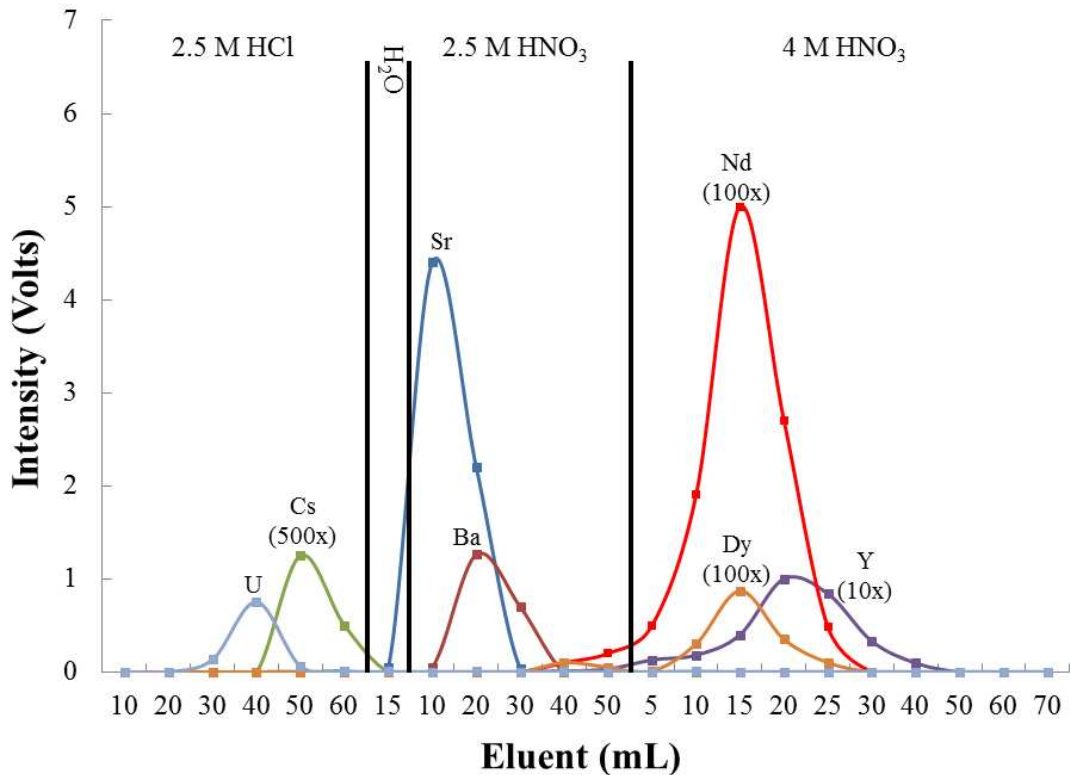


Figure 3.6: Column calibration using BHVO-2 taken before fuel rod separation. Column cut volumes identified by data points and were measured using MC-ICP-MS with intensities reported as voltages.

With the separation procedure calibrated, the materials and chemicals necessary to do the experiment were introduced into the Shielded Cells environment at SRNL. To avoid glass breakage in the Shielded Cells area, we used a commercially available plastic column, R1020 from Environmental Express, instead of quartz columns. The plastic columns shown in Fig. 3.7 had dimensions of 10 cm x 1.5 cm and were filled with the previously mentioned AG-50W x8 200-400 resin prior to being introduced into Shielded Cells. A large plastic reservoir was also attached to the columns to hold the needed acid volumes during elution, and to minimize work required by the manipulator technicians.

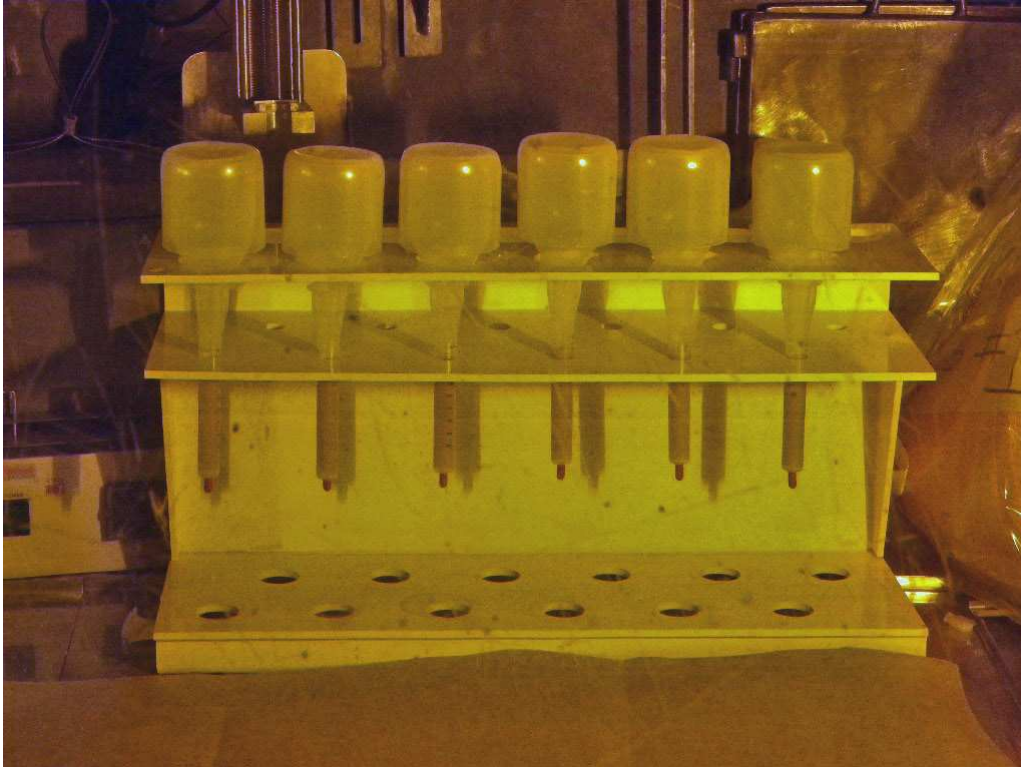


Figure 3.7: Column apparatus inside shielded cells.

A total of 6 samples were separated in Shielded Cells; the fuel rod and its respective blank for the 2009, 2010, and 2011 sampling events. An aliquot of dissolved fuel rod was pipetted from the stock solutions into a glass scintillation beaker. The beaker was previously marked with a line to indicate when 4 mL had been sampled from the stock solution as there was no balance or calibrated pipette to use for the sample transfer process. An estimation of the uncertainty introduced by using this visual method has been conducted in the clean lab at UMD by filling 10 similarly marked beakers, resulting in 3.98 ± 0.16 g. This uncertainty was used in subsequent yield calculations. Also it is important to note that at this stage of the project, yields were not a part of the initial deliverables, if they had been then more appropriate steps would have been taken to insure accurate and precise sampling.

Once the 4 mL aliquot had been transferred solutions were placed in a previously installed oven and heated to dryness. The aluminum rich nature of the samples was apparent from the residual aluminum-chloride salts shown in Fig. 3.8. Samples were further dissolved in ~2 mL of 2.0 M HCl, sealed, and allowed to equilibrate overnight. The next day the samples were loaded on the columns and the separation process initiated.

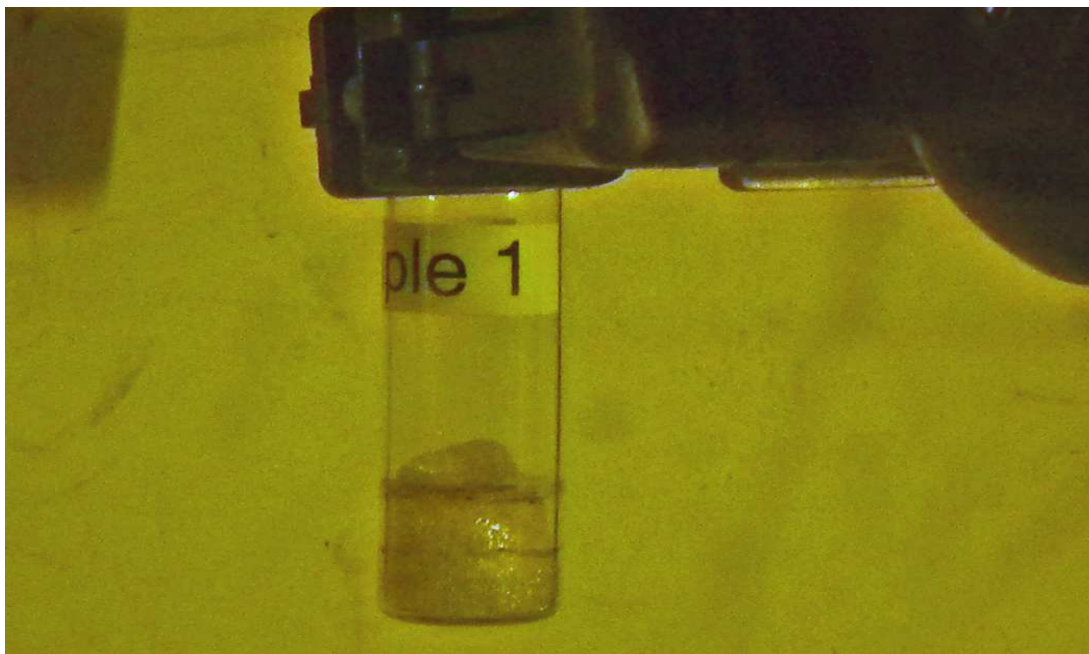


Figure 3.8: The dried down 2009 fuel rod sample. The solid observed is the residual AlCl_3 salt. The black marks correspond to 4 and 2 mL for the sampling and dissolution volumes, respectively.

After the samples were loaded onto the columns the bulk of the first elution acid was added. It was immediately apparent that the process of introducing the columns into the cells resulted in the reservoir for column 1 (containing fuel sample 2009) becoming unseated and it was thus leaking. This issue was discovered before the entire acid volume had been added and, therefore, was minimized by immediately halting the addition of the acid. An immediate reassessment of the situation by the

technicians and researchers commenced. It was determined that the best solution would be to remove the top reservoir from column 1 and add the elution acids in ~5 mL aliquots using transfer pipettes. The leaked acid traveled down the column apparatus towards column 2 (containing the 2009 blank) but was not observed to have traveled any further. The seal of the remaining 5 columns was tested and determined to have not suffered the same weakening as column 1 and after new acid was introduced to replace the lost amount the separation process carried on without incident.

The final volume of the lanthanoid cut in this separation procedure was ~50 mL which was stored in Shielded Cells for approximately 3 months to ensure complete decay of $^{90\text{m}}\text{Y}$. Following this step the solutions were removed and repackaged due to Shielded Cells contamination on the outer surface of the containers. Once cleaned, a 1 mL aliquot was taken from each sample and blank and was screened using High Purity Germanium (HPGE) gamma-ray detection to determine the approximate amount of radioactivity in each sample and the results are reported in Table 3.7. Non-gamma ray emitters (such as ^{151}Sm and all Pm isotopes) would not be detected using HPGE and they do not pose a significant health risk due to their low energy beta emissions. Following the HPGE analysis, safety personal at SRNL determined that only 1 mL of solution would be taken from the 50 mL stock for future lanthanoid separations.

Table 3.7: Results from a cursory HPGE analysis on 1 mL aliquots of the lanthanoid section removed from Shielded Cells.

	2009 Fuel Sample (dpm)	2009 Blank (dpm)	2010 Fuel Sample (dpm)	2010 Blank (dpm)	2011 Fuel Sample (dpm)	2011 Blank (dpm)
¹³⁴ Cs	0	0.9 ± 0.1	0	21 ± 1	0	0
¹³⁷ Cs	57 ± 4	210 ± 10	3400 ± 200	4100 ± 200	5800 ± 300	5.9 ± 0.4
¹⁵² Eu	0	0	81 ± 5	0	0	0
¹⁵⁴ Eu	10800 ± 500	71 ± 4	11800 ± 600	590 ± 30	4200 ± 200	0
¹⁵⁵ Eu	2100 ± 400	14 ± 3	1600 ± 300	120 ± 20	1300 ± 300	0
²⁴¹ Am	392 ± 5	3.8 ± 0.4	990 ± 50	33 ± 5	3000 ± 200	0

3.3.3 Chromatographic Separation of the Lanthanoids

Separation of the individual lanthanoids is a much more complex task than isolating the lanthanoids from their bulk matrix due to their identical oxidation state of 3⁺. Therefore, the most effective separation technique is based on their slightly different ionic radii, which decreases from light to heavy masses. Several techniques have been developed which separate the lanthanoids using high pressure liquid chromatography (Sivaraman et al., 2002) (HPLC) and traditional non-pressurized (Hidaka et al., 2009; Hidaka and Masuda, 1988) and pressurized column chromatography (Marsh, 1967; Eugster et al., 1970; Maas and McCulloch, 1990). The presence of radioactive Eu isotopes and ²⁴¹Am in the fuel samples requires that the second stage separation be conducted in a radiation hood in an approved area at SRNL, effectively eliminating the use of any pressurized system. Additionally, time constraints on technician and researcher work hours resulted in requiring that the entire separation occur within 12 hours or be broken up into multiple days to be completed. This constraint resulted in using gravity fed columns for the lanthanoid separations.

The different sizes of the lanthanoids allow adequate separation. The primary method to exploit the differences in ionic radii is to use chelators, molecules designed to surround specific elements in a cage-like formation, to isolate the lanthanoids by preferentially bonding with the smaller lanthanoids compared to the larger lanthanoids. The two methods investigated for the second separation step included the use of an extraction chromatographic Ln resin, produced by Eichrom, and cation exchange resin using the chelator α -hydroxyisobutyric acid (α -HIBA) as the eluent.

Ln resin consists of di(2-ethylhexyl) orthophosphoric acid (HDEHP) bound to a hydrophobic support matrix. The solid HDEHP preferentially targets the heavier lanthanoids, resulting in an elution order of La>Ce>Pr>Nd>Pm>Sm>Eu>Gd when eluting with HCl and HNO₃. The Ln resin has been used to perform separations of Nd from Sm (Pin and Zaldugui, 1997) and Gd from Sm (Hidaka et al., 2009) for geochemical age dating and neutron fluence calculations.

The Geology department at UMD had a previously existing method for the analysis of Nd and Sm isotopes similar to the Pin and Zaldugui (1997) method and was an ideal starting point for the isolation of Nd, Sm, and Gd. The method used columns, 7.5 x 0.6 cm, filled with Ln resin and eluted with varying concentrations of dilute HCl, typically 0.25/0.34/0.7 M HCl for Ce/Nd/Sm, respectively. The method was not designed for collection of Gd, so additional 0.7 M HCl was added followed by elution with 1 M HCl to reduce the Eu contamination and isolate the Gd cut. The results from these tests were not successful, the peaks of Sm/Eu/Gd were not resolvable, resulting in significant Eu contamination in the Gd and Sm peaks. Other work by Hidaka and Yoneda (2009) obtained Gd cuts which were not contaminated

with Sm, but they were unable to also remove the Eu contamination shown in Fig. 3.9.

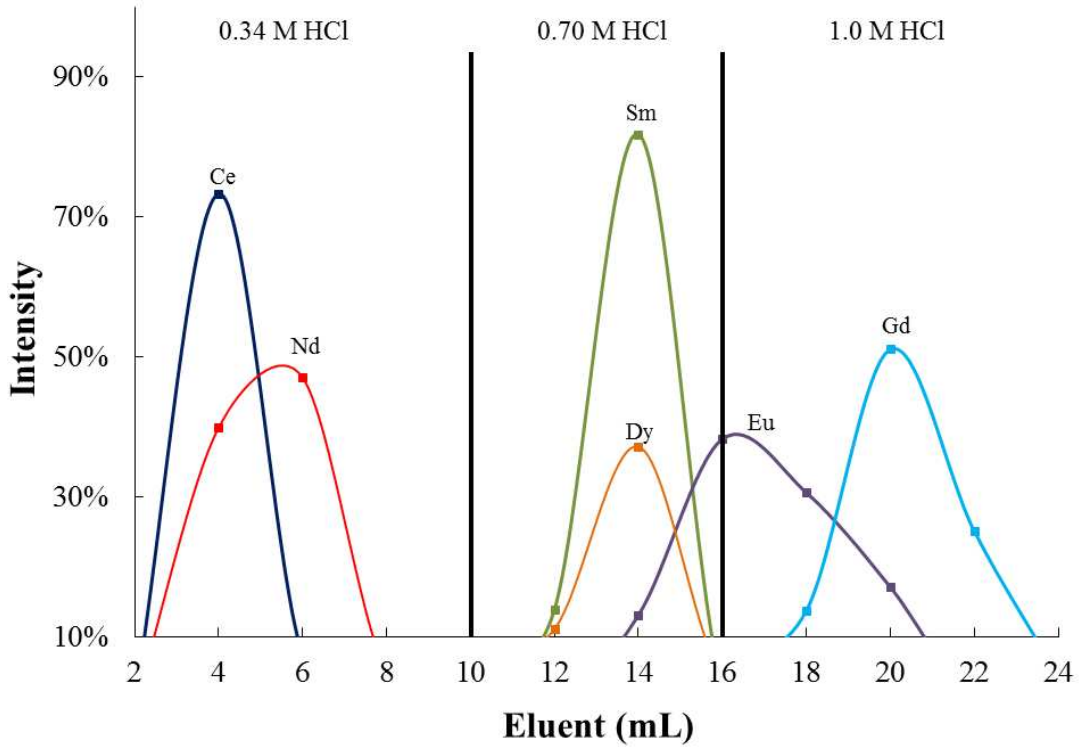


Figure 3.9: Separation using HCl with Ln resin. Samples taken every 2 mL and analyzed using SC-ICP-MS.

However, for natural samples the Eu contamination is not important as Eu only has two naturally occurring, stable isotopes, $^{151,153}\text{Eu}$, which are not isobars with either Sm or Gd. In the fuel samples the ^{151}Eu will interfere with ^{151}Sm and the radioactivity from the $^{154,155}\text{Eu}$ will present significant concerns for work at non-radioactive material labs where the mass spectrometers at both SRNL and UMD are located.

The method that was ultimately used for the trinitite and fuel rod lanthanoid separation involved the use of the same cation exchange resin as in the 1st stage

separation, but changed to the NH_4^+ form with α -HIBA as the eluent. The use of α -HIBA as an eluent to chromatographically separate the lanthanoids was first developed by Choppin and Silva (1956) using heated columns and Dowex 50-x12, identical to the AG-50W resin. The heated columns, however, are logistically impractical to implement at SRNL. Other studies determined that α -HIBA would nevertheless provide adequate separation of the lanthanoids at room temperature with and without pressurizing the columns (Smith and Hoffman, 1956; Marsh, 1967). This procedure has also been used in Oklo and Alligator River samples to determine perturbations to lanthanoid isotopic compositions due to past fission events that naturally occurred 1-2 billion years ago (Maas and McCulloch, 1990; Hidaka and Masuda, 1988).

Typically, the columns used are on the order of 0.2 x 30 cm with resin of either x4 or x8 cross-linkage, resulting in the columns flowing at approximately 1 mL/40 min without pressurization. Again, the limitations of the radiation lab prevented the use of a pressurized system, so the chromatographic separations were conducted under normal atmospheric pressure. The final column dimensions used in this work were 0.3 x 28 cm with AG-50W x8 200-400 mesh resin converted to the NH_4^+ form by treating the resin with several column volumes of ~50% NH_4OH . Prior to column chemistry the resin was equilibrated with ~5 mL of the selected eluent with sample load volumes of 0.2 mL. The eluting solutions used were 0.15 M, 0.225 M, and 0.53 M α -HIBA buffered to pH 4.7 using concentrated NH_4OH and measured via a pH meter.

The column elution rate forced the adoption of a 2-part method for Gd/Sm/Nd separations, due to the limit of ~10 hours per day that a column could be eluting. Therefore the 0.15 M α -HIBA solution was used first to isolate the Gd section and to discard the majority of Eu shown in Fig. 3.10A. The column was then rinsed with ~15 mL of 0.53 M α -HIBA to remove the remaining lanthanoids. Subsequently the column was cleaned with several column volumes of 6 M HCl, reconverted to NH_4^+ form, and equilibrated for the next sample. Finally Nd and Sm were eluted using the 0.225 M solution, shown in Fig. 3.10B. After Nd elution the column was cleaned with the previously mentioned protocol.

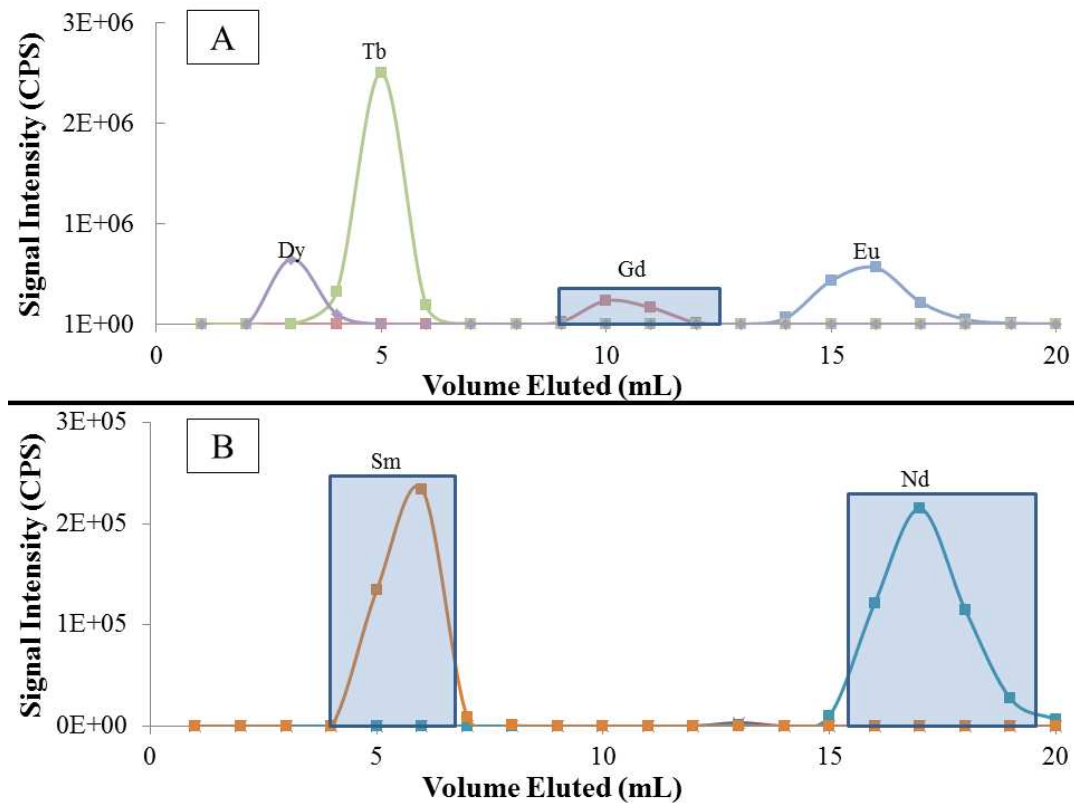


Figure 3.10: A) 0.15 M α -HIBA and B) 0.225 M α -HIBA. Shaded regions refer to collection volumes for finalized 2nd stage column procedure trinitite and fuel samples. Samples were taken every 1 mL and were analyzed with SC-ICP-MS with intensities reported as CPS.

Multiple column calibrations were obtained and the resultant graphs show that the elution peaks are reproducible to the 1 mL level. Yields for the entire column setup are only on the order of 60-80 % for Nd, Sm, and Gd. Reasons for the low yields are possibly due to ending the collection of the target elements as a precaution to reduce the possible contamination of neighboring lanthanoids, which in all cases contained radioactive species. This contamination would have prevented the samples from being analyzed at SRNL, which at the time was the planned analysis method.

Due to instrument related hardware problems, logistical constraints, and departure of key personnel at SRNL, aliquots of the fuel samples were transported to UMD and the separation procedure was conducted in a radiation lab in the Chemistry Department. The Nu Plasma MC-ICP-MS in the Geology Department was authorized to perform analyses on radioactive solutions as a backup plan and ultimately, when the instrument at SRNL did not come back online in a timely manner, the analyses were conducted at UMD and are reported in Chapter 5. A summary of the complete separation procedure for trinitite and the nuclear fuels can be found in Table 3.8.

Table 3.8: Final separation method for trinitite and fuel samples.

Step		Trinitite	Nuclear Fuels
1st Stage	Wash	55 mL 2 M HNO ₃ - 5 mL 4 M HNO ₃	60 mL 2 M HCl - 15 mL H ₂ O - 50 mL 2 M HNO ₃
	Lanthanoid Collection	30 mL 4 M HNO ₃	50 mL 4 M HNO ₃
2nd Stage	Wash	8 mL 0.15 M α-HIBA	8 mL 0.15 M α-HIBA
	Gd	4.25 mL 0.15 M α-HIBA	4.25 mL 0.15 M α-HIBA
	Wash	8 mL 0.15 M α-HIBA	8 mL 0.15 M α-HIBA
	Lanthanoid Recovery	10 mL 0.53 M α-HIBA	10 mL 0.53 M α-HIBA
	Wash	3 mL 0.225 M α-HIBA	3 mL 0.225 M α-HIBA
	Sm	3.75 mL 0.225 M α-HIBA	3.75 mL 0.225 M α-HIBA
	Wash	9 mL 0.225 M α-HIBA	9 mL 0.225 M α-HIBA
	Nd	4.5 mL 0.225M α-HIBA	4.5 mL 0.225M α-HIBA

All samples were analyzed on the Nu Plasma HR MC-ICP-MS in the Geology Department at UMD, with the exception of the Gd validation and trinitite measurements. These were performed on the Nu Plasma HR MC-ICP-MS at SRNL. The results for the trinitite analyses can be found in Chapter 4 and the nuclear fuel samples in Chapter 5.

Chapter 4: Trinitite¹

[1]: N. Sharp wrote all materials in this chapter. P. M. Piccoli and D. T. Borg conducted all electron probe analyses. D. T. Borg and R. D. Ash conducted the laser ablation analyses and lanthanoid abundance charts and figures. B. W. Ticknor and N. Sharp conducted the Gd analyses at SRNL. N. E. Sharp performed all chemistry, isotopic data calculations, and neutron fluence calculations. This chapter has been submitted for publication and is currently in revision as:

Sharp, N., McDonough, W.F., Ticknor, B.W., Ash, R.D., Piccoli, P.M., Borg, D.T., in revision, Rapid Analysis of Trinitite with Nuclear Forensic Applications for Post-Detonation Material Analyses. *Journal of Radioanalytical and Nuclear Chemistry*

4.1 Abstract

Analysis of post-nuclear detonation materials provides information on the type of device and its origin. Compositional analysis of trinitite glass, fused silicate material produced from the above ground plasma during the detonation of the Trinity nuclear bomb, reveals gross scale chemical and isotopic heterogeneities indicative of limited convective re-homogenization during accumulation into a melt pool at ground zero. Regions rich in weapons grade Pu have also been identified on the surface of the trinitite sample. The absolute and relative abundances of the lanthanoids in the glass are comparable to that of average upper crust composition, whereas the isotopic abundances of key lanthanoids are distinctly non-normal. The trinitite glass has a non-normal Nd isotope composition, with deviations of $-1.75 \pm 0.60 \text{ } \epsilon$ (differences in parts in 10^4) in $^{142}\text{Nd}/^{144}\text{Nd}$, $+2.24 \pm 0.75 \text{ } \epsilon$ in $^{145}\text{Nd}/^{144}\text{Nd}$, and $+1.01 \pm 0.38 \text{ } \epsilon$ in $^{148}\text{Nd}/^{144}\text{Nd}$ (all errors cited at 2σ) relative to reference materials: BHVO-2 and Nd-Ames metal. Greater isotopic deviations are found in Gd, with enrichments of $+4 \pm 1 \text{ } \epsilon$ in $^{155}\text{Gd}/^{160}\text{Gd}$, $+4.19 \pm 0.75 \text{ } \epsilon$ in $^{156}\text{Gd}/^{160}\text{Gd}$, and $+3.48 \pm 0.52 \text{ } \epsilon$ in

$^{158}\text{Gd}/^{160}\text{Gd}$ compared to BHVO-2. The isotopic deviations are consistent with a ^{239}Pu based fission device with additional ^{235}U fission contribution and a thermal neutron fluence between 1.4 and 0.97×10^{15} neutrons/cm².

4.2 Introduction

Today, a well-documented chemical and isotopic database is needed to assign origin and provenance to materials from a nuclear event. Characterizing the fissile material and composition of an unknown device are central efforts of nuclear forensics which can be challenging in the case of an urban event, given the myriad of debris types possible from the local environment. In the case of a nuclear device, non-natural isotopic fingerprints have the potential to provide insights into the history, source, and origin of interdicted materials. It is critical to observe and understand the effects of a fission event on less-complicated material before embarking on analyzing complex urban debris. Analyses of trinitite, fused silica-glass from the Trinity test event, presents nuclear forensic investigators with ideal post-detonation material where the composition of the nuclear device and source material are well-known, enabling validation of testing methods designed to determine a device's original makeup. In this study, we present chemical and isotopic data on trinitite and compare our results with Trinity's known characteristics.

In the early hours of 16 July 1945 the atomic age began with the Trinity nuclear bomb detonation at the White Sands Proving Ground, New Mexico. The bomb, a ^{239}Pu implosion device, produced a fireball of 10^4 K and a debris cloud that reached a height of 11 km within minutes, and eventually as high as 21 km (Eby et al., 2010). The debris cloud, consisting of material from the detonation tower, the

bomb itself, and adjacent desert sand, precipitated onto the desert floor and cooled rapidly, yielding a glassy surface, trinitite, that surrounded the explosion site.

The four varieties of trinitite include: green glass trinitite, pancake trinitite, red trinitite, and bead trinitite. All types originate from arkosic sand and are composed of quartz, microcline, albite, muscovite, actinolite, and calcite (Eby et al., 2010). The green glass variety (analyzed in this study) consists of glass with no observable unaltered original sand material. This sample was likely produced from the combination of proximal sand near ground zero melting into a glass and falling material from the debris cloud (Belloni et al., 2011). However, due to remediation of the test site, the exact location relative to ground-zero for this trinitite sample is unknown.

Trinitite contains fissile materials, neutron activated materials, and pieces of the detonation tower and the bomb itself, such as the uranium tamper and lead casing (Fahey et al., 2010; Belloni et al., 2011; Bellucci and Simonetti, 2012). Recently uranium and lead isotopic signatures of the bomb have been investigated (Bellucci et al., 2013a, 2013b). Here we report on the chemical and isotopic composition of trinitite, both spatially resolved laser ablation and solution analyses, using inductively coupled plasma mass spectrometry. During detonation, fission products of both light and heavy isotopes (e.g., 80-105 amu and 130-160 amu, respectively) are produced. The tail of the heavy isotope product distribution includes the middle members of the lanthanoids. The relative isotopic abundances of lanthanoids produced via fission differ from those occurring naturally. The mixing of fission lanthanoids with natural material produces measurable enrichments and depletions in isotopic abundances

when compared to natural material. The resultant altered isotopic abundances can be used to identify the device's fissile material, given a successful deconvolution of the fissile and natural isotopic compositions.

In this study the concentration of major element oxides and lanthanoids were determined using a combination of electron probe micro-analysis (EPMA) and laser-ablation inductively-coupled mass spectrometry (LA-ICP-MS). The isotopic composition of Gd and Nd were determined by sample dissolution followed by chromatographic separation of the elements of interest using multi-collector inductively coupled plasma mass spectrometry (MC-ICP-MS). The utility of rapid analysis of a post-detonation material via EPMA and LA-ICP-MS provides an initial qualitative screening that readily identifies specific targets for more thorough analyses, in this case using MC-ICP-MS for high-precision isotopic ratio determinations.

4.3 Experimental methods

The trinitite sample studied is entirely glass and contains little to no original sand. The green glass has a smooth top which corresponds to the surface facing the atmosphere during deposition. Deeper into the sample are vesicles with increasing frequency with greater depth. Samples are highly heterogeneous in composition with vesicles accounting for approximately 33% of the total trinitite volume (Hermes and Strickfaden, 2005). A ~1 g piece was broken off of the bulk pool glass and subsequently split into two fractions by hand. Both were mounted in epoxy: one

piece was mounted with the smooth surface exposed; the other piece was mounted perpendicular to the smooth surface as observed in Fig. 4.1.

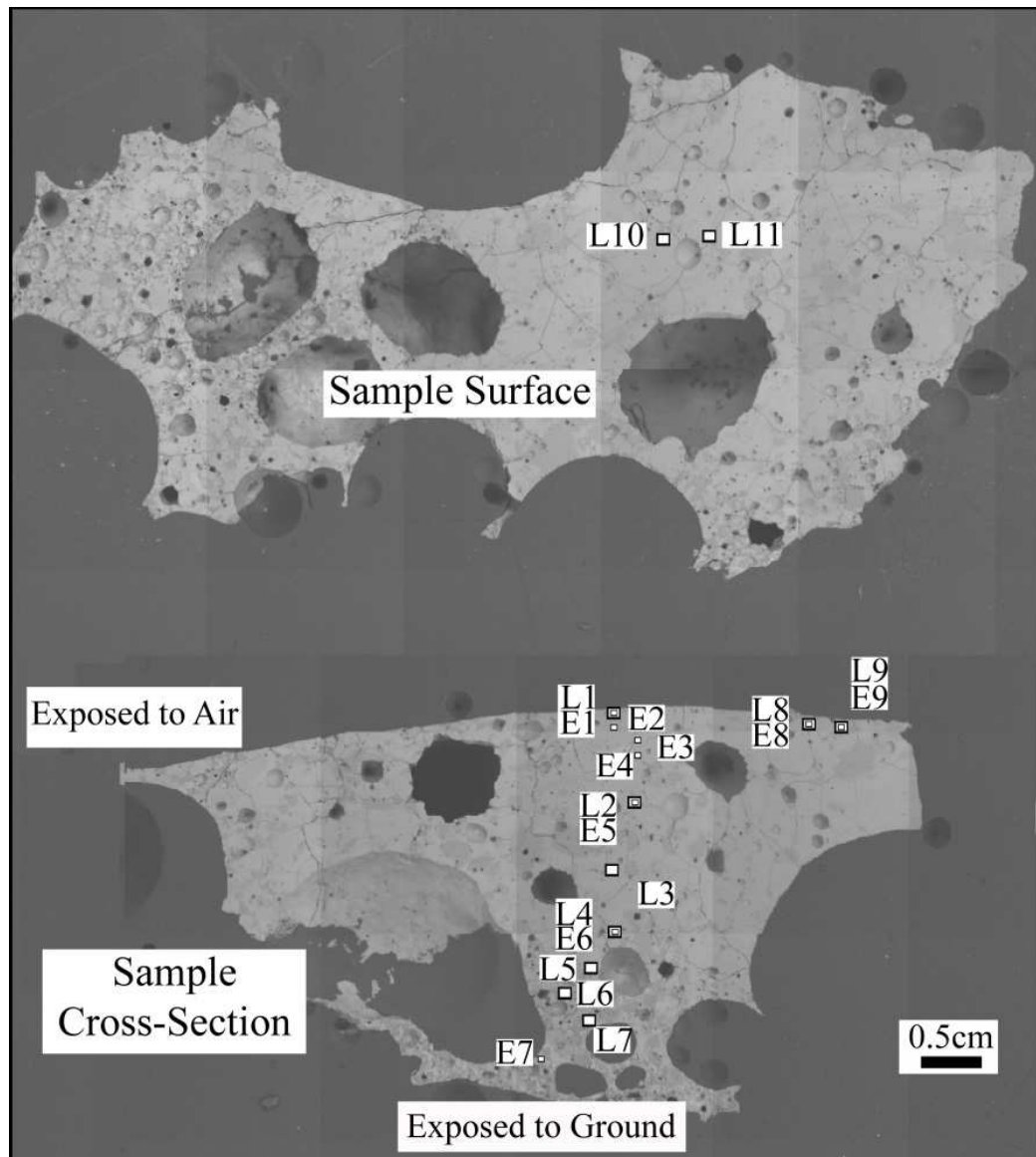


Figure 4.1: BSE image of the two pieces of trinitite mounted in epoxy. The piece on the top is the smooth surface of a piece of trinitite while the bottom image is the cross sectional piece in Fig. 4.2. The large boxes are LA-ICP-MS sites and the smaller boxes are EPMA sites.

4.3.1 Electron microprobe

The JXA-8900 SuperProbe was used to determine major element concentrations via wavelength dispersive spectrometry (WDS). The analyses were carried out with a 10-20 μm spot size, accelerating voltage of 15 kV, and a 20 nA cup current. Data was recalculated using a ZAF algorithm using orthoclase (K_2O , Al_2O_3 , SiO_2), rhodonite (MnO), and kakanui hornblende (CaO , MgO , FeO , TiO_2) as primary standards with Yellowstone rhyolite as a secondary standard. Backscattered electron (BSE) images were also acquired.

4.3.2 Sample Digestion and Chromatography

For Nd and Gd isotope analysis a 0.1 g piece of glassy trinitite (no original desert floor material) underwent an acid digestion procedure consisting of a mixture of concentrated HNO_3 and HF in addition to 100 μL of HClO_4 in a sealed 15 mL Teflon beaker. Two 0.05 g BHVO-2 SRMs underwent the same procedure in separate beakers. An analytical blank was also prepared and treated with the same chemistry procedure and resulted in Nd and Gd blank concentrations of 6 pg. Teflon distilled acid was used for sample digesting, chromatography, and sample analysis.

Sample digestion was performed on a hotplate set to 180°C for 72 hours. Subsequently the beakers were opened and the solutions were dried to a hard residual cake; 6 M HCl was added to each beaker, and they were then resealed and heated for an additional 24 hours. Following this heating, the beakers were opened and allowed to dry again, and the 6 M HCl step was repeated. After the 3rd drying step 2 mL of quartz distilled 2.5 M HCl was added to the samples.

Lanthanoids were separated from the bulk matrix with a 12cm x 2cm Dowex AG50W x8 400 mesh cation exchange column in H⁺ form. The 2 mL solution of 2.5 M HCl was added to the column and 50 mL of 2.5 M HCl wash was added and followed by 45 mL of 4.5 M HNO₃, with the last 35 mL collected as the REE cut. The REE cut was then dried down and reconstituted in 0.5 mL of 0.15 M α -hydroxyisobutyric acid (α -HIBA) buffered at pH 4.7 using NH₄OH.

Individual lanthanoids were separated using a 30 cm x 0.5 cm column filled with Dowex AG50W x8 400 mesh cation exchange resin treated with concentrated NH₄OH to convert the resin from H⁺ to the NH₄⁺ form. The 0.5 mL sample solution was loaded and followed by a series of elution steps with α -HIBA isolating the Nd and Gd cuts. The Nd and Gd cuts were then dried down and then dissolved with 2 mL of 0.8 M HNO₃. Isotope analysis samples were prepared by taking 300 μ L of the cut solution diluted with 1.2 mL of 0.8 M HNO₃.

4.3.3 LA-ICP-MS and MC-ICP-MS

The laser ablation analyses were conducted on a single collector, sector field, Element 2 (Thermo-Finnigan, Bremen, Germany) ICP-MS coupled to a 213 nm wavelength laser ablation system (UP213, New Wave Research) with operating conditions detailed in Table 4.1. Optimization of the instrument included tuning the ion lenses and ICP-MS torch position to maximize the signals at masses 43, 139 and 178 while maintaining $^{238}\text{U}^{16}\text{O}/^{238}\text{U} \leq 0.2\%$. Individual analysis included a 30s background acquisition followed by 30s spot analysis.

An external standard of NIST610 was analyzed in duplicate at the beginning and end of each data acquisition of ~16 spots analyses of unknowns. Differences in beam diameter were due to higher concentrations of lanthanoids in NIST610 compared to trinitite. The absolute concentration of Ca obtained from EPMA analyses functioned as an internal calibrant for data processing with LAMTRACE (Jackson, 2008). For laser ablation sites not constrained by EPMA determined Ca concentration, the laser ablation data was corrected by normalizing the ablation yields of unconstrained Ca sites to the ablation yields of EPMA constrained Ca sites. Plutonium concentrations are based on the assumption that Pu ablates at approximately the same efficiency as U. This correction allowed for the determination of a concentration/signal ratio for U at each site and to apply that factor to the Pu signal to determine a first-order approximation of Pu concentration.

Table 4.1: The instrument operational conditions used for LA-ICP-MS analysis.

New Wave Nd: YAG laser parameters	
Wavelength	213 nm
Energy density	2-3 J cm ⁻²
Pulse duration	5 ns
Carrier gas	He
Ablation pattern	Single spot
Laser beam size (diameter)	40 μm (NIST 610), 80 μm (Trinitite)
Repetition rate	7 Hz
Thermo Finnigan Element2 ICP-MS parameters	
RF power	1250 W
HV	8 kV
Scan optimization	Speed (dynamic peak-hopping mode)
Mass resolution	300 (m/Δm)
Detection mode	Analog and counting
Sampler cone	1.0 mm Al-alloy
Skimmer cone	0.7 mm Al-alloy
Cool gas flow	16 L min ⁻¹ Ar
Auxiliary gas flow	1.5 L min ⁻¹ Ar
Sample gas flow ^a	0.8 L min ⁻¹ Ar
Carrier gas flow ^a	0.6 L min ⁻¹ He
Dwell time	5 ms at masses: 43, 137, 139, 140, 141, 142, 143, 144, 145, 146, 147, 148, 149, 150, 151, 152, 153, 154, 155, 156, 157, 158, 159, 160, 161, 162, 163, 164 10ms at masses: 165, 166, 167, 168, 169, 170, 171, 172, 173, 174, 175, 176

^aThese gas flows were coupled at a T-junction prior to the plasma torch.

Isotope analyses for Nd and Gd were conducted at the University of Maryland Geology (UMD) department and the Savannah River National Laboratory (SRNL) using Nu Plasma HR MC-ICP-MS (Nu Instruments, Wrexham, UK) with operating parameters listed in Table 4.2. The instrument at UMD was coupled to an Aridus I (Cetac Technologies, Omaha, NE) desolvating nebulizer while a DSN-100

desolvating nebulizer (Nu Instruments) was coupled to the mass spectrometer at SRNL. Measurement parameters were identical at each location with 5 blocks of 20 10 second integration points with a mandatory 30 second background determination at the beginning of each block.

Table 4.2: The instrument operational conditions used for MC-ICP-MS analysis

Nu Plasma HR MC-ICP-MS parameters^a	
RF power	1300 W
Reflected power	5 W
Accelerating voltage	4000 V
Cool gas flow	13 L min ⁻¹ Ar
Auxiliary gas flow	1 L min ⁻¹ Ar
Sweep gas flow ^b	2.75 L min ⁻¹ Ar
N ₂ gas	10 mL min ⁻¹ N ₂
Aspiration rate	50 µL min ⁻¹
Integration time	10s
Blocks	5
Background time	30s between blocks

Nu Plasma HR2 MC-ICP-MS parameters^c	
RF power	1300 W
Reflected power	0 W
Accelerating voltage	6000 V
Cool gas flow	13 L min ⁻¹ Ar
Auxiliary gas flow	0.8 L min ⁻¹ Ar
Sample gas flow ^d	4.5 L min ⁻¹ Ar
Aspiration rate	100 µL min ⁻¹
Integration time	10s
Blocks	5
Background time	30s between blocks

^a University of Maryland – Nd isotopes

^b Gas flows were set using an Aridus I

^c Savannah River National Laboratory – Gd isotopes

^d Gas flows were set using a DSN-100

Isobaric interferences for Nd consisted of Ce and Sm at masses: 142, 144, 148, and 150. During sample acquisition, ¹⁴⁰Ce remained stable at ≤ 1.3 mV while ¹⁴⁷Sm remained at less than 1×10^{-2} mV; the contribution from Sm isobars was

negligible, whereas interference from Ce required a correction to ^{142}Nd using $^{142}\text{Ce}/^{140}\text{Ce} = 0.1256$ (Chang et al., 1995).

Instrument induced mass fractionation for Nd was corrected on-line by normalizing to $^{146}\text{Nd}/^{144}\text{Nd} = 0.7219$. Normalizing using 0.7219 is not ideal due to fission production of ^{146}Nd and ^{144}Nd , however, the comparable fission isotopic ratio of 0.6667 permits us to make comparisons using the original 0.7219 value for mass fractionation correction. In the case of Gd a concentration standard was mass fractionation corrected using $^{156}\text{Gd}/^{160}\text{Gd} = 0.9361$ and the mass bias factor from this correction was used to correct the BHVO-2 and trinitite data. Due to low signals of ^{152}Gd and ^{154}Gd (80 mV and 8 mV, respectively) those isotopes are not reported.

4.4 Results

A vertical cross section through a ~1 cm thick piece of trinitite glass reveals chemical and physical heterogeneities. The sample top surface (i.e., that facing the atmosphere) and subjacent region contains silicate glass populated with quartz grains that show signs of incipient melting. A vertical gradient in the amount and size of vesicles with increasing sample depth into the puddle glass is observed in Fig. 4.2. The lower portion of the cross section (3.0-5.5 mm below the surface) contains a higher abundance of partially-melted quartz grains. The incipiently melted material present on the bottom of the sample most likely remained on the desert floor and was not incorporated into the debris cloud, resulting in less overall melting and more vesicles. The quartz-rich zones appear more pronounced lower in the cross-section.

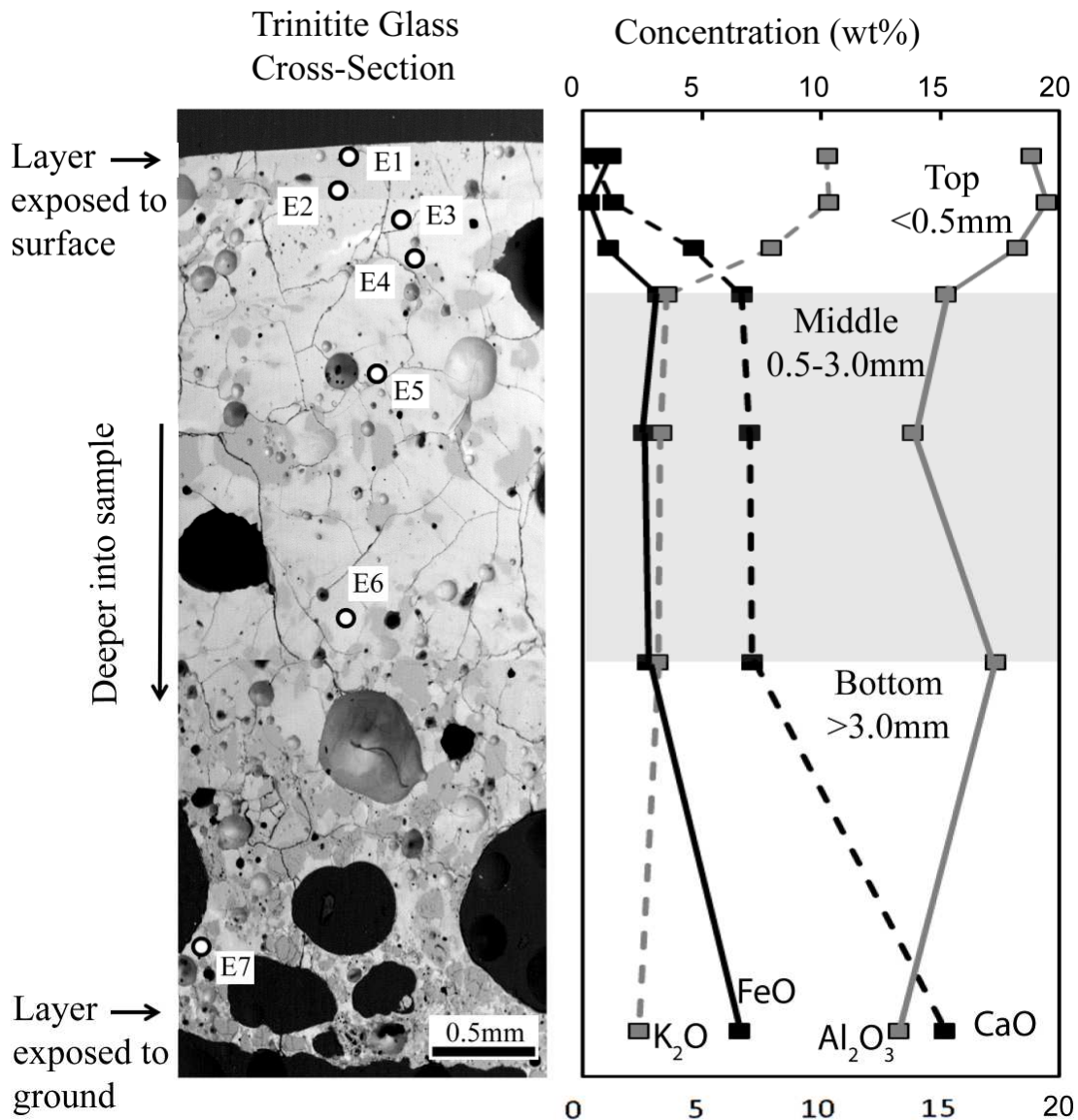


Figure 4.2: Cross section BSE image of trinitite showing an increase in size and number of vesicles with depth and EPMA sites marked E1-7. Darker shades of gray represent partially melted quartz grains. Uncertainty in the concentration measurements are on the order of $\pm 1\%$ (2σ).

Major oxide compositions determined using EPMA are listed in Table 4.3.

There is marked bulk compositional heterogeneity of the cross section of trinitite glass (Fig. 4.2) with CaO and FeO concentration increasing with depth and K₂O and Al₂O₃ concentrations decreasing with depth. We observed positive correlation of

FeO vs CaO and K₂O vs Al₂O₃ and negative correlation of FeO vs Al₂O₃ and CaO vs K₂O. Lanthanoid concentrations obtained via LA-ICP-MS are listed in Table 4.4.

Trinitite glass is comparable to the average upper crust composition as shown in Fig. 4.3 (Rudnick and Gao, 2003), however, some domains show marked depletion, possibly reflecting lithological variations in the available desert floor and are likely due to high calcite and quartz (L9) contributions.

Table 4.3: Major element oxide composition obtained via EPMA analysis of trinitite.

	E1 ^a	E2	E3	E4	E5	E6	E7	E8	E9
<i>Oxide wt%</i>									
SiO ₂	64.74	64.96	65.43	67.72	68.14	65.52	57.10	65.03	96.42
TiO ₂	0.08	0.03	0.08	0.54	0.45	0.37	0.92	0.62	b.d. ^b
Al ₂ O ₃	18.81	19.46	18.21	15.25	13.86	17.31	13.25	11.82	0.15
FeO	1.15	0.28	1.05	3.15	2.53	2.71	6.57	2.55	0.16
MnO	0.02	b.d. ^b	0.02	0.07	0.06	0.06	0.09	0.05	b.d. ^b
MgO	0.39	0.03	0.44	1.30	1.06	1.00	2.74	0.94	0.06
CaO	0.38	1.27	4.62	6.66	7.00	7.10	15.15	8.68	0.32
Na ₂ O	2.14	2.61	2.05	2.09	1.82	2.21	1.71	2.04	0.20
K ₂ O	10.25	10.32	7.92	3.55	3.32	3.17	2.32	3.05	0.30
Total	97.96	98.96	99.82	100.33	98.24	99.45	99.85	94.78	97.61

^aLocations in Figure 4.2

^bBelow detection.

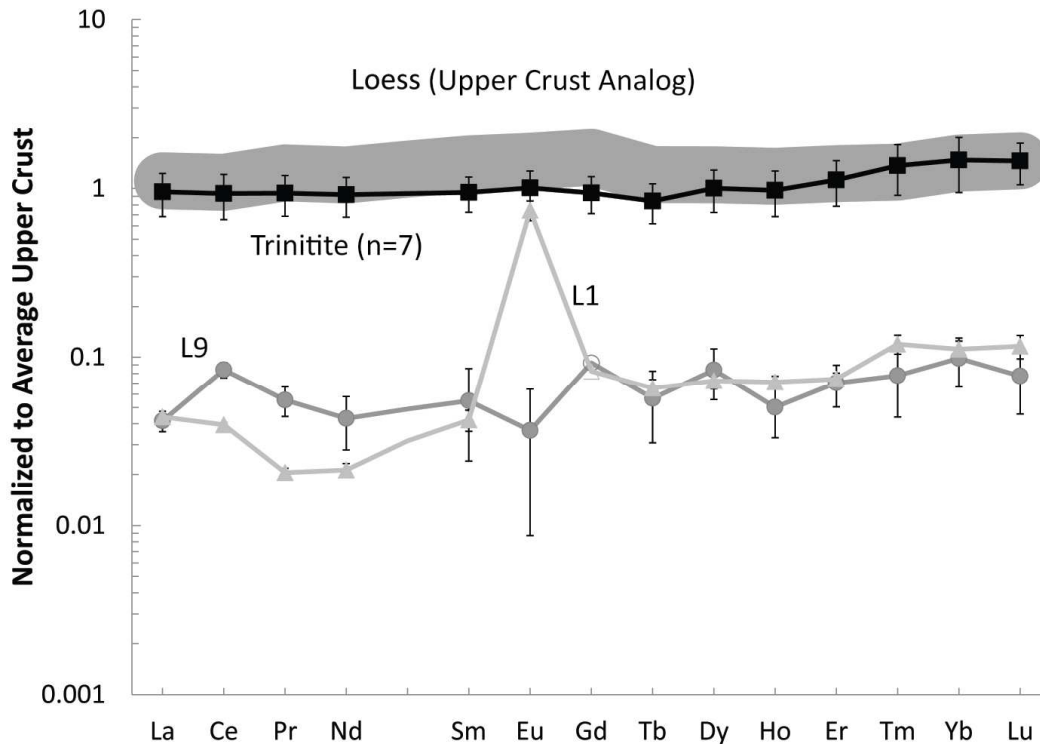


Figure 4.3: Comparison of lanthanoid concentrations obtained with LA-ICP-MS on trinitite. Values are normalized to upper crust values from Rudnick and Gao (2003). Loess (grey region), a glacial dust which is a naturally produced sample of the average upper continental crust (Barth et al., 2000), are compared to trinitite. Average trinitite values (black squares) represent average from n=7 analyses, with L1 and L9 plotted separately. Uncertainties shown are 2σ . The Gd values for L1 and L9 are below detection and are therefore empty markers.

Table 4.4 shows ^{238}U and ^{239}Pu concentrations vary by an order of magnitude and are not correlated with other elemental concentrations in the sample. In general, all sites analyzed exhibited a $^{240}\text{Pu}/^{239}\text{Pu}$ ratio of ≤ 0.03 , which is indicative of weapons grade Pu (Moody et al., 2005), a strong marker for the fissile material used in the device. In-situ laser ablation also identified isotopic anomalies in Gd isotopic ratios, shown in Fig. 4.4, which provided strong evidence that more rigorous analyses of the trinitite sample were warranted and would likely yield detailed information about the fission device.

Table 4.4: Trace element results obtained via LA-ICP-MS with concentrations in $\mu\text{g/g}$ obtained via ablation yield normalization.

	L1 ^a	L2	L3	L4	L5	L6	L7	L8	L9	L10	L11
La	1.4(1)	22.8(7)	25.3(6)	39.0(9)	1.3(2)	16.0(5)	32.6(8)	38(1)	33.6(8)	n.m. ^c	n.m.
Ce	2.5(2)	43(1)	48(1)	74(1)	5.3(6)	32.7(9)	65(1)	80(2)	69(1)	n.m.	n.m.
Pr	0.15(4)	5.4(2)	5.7(2)	8.2(3)	0.4(1)	3.7(2)	7.1(3)	8.6(4)	8.0(3)	n.m.	n.m.
Nd	0.57(2)	20(2)	24(2)	32(2)	1.2(4)	13(1)	27(2)	29(2)	28(2)	n.m.	n.m.
Sm	0.2(1)	4.0(5)	4.8(5)	4.8(6)	0.3(1)	2.4(4)	4.5(5)	4.8(6)	5.8(6)	n.m.	n.m.
Eu	0.7(1)	0.9(1)	1.3(2)	0.7(1)	0.04(3)	0.6(1)	1.2(1)	1.1(2)	1.2(2)	n.m.	n.m.
Gd	0.3(2)	3.2(4)	4.5(5)	3.8(5)	0.4(1)	2.3(3)	3.2(4)	4.2(5)	5.0(5)	n.m.	n.m.
Tb	0.05(2)	0.57(6)	0.73(6)	0.42(6)	0.04(2)	0.40(5)	0.62(6)	0.56(7)	0.83(8)	n.m.	n.m.
Dy	0.28(9)	2.9(3)	4.8(3)	2.6(3)	0.3(1)	3.1(3)	4.7(3)	3.9(4)	5.5(4)	n.m.	n.m.
Ho	0.06(1)	0.60(5)	1.03(6)	0.49(4)	0.04(1)	0.60(4)	0.95(5)	0.87(6)	1.1(6)	n.m.	n.m.
Er	0.17(4)	1.9(1)	3.2(2)	1.5(1)	0.16(5)	2.0(1)	3.3(2)	2.7(2)	3.4(2)	n.m.	n.m.
Tm	0.04(1)	0.29(3)	0.48(4)	0.20(3)	0.02(1)	0.35(3)	0.57(4)	0.45(4)	0.54(4)	n.m.	n.m.
Yb	0.22(6)	2.0(2)	3.3(2)	1.4(1)	0.20(6)	2.2(2)	4.1(2)	3.5(2)	4.0(2)	n.m.	n.m.
Lu	0.04(1)	0.39(4)	0.50(4)	0.24(3)	0.02(1)	0.38(4)	0.60(4)	0.48(4)	0.57(4)	n.m.	n.m.
²³⁸ U	n.m.	43.0(4)	46.5(3)	n.m.	n.m.	n.m.	n.m.	41.8(4)	276(2)	29.1(2)	27.8(3)
²³⁹ Pu ^b	n.m.	0.36(4)	2.22(7)	n.m.	n.m.	n.m.	n.m.	1.70(7)	0.56(1)	0.56(3)	0.59(4)
²⁴⁰ Pu ^b	n.m.	0.012(6)	0.036(9)	n.m.	n.m.	n.m.	n.m.	0.06(1)	0.02(2)	0.018(6)	0.009(5)
²⁴⁰ Pu/ ²³⁹ Pu	n.m.	0.034(8)	0.016(4)	n.m.	n.m.	n.m.	n.m.	0.033(8)	0.027(28)	0.033(11)	0.015(8)

^aLocations Figure 4.2

^bPu concentration calculated based on assumed similar ablation and ionization yields as ²³⁸U

^cNot measured: No data collected for these elements

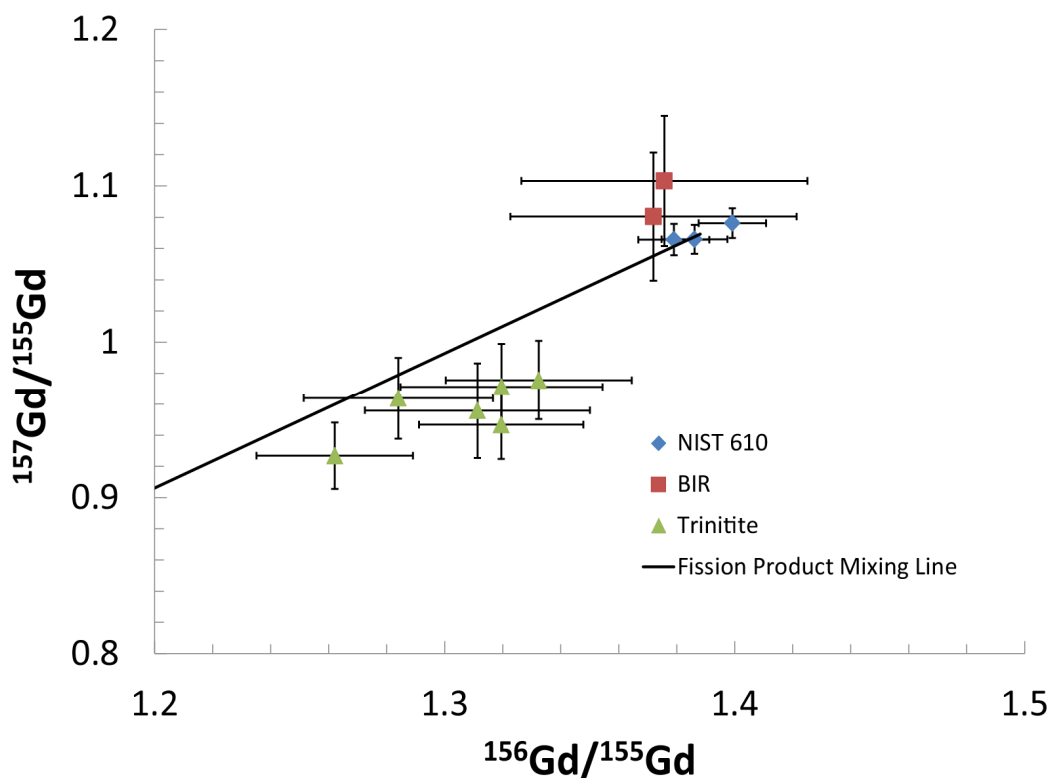


Figure 4.4: Isotopic composition of Gd analyzed with LA-ICP-MS. Mixing line represents line from ^{239}Pu fission production to natural composition. Icelandic basalt (BIR) was used as a secondary standard during analyses. Uncertainties are reported at 2σ .

The Nd isotopic composition for trinitite is distinctive from both the BHVO-2 and Nd-Ames metal solution, listed in Table 4.5, and shows deviations in $^{142}\text{Nd}/^{144}\text{Nd}$, $^{145}\text{Nd}/^{144}\text{Nd}$, and $^{148}\text{Nd}/^{144}\text{Nd}$ which are -1.75ϵ , $+2.24 \epsilon$, and $+1.01 \epsilon$ respectively, with ϵ being deviations in parts in 10^4 . Likewise, the Gd isotopic composition of trinitite, (Table 4.5) also differs from natural materials in $^{155}\text{Gd}/^{160}\text{Gd}$, $^{156}\text{Gd}/^{160}\text{Gd}$, and $^{158}\text{Gd}/^{160}\text{Gd}$ with enrichments of 4ϵ , 4.19ϵ , and 3.48ϵ respectively.

Table 4.5: Nd and Gd isotopic ratios for standards and trinitite sample.

Sample	$^{142}\text{Nd}/^{144}\text{Nd}$	$^{143}\text{Nd}/^{144}\text{Nd}$	$^{145}\text{Nd}/^{144}\text{Nd}$	$^{148}\text{Nd}/^{144}\text{Nd}$	$^{150}\text{Nd}/^{144}\text{Nd}$	^{140}Ce (V)	^{147}Sm (V)
Nd-Ames Metal (n=18) ^a	1.141863(53)	0.512151(18)	0.348403(12)	0.241543(10)	0.236353(9)	-	-
ε (Ames+BHVO-2)	-0.09(59)	-8.23(0.73)	+0.20(73)	+0.02(0.36)	+0.15(39)		
BHVO-2 (n=2) ^a	1.141884(41)	0.512995(33)	0.348389(3)	0.241542(3)	0.236346(2)	0.0013(2)	0.000009(5)
ε (Ames+BHVO-2)	+0.09(59)	+8.23(73)	-0.20(73)	-0.02(36)	-0.15(39)		
Trinitite (n=1) ^a	1.141674(25)	0.512164(9)	0.348474(5)	0.241567(7)	0.236342(10)	0.0012(2)	0.000005(14)
ε (Ames+BHVO-2)	-1.75(60)	-7.98(75)	+2.24(75)	+1.01(38)	-0.32(58)		
Sample	$^{155}\text{Gd}/^{160}\text{Gd}$	$^{156}\text{Gd}/^{160}\text{Gd}$	$^{157}\text{Gd}/^{160}\text{Gd}$	$^{158}\text{Gd}/^{160}\text{Gd}$	^{147}Sm (V)	^{162}Dy (V)	
Gd Solution (n=20)	0.676819(42)	0.9361	0.715875(33)	1.135906(40)	-	-	
ε (Gd soln)	0.0(62)	-	0.0(46)	0.0(35)			
BHVO-2 (n=2) ^b	0.676813(17)	0.936083(47)	0.715846(12)	1.135883(28)	0.00006(1)	0.00022(1)	
ε (Gd soln)	-0.09(67)	-0.18(50)	-0.41(49)	-0.20(43)			
Trinitite (n=1) ^b	0.677100(64)	0.936492(70)	0.715880(42)	1.136301(44)	0.00004(2)	0.00210(20)	
ε (Gd soln)	+4(1)	+4.19(75)	+0.07(75)	+3.48(52)			

^aNd normalized to $^{146}\text{Nd}/^{144}\text{Nd} = 0.7219$

^bGd normalized to $^{156}\text{Gd}/^{160}\text{Gd} = 0.9361$ using standard-sample bracketing

4.5 Discussion

Vertical, textural, and chemical gradations in the trinitite glass are consistent with rapidly quenched melt material that was not sufficiently molten long enough for thermal convection to efficiently mix and homogenize the melt pool. The top 1 mm is suggestive of the source material primarily consisting of potassium feldspar, KAlSi_3O_8 , which agrees with one of the possible glass forms identified in previous studies (Ross, 1948). The smooth texture of the sample's surface alone is not sufficient to determine how the sample was produced. The top-most material could either have been original desert floor which was heated to melting from the thermal radiation of the blast, or it could consist of molten droplets raining from the sky and pooling over the desert floor (Belloni et al., 2011; Ross, 1948). The primarily potassium feldspar composition of the analyzed region does not imply that the top material is solely potassium feldspar, instead, it shows that an original crystal of potassium feldspar was melted to such a degree that it is not visually observable from its surroundings.

The observable increase in vesicle frequency with cross-sectional depth could be due to degassing of water from the beneath the desert floor. The topmost layer of trinitite likely consists of material that rained out from the debris cloud, which was degassed and vesicle free. The initial blast and early deposited material on the desert floor heated pre-existing local water to evaporation. The deposition of airborne material incorporated desert floor sediments and acted as an insulator while the top-most layer quenched to a glass. Degassing likely occurred deeper in the soil with the vapors escaping upward to the quenched surface, becoming trapped and creating

vesicles of increasing size with depth in the sample. An alternative explanation by Belloni et al. (2011) proposed that immediately following the detonation the sand around ground zero is heated to its boiling point. Roughly 2 seconds after the explosion, molten droplets begin to rain down on the boiling sand, forming the top-most portion of trinitite. Trinitite is then instantly quenched by cool air being sucked toward ground zero.

4.5.1 Nd and Gd Isotopic Composition

Deviations in the isotopic ratios of Nd and Gd in trinitite are dominated by two nuclear processes: neutron absorption and fission product generation. Neutron absorption reactions, specifically thermal (~ 0.025 eV) neutron capture, will decrease the abundance of an isotope that has a large neutron capture cross-section, with an accompanying increase in the capture products, while isotopes with comparatively low cross sections would have a reduced probability for neutron capture, thus remaining largely unaffected. Thermal neutrons are specifically mentioned here as fast neutrons (greater than 0.5 MeV) have a lower probability of being captured by nuclei due to their higher energy and must undergo several kinetic collisions with other nuclei before becoming thermalized and able to participate in capture reactions. Fast neutrons can also participate in nuclear reactions outside of neutron capture, however, our calculations specifically require thermal neutrons and, therefore, we are constrained to reporting the thermal neutron fluence of Trinity and not the total neutron fluence.

None of the Nd isotopes are major neutron absorbers, thus neutron absorption reactions do not play a prominent role in any Nd isotopic deviations found in trinitite. However, two Gd isotopes, ^{155}Gd and ^{157}Gd , have large capture cross-sections for thermal neutrons, 6×10^4 b and 2.5×10^5 b respectively. Their resulting capture products, ^{156}Gd and ^{158}Gd , exhibit very small capture cross-sections for thermal neutrons, 1.8 b and 2.2 b respectively, which are too low to experience significant depletions, resulting in enrichments in ^{156}Gd and ^{158}Gd which can be directly correlated with depletions in ^{155}Gd and ^{157}Gd .

Fission also changes the Nd and Gd isotopic ratios due to decay of neutron-rich fission products. Trinity's ^{239}Pu fast fission does not immediately produce significant stable Nd and Gd isotopes (highest yield being 0.1% and 0.001% respectively (Chadwick et al., 2011)), however, after subsequent beta decays, stable isotopes are produced with yields found in Table 4.6. Fission produced isotope yields alone are not sufficient to predict deviations in isotopic ratios. To predict isotopic ratio deviations the difference between the isotopic composition of fissioned material and natural material must be taken into account. If a fission event produces isotopes in similar abundances to natural material at most a small deviation will be observed. For example, $^{146}\text{Nd}/^{144}\text{Nd}$ in natural material is assumed to be 0.7219, however, in ^{239}Pu fission the ratio is 0.6669, resulting in a maximum deviation of $-762 \text{ } \epsilon$. However, if the fission event produces isotopes that are greatly different than natural material a large deviation will be observed. For example, $^{155}\text{Gd}/^{160}\text{Gd}$ in most natural material is assumed to be 0.6768, however, the ratio produced in ^{239}Pu fission is 13.13, resulting in a maximum deviation of $+184,000 \text{ } \epsilon$.

Table 4.6: List of independent and cumulative yields of lanthanoids of interest (Jackson, 2008).

	Independent Yield (%)	Cumulative Yield (%)	Initial Isotope	Lifetime (minutes)
¹⁴² Nd	2(1) x 10 ⁻¹⁰	1.2(7) x 10 ⁻⁶	¹⁴² Pr	2 x 10 ³
¹⁴⁴ Nd	2.8(9) x 10 ⁻⁹	3.69(3)	¹⁴⁴ Ba	6 x 10 ⁵
¹⁴⁵ Nd	4(2) x 10 ⁻⁶	3.00(2)	¹⁴⁵ La	3 x 10 ¹
¹⁴⁶ Nd	8±5 x 10 ⁻⁵	2.46(1)	¹⁴⁶ Ce	3 x 10 ¹
¹⁴⁸ Nd	7±4 x 10 ⁻³	1.658(6)	¹⁴⁸ Ce	3 x 10 ⁰
¹⁵⁰ Nd	0.10(6)	0.993(5)	¹⁵⁰ Pr	1 x 10 ⁻¹
¹⁵⁵ Gd	3(2) x 10 ⁻⁷	0.21(2)	¹⁵⁵ Pm	4 x 10 ⁶
¹⁵⁶ Gd	7(2) x 10 ⁻⁷	0.154(6)	¹⁵⁶ Pm	3 x 10 ⁴
¹⁵⁷ Gd	3(2) x 10 ⁻⁵	0.106(8)	¹⁵⁷ Sm	1 x 10 ³
¹⁵⁸ Gd	2(1) x 10 ⁻⁴	0.06(1)	¹⁵⁸ Sm	5 x 10 ²
¹⁶⁰ Gd	1.1(7) x 10 ⁻³	0.016(5)	¹⁶⁰ Eu	9 x 10 ⁻¹

Maximum deviations can only be observed when the fission event was of such magnitude that the element's natural mass has been overwhelmed with fission produced material and has a pure fission composition. Thus, both the yield and isotopic composition of the fissioned material must be considered when predicting deviations in isotopic composition of fallout material. Lower concentrations of lanthanoids in natural material are more sensitive to both fission isotope generation and neutron capture due to the lower number of atoms available to dilute the fissionogenic signature. Therefore, we would expect to observe the most pronounced altered isotopic abundances in elements that are both low abundance in nature and produced in high yields via fission; both criteria that are met by Nd and Gd.

There is a noticeable difference in time domains of neutron lifetimes (on the order of tens of seconds from Bainbridge (1976)) and time necessary for beta decay of fission products to reach stable lanthanoid isotopes (hours - Table 4.6). This difference in time enables a simplifying assumption that neutron capture only

occurred on naturally occurring material, essentially no fission product lanthanoids were available or participated in neutron capture. For example, ^{157}Gd has an independent fission yield of $3 \times 10^{-5}\%$, whereas the majority of mass 157 isotopes are produced as ^{157}Sm ($t_{1/2} = 8.03$ minutes) with a yield of $\sim 0.1\%$. It takes approximately 160 minutes for all ^{157}Sm to beta decay to ^{157}Gd , by which time neutrons are no longer available for capture. Immediately produced lanthanoid fission product nuclei can also be assumed to not participate in neutron capture reactions due to their neutron heavy structure and relatively low capture cross sections in comparison to the naturally stable lanthanoids. The lanthanoids produced through fission with high immediate yields are so neutron rich that they all have short half-lives, on the order of minutes, and undergo β^- decay. With the neutron pulse being on the order of seconds and the half-lives on the order of minutes, it can be assumed that none of the lanthanoids immediately produced via fission absorb any neutrons. Therefore, the only lanthanoids able to absorb neutrons were already present in the natural source material.

Having neutron absorption occur prior to β -decay of neutron-rich fission products enables an iterative modeling process to determine the total neutron fluence the trinitite sample experienced. The isotopic composition of Gd and Nd can also be used to determine whether ^{235}U or ^{239}Pu was the fissile material, based on their distinctive fission product isotopic composition. The iterative process begins by determining the total number of atoms for each isotope initially present and then determining the effect of unknown neutron fluence on the isotopic composition using the following equation:

$$N_{x+1}^c = N_{x+1}^o + (N_x^o * \sigma_c^x - N_{x+1}^o * \sigma_c^{x+1}) * \Phi \quad (4-1)$$

where N_x^o represents the original atoms of isotope x, N_{x+1}^c the resulting atoms of isotope x+1, σ_c^x is the neutron capture cross section of isotope x in cm^2 , and the total neutron fluence is Φ .

Fission products are introduced according to their cumulative yields using the general equation:

$$N_x^f = N_x^c + \rho_x^{cum} * \text{Fission Events} \quad (4-2)$$

where N_x^f and N_x^c represents post-fission and post-neutron capture atoms, respectively, and ρ_x^{cum} represents the cumulative fission yield of isotope x. The number of fission events is increased until the modeled isotopic ratios are of similar magnitude as the measured ratios from trinitite. Both equation steps are repeated in an iterative process until a best fit line has been reached.

As previously mentioned, a low capture cross section for thermal neutrons results in Nd isotopes having low sensitivity to neutron fluence, and therefore are not ideal for determining the level of neutron fluence produced by the Trinity detonation. With the larger neutron capture cross-sections in Gd, the neutron fluence can be back-calculated based on Gd isotopic ratios. The neutron fluence can be calculated in two ways: the iterative process previously detailed or by using Eq 4-3:

$$\Phi_N = \frac{\left[\left(\frac{^{158}\text{Gd}}{^{157}\text{Gd}} \right)_t - \left(\frac{^{158}\text{Gd}}{^{157}\text{Gd}} \right)_n \right]}{\sigma_{157} \left[1 + \left(\frac{^{158}\text{Gd}}{^{157}\text{Gd}} \right)_n \right] + \left[0.25 \sigma_{155} \left(\frac{^{158}\text{Gd}}{^{157}\text{Gd}} \right)_n * \left(\frac{^{155}\text{Gd}}{^{156}\text{Gd}} \right)_n \right]} \quad (4-3)$$

Eq. 4-3 was derived by Eugster et al. (1970) with Φ_N representing thermal neutron fluence in n/cm^2 , the subscripts t and n represent trinitite and natural, and σ_x is the thermal neutron capture cross section for their respective isotopes.

The iterative process gives a fluence value of $(1.4 \pm 0.2) \times 10^{15} \text{ n/cm}^2$ (all errors cited at 2σ), which is on the lower end of the values predicted by Parekh et al. (2006), while calculations based on Gd ratios results in a fluence of $(9.468 \pm 0.002) \times 10^{14} \text{ n/cm}^2$. The differing uncertainties are a product of calculating the total mass of Gd experimentally measured ion current from the faraday cup for the iterative process. This signal has a greater uncertainty due to fluctuations in the ion beam compared to the uncertainty of the isotope ratio pairs, which constrain the ratio calculation method. The discrepancy between these two fluence values could be due to the ratio method not accounting for fission product interference, which would reduce the impact of neutron capture on $^{155}\text{Gd}/^{156}\text{Gd}$ and $^{157}\text{Gd}/^{158}\text{Gd}$ given the greater production of ^{155}Gd and ^{157}Gd compared to ^{156}Gd and ^{158}Gd respectively.

Trinity's fissile material can be determined by looking at the isotopic ratios of Gd in Fig. 4.5. The isotopic ratios, which would be obtained from fissioning either ^{235}U or ^{239}Pu , are similar with regards to $^{156}\text{Gd}/^{160}\text{Gd}$, $^{157}\text{Gd}/^{160}\text{Gd}$, and $^{158}\text{Gd}/^{160}\text{Gd}$. However, a noticeable depletion in $^{155}\text{Gd}/^{160}\text{Gd}$ is observed relative to modeled predictions. Based on scaling ^{239}Pu and ^{235}U fissionogenic isotopic ratios to trinitite, ^{235}U fission would have resulted in +12 ϵ enrichment in $^{155}\text{Gd}/^{160}\text{Gd}$ while ^{239}Pu would have resulted in +5.8 ϵ . Both possible fissile materials show an enrichment above what is actually observed in this trinitite sample for ^{155}Gd , however, the lower limit for ^{239}Pu is within 3 standard deviations of the measured value whereas ^{235}U is

~22 standard deviations. The closer agreement observed for ^{239}Pu is a strong indicator that ^{239}Pu was the fissile material as opposed to ^{235}U .

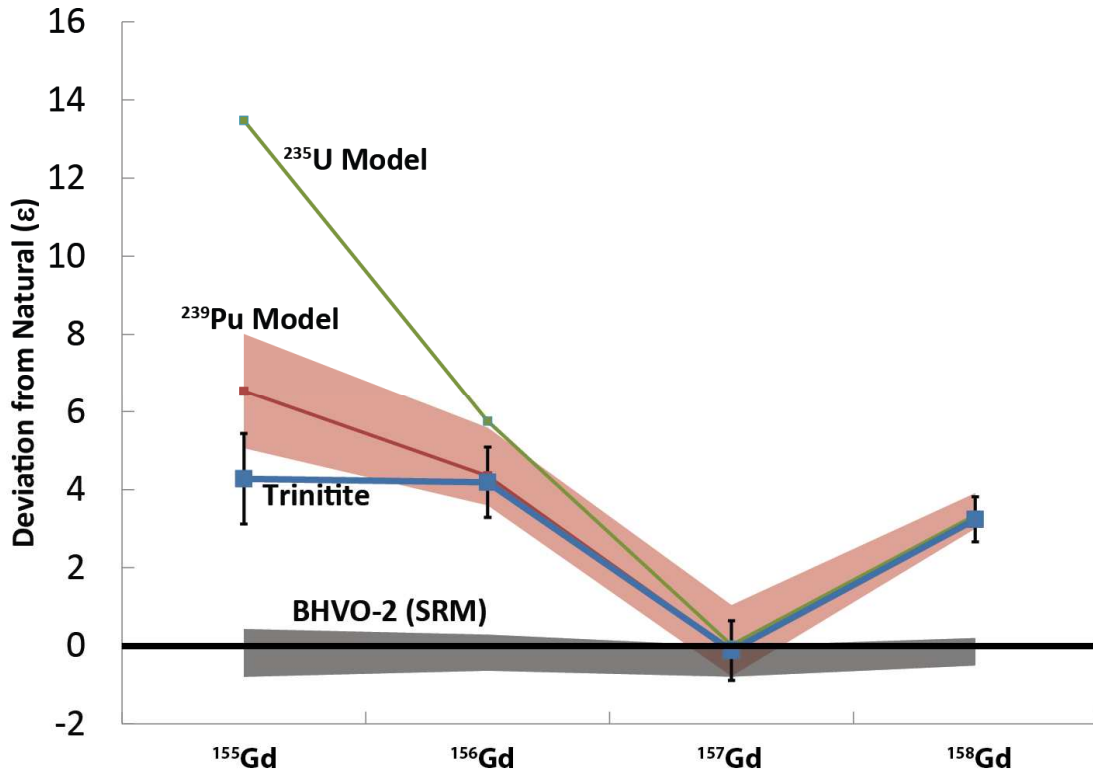


Figure 4.5: Graph of ϵ (10^4) deviation in trinitite for Gd isotopes normalized to ^{160}Gd . Uncertainty reported as 2σ . Trinitite and BHVO-2 were corrected for mass fractionation via sample-standard bracketing with a concentration standard corrected to $^{156}\text{Gd}/^{160}\text{Gd} = 0.9361$. Shaded regions refer to 2σ uncertainty with ^{235}U model uncertainty comparable to ^{239}Pu .

The isotopic ratios of Nd show clear signs of fissionogenic contribution due to enrichments in $^{145}\text{Nd}/^{144}\text{Nd}$ and $^{148}\text{Nd}/^{144}\text{Nd}$ and depletions in $^{142}\text{Nd}/^{144}\text{Nd}$ as shown in Fig. 4.6. As previously mentioned, Nd isotopic deviations occur solely due to yield of fission isotopes which peaks at ^{144}Nd (Table 4.6). The depletion in $^{142}\text{Nd}/^{144}\text{Nd}$ is due to the lack of production of ^{142}Nd compared to ^{144}Nd . The presence of stable ^{142}Ce along the decay path of mass 142 fission products results in no additional production of ^{142}Nd with the exception of the small likelihood of ^{142}Pr production

($10^{-6}\%$) or direct production of ^{142}Nd ($10^{-10}\%$). The scaling fit for the initial fissile material shows strong agreement for ^{239}Pu based on $^{142}\text{Nd}/^{144}\text{Nd}$, $^{145}\text{Nd}/^{144}\text{Nd}$, and $^{146}\text{Nd}/^{144}\text{Nd}$. However, $^{148}\text{Nd}/^{144}\text{Nd}$ fits between the ^{239}Pu and ^{235}U fission curves along with $^{150}\text{Nd}/^{144}\text{Nd}$, which is not distinguishable from natural material. The greater uncertainty in ^{148}Nd and ^{150}Nd isotopic ratios is due to their lower abundances and large mass differences compared to the mass fractionation correction ratio, and could explain the deviation of trinitite values from the ^{239}Pu fission curve.

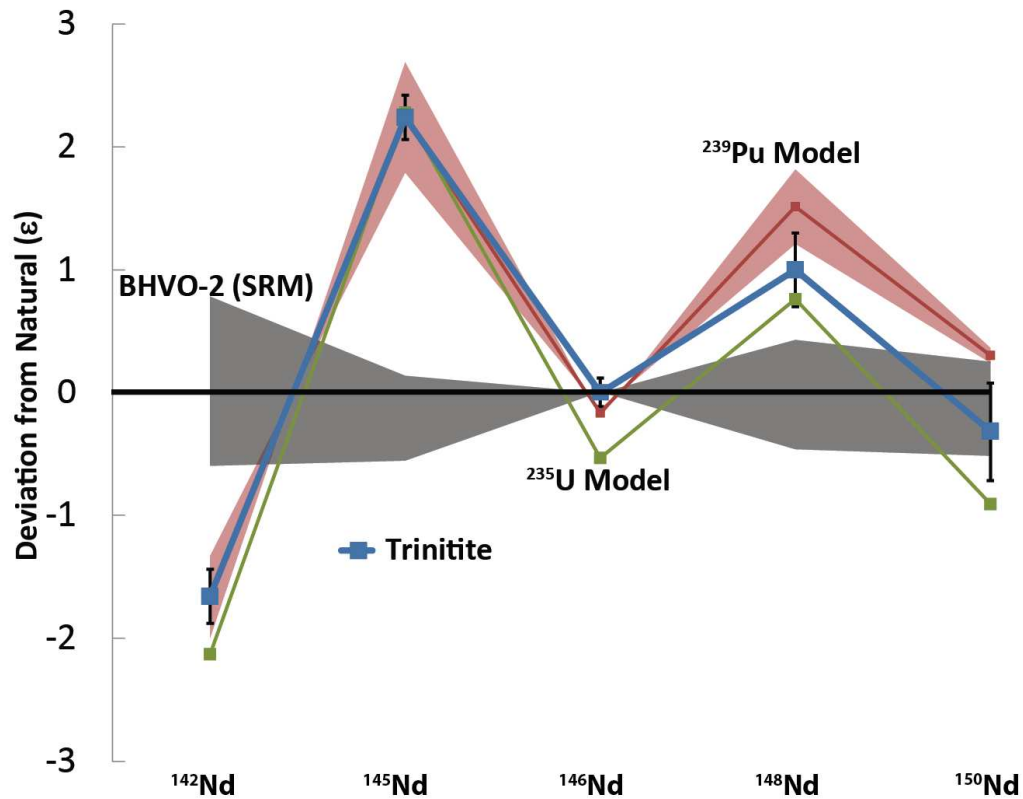


Figure 4.6: Graph of ϵ (10^4) deviation in trinitite for Nd isotopes, normalized to ^{144}Nd , from an average value of Nd-Ames metal and BHVO-2. Uncertainty reported as 2σ . BHVO-2 ratios are shown compared to the averaged natural value to show instrumental precision. Interferences in BHVO-2 and trinitite were observed at ^{140}Ce signal <1 mV and ^{147}Sm $<10^{-3}$ mV. Results for ^{142}Nd are corrected for ^{142}Ce interference. All isotopic ratios are corrected to $^{146}\text{Nd}/^{144}\text{Nd} = 0.7219$. Shaded regions refer to 2σ uncertainty with ^{235}U model uncertainty comparable to ^{239}Pu .

Conversely, $^{150}\text{Nd}/^{144}\text{Nd}$ does not show any signs of enrichment, which was expected, given that ^{239}Pu fission production would yield an isotopic ratio of 0.269 ± 5 , greater than the measured natural isotopic ratio of 0.236353 ± 9 (Table 4.5) for Nd-Ames metal. Assuming ^{239}Pu fission, trinitite should exhibit enrichment in $^{150}\text{Nd}/^{144}\text{Nd}$ compared to natural. Possible explanations for this discrepancy include loss of fission produced ^{150}Nd or a greater production of ^{144}Nd than expected. However, due to the agreement with the other isotopic ratios with the ^{239}Pu model the ^{144}Nd excess is unlikely and the preferential loss of ^{150}Nd compared to the other isotopes is also unlikely to occur. Neutron capture on ^{150}Nd isotopes is unlikely due to the 1 b neutron capture cross section of ^{150}Nd .

Another possible explanation is production of Nd through ^{235}U fast neutron fission, which would give $^{150}\text{Nd}/^{144}\text{Nd}$ and $^{148}\text{Nd}/^{144}\text{Nd}$ isotopic ratios of 0.182 ± 6 and 0.140 ± 3 respectively (Chadwick et al., 2011), lower than the ratios produced from fast fission of ^{239}Pu which are 0.269 ± 5 and 0.449 ± 9 respectively. The trinitite $^{148}\text{Nd}/^{144}\text{Nd}$ and $^{150}\text{Nd}/^{144}\text{Nd}$ ratios plot between the ^{239}Pu and ^{235}U fast fission predictions. Recent studies have also shown that other isotopic systems plot between both ^{239}Pu and ^{235}U fission (Bellucci et al., 2013c). The presence of notable isotopic alterations caused by ^{235}U fission suggests that ^{235}U fission contributed significantly to the overall fission events from Trinity, in addition to the ^{239}Pu which was the primary fissile material. Our model does not assign a quantified value to the ^{235}U contribution, but our results are in agreement with modeled predictions made by Semkow et al. (2006) and noted discrepancies in predicted ^{155}Eu and ^{137}Cs ratios by Bellucci et al. (2013c). Evidence for ^{235}U fission is not apparent in Gd isotopes, due

to the difference in yields of Gd through ^{235}U and ^{239}Pu fission. Fission of ^{239}Pu produces approximately 10x the amount of Gd per fission event compared to ^{235}U (Table 4.6), therefore, the ^{239}Pu events obfuscated any possible ^{235}U contribution.

The ability to determine the fissile material used in a nuclear weapon from the isotopic composition of rare earth elements in post-detonation material provides investigators with a method that is more resistant to artificial emulation with fissile material or common highly radioactive fission products. Results from this method can be used in tandem with other indicators of a fission device to verify or bring into question a previous hypothesis concerning the fissile material used in the device. Focusing specifically on Trinity, the combination of the presence of ^{239}Pu and the non-normal isotopic compositions of Nd and Gd provides compelling evidence that Trinity was a primarily ^{239}Pu based fission device with additional fission contribution from ^{235}U .

4.6 Conclusion

The trinitite sample analyzed in this study has significant variability with depth in terms of major element compositions and vesicle abundance. Signs of the fission event are apparent in the isotopic composition of Nd and Gd with clear enrichments and deviations in normally invariable ratios. Comparison of trinitite Nd isotopic composition with ^{239}Pu and ^{235}U fission predictions yielded evidence of fission of not only ^{239}Pu , which the device was intended to fission, but also significant fission of ^{235}U . Detecting the contribution of unexpected fissile material in Trinity highlights the level of detail that can be obtained using careful sampling and analysis

of post-detonation material. Taking advantage of rapid analysis times achievable with EPMA and LA-ICP-MS, a first pass analysis of any intercepted or post-detonation nuclear material can be performed quickly (2-3 days total) while also identifying suitable samples for more in-depth analyses.

Chapter 5: Sm and Nd Isotopic Composition in Three Research Reactor Fuels

This chapter focuses on the isotopic compositions of Nd and Sm in three spent nuclear fuels from different material test reactors (MTR). The yields of the separation process and original concentrations of the lanthanoids are calculated and compositional differences between the fuel rods discussed. The measured isotopic compositions are compared to the modeled compositions predicted by the Oak Ridge Isotope Generation and Depletion Code (ORIGEN-S) (Hermann and Westfall, 1995).

5.1 Introduction

In nuclear forensics there are two major types of nuclear materials: pre-detonation and post-detonation. Pre-detonation materials can vary tremendously from uranium ores to spent nuclear material. Spent nuclear material is particularly important as it can be used in a radiological dispersion device due to the highly radioactive nature of the contained fission products. Spent nuclear fuel can also contain large amounts of un-fissioned ^{235}U , especially from research reactors which typically operate with ^{235}U enrichment levels above 20 %. Previously research reactors operated at high ^{235}U enrichments, in some cases up to 93%, but in recent years a push has been made to convert to low-enriched fuel (LEU) with enrichments on the order of 20% (IAEA, 2010). With their large amount of fissile material and radioactivity, spent nuclear fuels represent high-profile targets for illicit activities and, therefore, require methods to determine an interdicted fuel rod's provenance and host-reactor's operating characteristics.

Spent nuclear fuel from power reactors has been extensively modeled using multiple versions of ORIGEN, including ORIGEN2.2 and ORIGEN-S (Groff, 1980; Xulubana et al., 2008; Ezure, 1989; Tait et al., 1995). The large amount of radiation produced via fission products must be understood so that nuclear reactor operators know what to expect from each fuel rod and can thus take appropriate handling and shielding steps to protect themselves and others. While codes such as ORIGEN have been benchmarked with power reactor fuels, spent nuclear fuel from research reactors have not been as extensively modeled (Gauld et al., 2006) .

The evolution of spent nuclear fuels can be modeled for power reactors given that setups assuming the use of LEU or HEU fuels can share essentially identical fission product codes with ^{235}U as the primary fission isotope. However, neutron fluences can differ greatly between research reactors and power reactors. The primary reason for this comes from the higher uranium enrichment in research reactors, but another important reason comes from differences in core geometries. Research reactors primarily perform neutron-based experiments and therefore have neutron reflectors and open voids in their reactors to focus neutron fluxes and perform in-core neutron irradiation experiments. These conditions differ greatly from power reactors, which are focused on maximizing the thermal output from fission to generate electricity; therefore, they have more uniform neutron fields compared to research reactors. An important question to answer from a nuclear forensic viewpoint is whether a computer model which is based on an average neutron flux can accurately predict the final composition of spent nuclear fuel from a research reactor.

It is useful to analyze the rare earth elements (REE) to determine the accuracy of ORIGEN-S for describing spent research reactor nuclear fuel. These elements exist on the tail-end of the high-mass fission product curve and contain isotopes with large thermal and resonance neutron cross sections (e.g.: ^{149}Sm and ^{147}Sm , respectively) and ^{148}Nd is characteristically used as a monitor to determine fuel burn-up. The isotopic composition of these elements can provide information as to how well the fuels have been modeled by determining the amount of burn-up and neutron captures.

Typically the Nd and Sm isotopic composition in spent nuclear fuel have been analyzed using HPLC to separate the elements before measurements using MC-ICP-MS (Isnard et al. 2005; Brennetot et al., 2005; Bourgeois et al., 2011). However, HPLC requires a dedicated instrument contained in a glove-box to perform the separations, which can be logistically challenging. In this study we present a simplified method for separating Nd and Sm by using cation exchange chromatography. The samples were chromatographically purified and then analyzed using a Nu Plasma HR MC-ICP-MS at the University of Maryland (UMD) with reference materials that have gone through the same column chemistry serving as mass fractionation correction standards.

5.2 Materials and Methods

5.2.1 Fuel Rod Sampling and Lanthanoid Separation

All acids used in this work were of high-purity quality (either purchased or created using a triple-distillation process at UMD). Resins used were cleaned with 6 M HCl prior to column loading. All sample materials were collected in acid-

cleaned containers and reference material chemistry was performed in a Class 1000 clean lab in the Geology Department at UMD.

Three MTR spent nuclear fuel rods were sampled individually in 2009, 2010, and 2011 at Savannah River National Laboratory (SRNL) Shielded Cells Facility. The sampled fuel rod was placed into a special containment device specifically built for the sampling process and placed inside Shielded Cells. The containment device ensured that no cross contamination occurred between Shielded Cells and the fuel rod samples. MTR spent fuel rods consist of multiple plates of uranium fuel spatially separated from one another and incased in an aluminum cladding. Cores (5 or 6 total sites) spaced evenly down the length of the fuel rod and were drilled deep enough to sample only the top fuel plate. This sampling process provided enough material to obtain representative compositional analyses of the entire fuel rod while minimizing the radioactivity of the processed solution. The resulting material had an average weight of ~1.5 g total with ~0.2 g consisting of the uranium fuel and the rest consisting of the Al-cladding material. This material was dissolved in 100 mL of 50% aqua regia. Blanks were taken inside the containment device for each fuel rod sampling event. These solutions were also analyzed and their concentrations will be reported along with the fuel rod solutions.

For the lanthanoid separation process, ~4 mL were taken from each 100 mL solution and dried down overnight in an oven. The dried samples were then diluted with 2 mL of 2 M HCl. The lanthanoids were separated from the highly-radioactive fission products, uranium, plutonium, and the aluminum-rich matrix using cleaned cation resin (AG-50W x8 200-400 mesh) equilibrated with 2.0 M HCl and contained

in plastic 10 cm x 1.5 cm columns (Environmental Express R1020). After loading the samples onto the columns with 2 mL of 2 M HCl the resin was then washed with 60 mL of 2 M HCl followed by 15 mL of H₂O and 50 mL of 2 M HNO₃. The lanthanoids were finally eluted with 50 mL of 4 M HNO₃. The resulting lanthanoid solution was removed from shielded cells and analyzed using gamma-ray spectroscopy to verify removal of high-activity fission products.

Due to logistical constraints 1 mL aliquots of the six 50 mL solutions (0.1 mL for MTR 2009 due to larger fuel rod sampled mass) were transported to UMD for separation of the individual lanthanoids. This separation was carried out in a non-clean lab environment and involved the use of cleaned AG-50W x8 200-400 mesh resin in the NH⁴⁺ form loaded into a 0.3 cm x 28 cm quartz glass column with 0.15 M, 0.225 M, and 0.53 M alpha-hydroxyisobutyric acid (α -HIBA) buffered to pH 4.7 using NH₄OH.

Once at UMD the separation procedure was performed in a radiation hood and the aliquots were dried and reconstituted in 0.2 mL 0.15 M α -HIBA and loaded onto the column. The Gd cut was collected in 4.25 mL after an 8 mL wash. A subsequent 8 mL wash removed most of the Eu and the lighter lanthanoids were then collected in 10 mL 0.53 M α -HIBA. The column was then treated with 6 M HCl, 18 M Ω H₂O, 7 M NH₄OH, and equilibrated with 0.225 M α -HIBA. The 10 mL containing the lighter lanthanoids was dried down and the α -HIBA digested with aqua regia. The remaining material was reconstituted in 0.2 mL 0.225 M α -HIBA and loaded onto the column. The column was washed with 3 mL, Sm recovered with 3.75 mL, wash with 9 mL, and finally Nd was collected with 4.5 mL. The Gd, Sm, and Nd aliquots were

dried down and the a-HIBA digested using aqua regia. These final solutions were then dried down and reconstituted in 2 mL 0.8 M HNO₃ for Sm and Nd while Gd was reconstituted in 1 mL 0.8 M HNO₃. Smaller aliquots of Nd and Sm were taken for MC-ICP-MS analyses while the entire 1 mL Gd solution was analyzed as-is due to its predicted concentration being too low to require further dilution.

Reference materials for this work consisted of BHVO-2 (a basalt powder reference material) and a 600 ppb (wt%) solution of lanthanoids (Ce through Dy) in 2 M HCl, created via dilutions of concentrated elemental stock solutions (referred to as MBF). Two 0.05 g samples of BHVO-2 were digested using a mixture of HNO₃ and HF with 100 µL of HClO₄ in a sealed 15 mL teflon beaker at 180°C. The solution was then dried down and the samples were reconstituted in 6 M HCl, sealed, and heated for 24 hours. This process was repeated twice and the final dry material was dissolved in 2 mL of 2 M HCl. These two BHVO-2 samples and the MBF sample went through the same separation procedure as the fuel rod samples and were analyzed on the MC-ICP-MS with the BHVO-2 serving as a quality control and the MBF solution as the mass bias factor correction control. A blank was also taken through this process to account for natural lanthanoid contamination.

5.2.2 MC-ICP-MS

Isotopic analyses of Nd and Sm were conducted at the Geology Department of UMD using the Nu Plasma HR MC-ICP-MS with operating parameters reported in Table 5.1. The instrument was coupled to an Aridus I desolvating nebulizer with an uptake rate of 50 µL/min. The sample measurement conditions consisted of 5 blocks of 20 5-second measurements with a 15-second background between each block for

Nd and 4 blocks of 20 7-second measurements (1 sec for Cycle 2) with 15-second backgrounds for Sm. Gd was not analyzed due to no detectable signal for the fuel samples.

Table 5.1: Instrument operational conditions used for MC-ICP-MS analysis of MTR samples.

Nu Plasma HR MC-ICP-MS parameters										
RF Power	1300 W									
Reflected Power	5 W									
Accelerating Voltage	4000 V									
Cool Gas Flow	13 L min ⁻¹ Ar									
Auxiliary Gas Flow	1 L min ⁻¹ Ar									
Sweep Gas Flow ^a	2.75 L min ⁻¹ Ar									
N ₂ Gas	10 mL min ⁻¹ N ₂									
Aspiration Rate	50 μL min ⁻¹									
Collector ^b	H5	H4	H3	H2	H1	Ax	L1	L2	IC 0	L3
Nd	150	148	147	146	145	144	143	142		140
Sm ^c	154 5	152 3	151 2	150 1	149 50	148 9	147 8	146 7		144 5

^aGas flows are set with an Aridus I

^bHx cups refer to Faraday cups, ICx are ion counters

^cSm analyses involved two cycles: Cycle 1 | Cycle 2

Mass fractionation was corrected using the standard-sample-standard bracketing method using the MBF solution as the standard and the BHVO-2 samples as a QC to determine the accuracy of the correction method. For the MBF solution we used $^{146}\text{Nd}/^{144}\text{Nd} = 0.7219$ and $^{148}\text{Sm}/^{154}\text{Sm} = 0.49419$ as the internal correction terms (Wasserburg et al., 1981). Total intensity of the ion beams for samples and MBF deviated by no more than 15 % during the analysis with total Nd and Sm

intensities of ~6.4 V and 2.1 V, respectively on the faraday cups which all had 1×10^{11} ohm resistors.

Isobaric interferences for Nd consist of ^{142}Ce and $^{144,146,148,150}\text{Sm}$ while Sm has interferences from $^{144,146,148,150}\text{Nd}$ and $^{151,152,154}\text{Eu}$. During Nd analysis intensities of ^{140}Ce and ^{147}Sm were monitored and averaged at 3 mV and 0.3 mV, respectively, while Sm interferences were monitored at ^{145}Nd and ^{153}Eu and were ~0.01 mV and ~0.1 V respectively.

5.3 Results

Yields for Nd, Sm, and Gd were calculated by comparing the total ion intensities of the MBF samples to stock solutions of known concentration prepared gravimetrically prior to isotopic analysis. This resulted in yields of $59 \pm 4\%$, $53 \pm 10\%$, and $43 \pm 6\%$ (95 confidence level) for Nd, Sm, and Gd respectively. Yields from BHVO-2 samples fall within these ranges with the noticeable exception of a calculated 80% yield for Gd. Concentrations for Nd and Sm in the MTR fuel solutions and their respective chemistry blank solutions contained in Shielded Cells at SRNL are presented in Table 5.2. Analysis of Gd in the MTR solutions showed no detectable signal.

Table 5.2: Concentration of Nd and Sm ($\mu\text{g/mL}$) in stock solutions at SRNL.

	Nd	Sm
MTR 2009	$6(1) \times 10^3$	$4(1) \times 10^3$
Blank 2009	1.9(4)	0.6(2)
MTR 2010	$2.8(6) \times 10^3$	$1.8(6) \times 10^3$
Blank 2010	6×10^{-3}	1×10^{-3}
MTR 2011	$1.5(3) \times 10^3$	$9(3) \times 10^2$
Blank 2011	0.6(1)	2×10^{-3}
UMD Blank	2 pg	3 pg

The isotopic ratios of the MTR fuel and BHVO-2 were corrected using the mass fractionation correction terms derived from the MBF standards and the results are given in Table 5.3. The overall external reproducibility of the MC-ICP-MS is $\sim 0.02\%$ (95 CL) and the bias introduced via the bracketing correction method is (0.01-0.4) %. Isobaric interferences in the fuel samples were corrected by calculating the isotopic composition of the interfering isotope in the specific fuel sample and using that ratio to correct for the isotopic ratio of interest. For example, ^{150}Sm interference on ^{150}Nd in MTR 2009 was corrected by calculating the $^{150}\text{Sm}/^{147}\text{Sm}$ isotopic ratio in MTR 2009 and using that ratio to correct for ^{150}Sm in MTR 2009 Nd by monitoring the ^{147}Sm signal. All of these corrections were below 1% with the exception of ^{150}Nd in MTR 2009 and all MTR 2009, 2010, and 2011 ^{142}Nd which were 1.39%, 1.37%, 2.92%, and 2.14% respectively.

Table 5.3: Nd and Sm isotopic ratios in MTR samples and natural materials with 2σ uncertainties.

Sample (Nd)	¹⁴² Nd/ ¹⁴⁴ Nd	¹⁴³ Nd/ ¹⁴⁴ Nd	¹⁴⁵ Nd/ ¹⁴⁴ Nd	¹⁴⁶ Nd/ ¹⁴⁴ Nd	¹⁴⁸ Nd/ ¹⁴⁴ Nd	¹⁵⁰ Nd/ ¹⁴⁴ Nd	Nd Beam (V)	¹⁴⁷ Sm (V)	¹⁴⁰ Ce (V)
2009 Fuel	0.00955(1)	0.61910(5)	0.50918(4)	0.46731(6)	0.24410(6)	0.08862(3)	5.38908	0.00303	0.00026
2010 Fuel	0.00724(1)	0.70851(9)	0.55239(2)	0.47651(7)	0.25761(7)	0.09564(3)	4.79983	0.00023	0.00036
2011 Fuel	0.00215(1)	0.93197(9)	0.63756(4)	0.52532(7)	0.29817(8)	0.10887(4)	5.41655	0.00147	0.00008
BHVO-2 1	1.14038(6)	0.51264(2)	0.34861(1)	0.72278(4)	0.24213(3)	0.23718(3)	6.29253	0.00258	0.01340
BHVO-2 2	1.14193(5)	0.51301(2)	0.34839(1)	0.72180(3)	0.24147(2)	0.23621(2)	7.17912	0.00003	0.00142
Ames (n=2)	1.14173(5)	0.51213(2)	0.34840(1)	0.72190 ^a	0.24154(1)	0.23630(2)	6.68823	0.00000	0.00009
MBF (n=3)	1.14173(40)	0.51239(11)	0.34839(5)	0.72190 ^a	0.24156(3)	0.23630(6)	7.03136	0.00002	0.00125
Sample (Sm)	¹⁵¹ Sm/ ¹⁵⁴ Sm	¹⁴⁷ Sm/ ¹⁵⁴ Sm	¹⁴⁸ Sm/ ¹⁵⁴ Sm	¹⁴⁹ Sm/ ¹⁵⁴ Sm	¹⁵⁰ Sm/ ¹⁵⁴ Sm	¹⁵² Sm/ ¹⁵⁴ Sm	Sm Beam (V)	¹⁴⁶ Nd (V)	¹⁵³ Eu (V)
2009 Fuel	0.1676(2)	11.7550(5)	3.5148(7)	0.1732(2)	8.9301(36)	4.5568(6)	2.2088	0.00007	0.7
2010 Fuel	0.3687(3)	21.185(16)	3.4269(11)	0.4646(2)	12.7430(69)	7.8544(13)	2.2828	0.00010	0.1
2011 Fuel	0.6589(5)	22.336(14)	1.5066(3)	0.6811(2)	11.8466(44)	7.9488(7)	2.1911	0.00002	0.2
BHVO-2 1	n/a ^c	0.6599(1)	0.49466(4)	0.60811(8)	0.32472(4)	1.17586(3)	2.16496	0.0008	0.02
BHVO-2 2	n/a ^c	0.65984(9)	0.49452(3)	0.60799(6)	0.32465(4)	1.17574(3)	2.18286	0.0001	0.03
Standard 1 (n=2)	n/a ^c	0.65922(3)	0.49419 ^b	0.60762(2)	0.32449(4)	1.175459(4)	2.22600	0.0001	0.00005
MBF (n=4)	n/a ^c	0.65937(6)	0.49419 ^b	0.60769(3)	0.32450(6)	1.17549(3)	2.00500	0.00001	0.0003

^a¹⁴⁶Nd/¹⁴⁴Nd = 0.7219 for mass fractionation correction
^b¹⁴⁸Sm/¹⁵⁴Sm = 0.49419 for mass fractionation correction
^cNo ¹⁵¹Sm exists in natural samples

The final abundances for Nd and Sm isotopes incorporated the overall reproducibility, the bracketing bias, and isobaric interferences and are presented in Table 5.4 while the modeled abundances are listed in Table 5.5. The $^{144,146}\text{Sm}$ abundances in the MTR fuels are not reported due to low signal intensities from a combination of low immediate fission yields and the β -decay shielding in $^{144,146}\text{Nd}$ from neutron rich fission products. While ^{142}Nd also has a low immediate fission yield and is shielded by ^{142}Ce , neutron capture on ^{141}Pr produces measureable amounts of ^{142}Nd . Additionally the high level of Eu contamination in the fuel samples makes the calculation of ^{151}Sm impractical for this work and is not reported.

Table 5.4: Isotope abundances of Nd and Sm in the three MTR fuels.

Nd Isotope	MTR 2009	MTR 2010	MTR 2011
^{142}Nd	0.3250(3)%	0.2336(2)%	0.0615(2)%
^{143}Nd	21.073(5)%	22.871(6)%	26.597(6)%
^{144}Nd	34.038(1)%	32.280(1)%	28.539(1)%
^{145}Nd	17.332(2)%	17.831(2)%	18.195(2)%
^{146}Nd	15.907(2)%	15.382(2)%	14.992(2)%
^{148}Nd	8.309(2)%	8.316(3)%	8.509(3)%
^{150}Nd	3.016(1)%	3.087(1)%	3.107(1)%
Sm Isotope	MTR 2009	MTR 2010	MTR 2011
^{147}Sm	39.06(2)%	45.03(4)%	48.58(6)%
^{148}Sm	11.678(4)%	7.284(3)%	3.277(1)%
^{149}Sm	0.576(1)%	0.988(1)%	1.481(1)%
^{150}Sm	29.67(1)%	27.09(2)%	25.77(1)%
^{151}Sm	0.557(1)%	0.784(1)%	1.433(1)%
^{152}Sm	15.140(4)%	16.695(7)%	17.288(6)%
^{154}Sm	3.3225(3)%	2.126(1)%	2.175(1)%

Table 5.5: ORIGEN-S predicted isotope abundances of Nd, Sm, and Gd in the three MTR fuels.

Nd Isotope	MTR 2009	MTR 2010	MTR 2011
¹⁴² Nd	0.222%	0.186%	0.033%
¹⁴³ Nd	22.556%	23.762%	26.469%
¹⁴⁴ Nd	32.117%	30.923%	28.238%
¹⁴⁵ Nd	18.135%	18.344%	18.609%
¹⁴⁶ Nd	15.420%	15.228%	14.960%
¹⁴⁸ Nd	8.291%	8.297%	8.408%
¹⁵⁰ Nd	3.259%	3.260%	3.282%
Sm Isotope	MTR 2009	MTR 2010	MTR 2011
¹⁴⁷ Sm	44.898%	48.721%	51.785%
¹⁴⁸ Sm	4.684%	3.488%	1.047%
¹⁴⁹ Sm	0.942%	1.264%	2.569%
¹⁵⁰ Sm	30.990%	28.233%	25.812%
¹⁵¹ Sm	1.074%	1.172%	1.996%
¹⁵² Sm	15.320%	15.076%	14.705%
¹⁵⁴ Sm	2.092%	2.046%	2.085%
Gd Isotope	MTR 2009	MTR 2010	MTR 2011
¹⁵² Gd	0.08%	0.35%	0.02%
¹⁵⁴ Gd	13.17%	16.59%	11.81%
¹⁵⁵ Gd	4.30%	5.00%	6.31%
¹⁵⁶ Gd	68.84%	63.77%	61.13%
¹⁵⁷ Gd	0.14%	0.23%	0.68%
¹⁵⁸ Gd	13.15%	13.71%	19.52%
¹⁶⁰ Gd	0.32%	0.35%	0.53%

5.4 Discussion

5.4.1 Yields and Blanks

Chemistry blank values for the fuel rod samples are abnormally high when compared to the chemistry blanks from UMD. The fuel rod blanks are on the order of μg compared to pg for UMD blanks which confirms that the separation process did not introduce a notable amount of natural lanthanoids which could have affected the

isotopic signature of the fuel rods. Isotopic measurements of the MTR 2009 and MTR 2011 blanks show identical isotopic composition compared to their corresponding fuel samples. The isotopic compositions of the blanks from MTR 2010 were not analyzed due to insufficient signal intensity for faraday cup measurements. The blanks were determined using the ion counters and therefore, their isotopic composition is not provided. This similarity removes the possibility of contamination from natural sources and instead implies that the blanks have been contaminated with the fuel rod samples in a non-uniform way. The MTR 2009 blank has the highest amount of Nd and Sm while the MTR 2010 and MTR 2011 blanks are approximately 10-1000 times lower. At this time it is unclear where the contamination events occurred. The spill event is likely the reason for MTR 2009's higher blank values, however, the similarity of the blank isotopic compositions to their respective fuel samples makes it unlikely that MTR 2009 contaminated MTR 2010 and 2011.

The lack of a Gd signal is unexpected based on the 43% yield of the MBF solution. Possible explanations for this low yield are: the Gd peak was eluted before or after the collection step; or the fuel rod aliquots at UMD have less than the detection limit of 14 pg/mL Gd. The Gd cut elutes over 4 mL of 0.15 M α -HIBA so the possibility that the entire Gd peak was not collected is unlikely, especially when compared with the successful collection of Gd from the BHVO-2 samples. Based on fission yields of Gd compared to Nd and Sm, Gd should have been produced in the sample. Neutron induced fission of ^{235}U produces ~0.05% Gd and ~3% Sm (Chadwick et al., 2011). The concentration of Sm in the MTR samples at UMD was

on the order of micrograms. Therefore, Gd should have been present in the sample at the nanogram level, well above the picogram limit of detection. As of this time the reason for the lack of a Gd signal is most likely due to the loss of the Gd cut from the 2nd stage column. To be certain of this it is recommended that an aliquot be taken from the 50 mL stock solution at SRNL and analyzed for ^{156,158}Gd to determine their concentrations as ^{156,158}Gd are the most abundant isotopes after fission and neutron absorptions are taken into account. However, the logistical restrictions in sampling the 50 mL solution at SRNL does not allow us to obtain results at this time.

5.4.2 Nd and Sm Isotope Abundances

The agreement between the measured Nd isotopic abundance and the predicted abundances using ORIGEN-S is shown in Fig. 5.1. Negative percent differences correspond to the model calculating a larger percent abundance compared to the actual value and the positive differences are produced by the model predicting a lower abundance. Overall the model agrees within 10% to the measured fuel rods with the best fit with MTR 2011. The obvious exception to the previous statement is the high level of percent difference in the measured ¹⁴²Nd abundance. Interestingly the ^{143,145}Nd isotopes are depleted compared to the enriched ^{144,146}Nd isotopes. This relationship can be described by the model not taking into account the appropriate neutron fluence as ^{143,145}Nd have higher thermal capture cross sections compared to ^{144,146}Nd. However, the thermal neutron capture cross sections are low for Nd isotopes in general (325 b and 50 b for ^{143,145}Nd respectively) and ¹⁴¹Pr also has a low thermal neutron capture cross section of ~11 b. These low thermal neutron capture

cross sections could explain why the measured values are so close to the predicted values even with the apparent incorrect neutron fluence calculations.

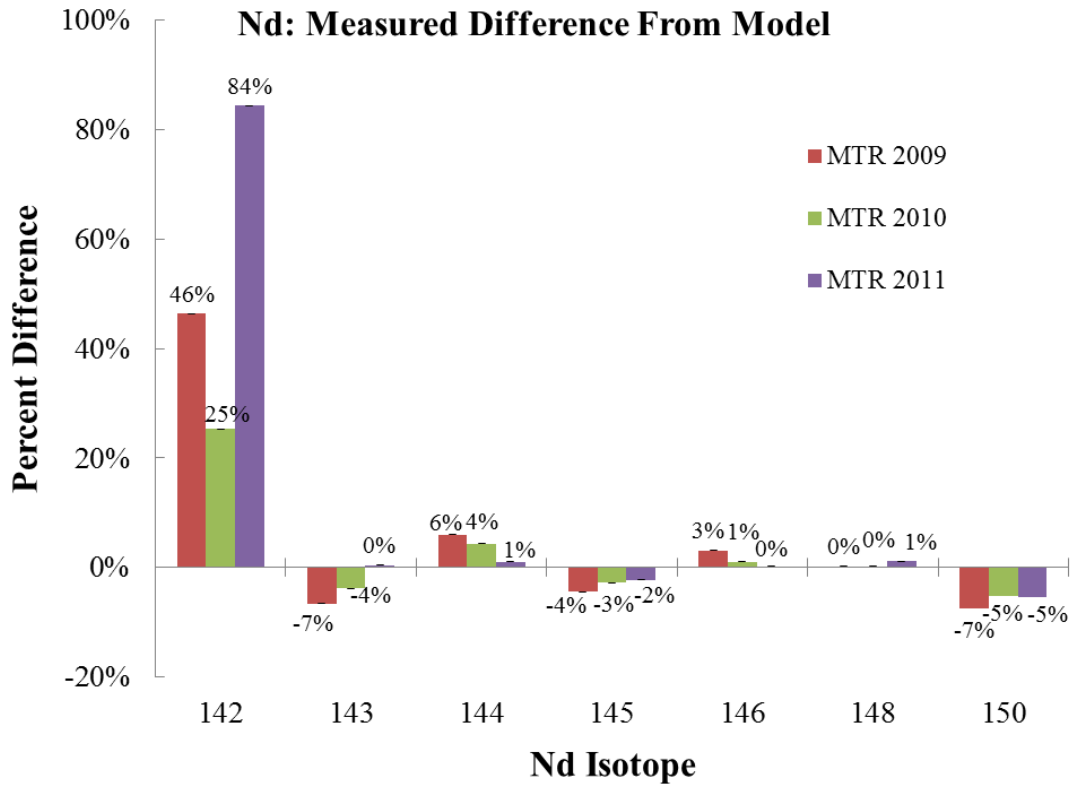


Figure 5.1: Percent difference of Nd isotope abundances compared to ORIGEN-S model.

The agreement between the measured Sm isotope abundances and the predicted abundances using ORIGEN-S is shown in Fig. 5.2. While Nd was modeled fairly well by ORIGEN 2.2, Sm is not nearly as accurate. Discrepancies on the order of 200% different are shown in ^{148}Sm while the other isotopes range from as high as 58% to -42% difference. The uncertainties on ^{151}Sm are possibly due to interference from ^{151}Eu as the ^{153}Eu signal during Sm acquisition was high enough to have a notable effect on the accuracy of ^{151}Sm measurements. The higher discrepancies overall compared to Nd is possibly indicative of more importance having been placed

on accurately determining Nd isotopic composition compared to Sm. Burnup (measure of how much fissile material has fissioned) is routinely measured using ^{148}Nd (Standards 1974) and as ORIGEN-S was originally designed to assist nuclear material handlers having the correct values for burn-up would have been a priority. From a burn-up or radiation safety point of view the Sm isotopes are not important and their lack of importance could explain the model's inaccuracies. As Sm isotopes do not factor into burn-up calculations or present a radiological safety hazard (the beta from ^{151}Sm is very weak) the lower accuracy of the modeled abundances is somewhat expected.

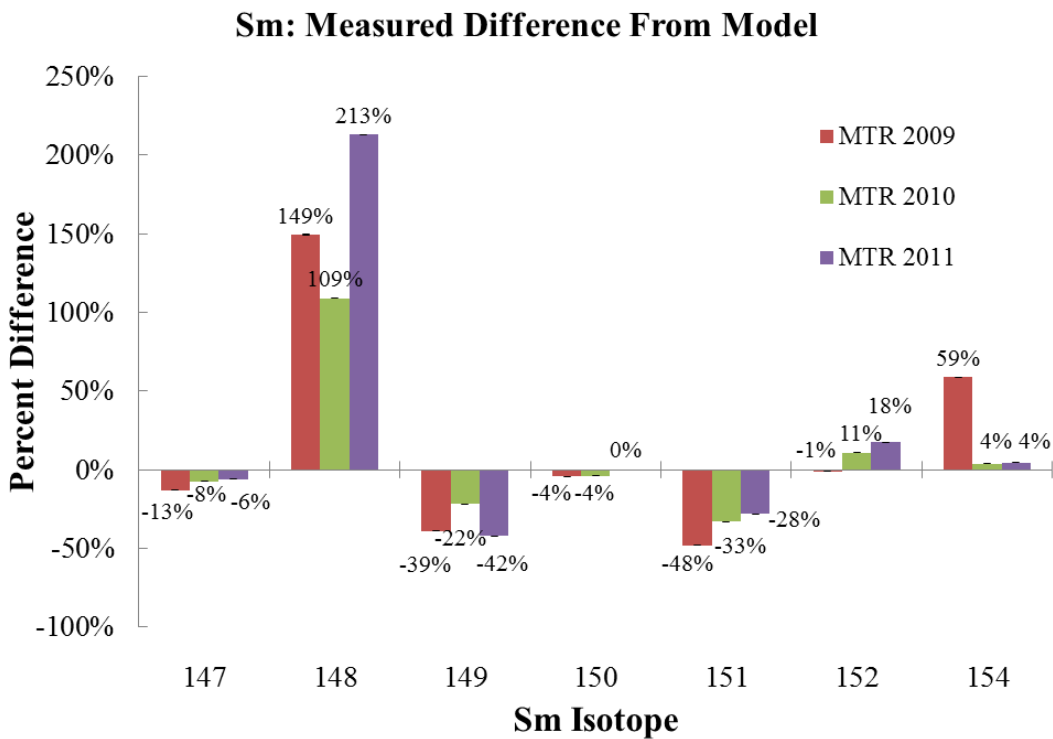


Figure 5.2: Percent difference of Sm isotope abundances compared to ORIGEN-S model.

Similar to the Nd isotope abundances, the Sm isotopes also show signs that the ORIGEN-S model did not accurately calculate effect of the neutron fluence on the samples. The 100-200% difference in ^{148}Sm is likely due to thermal neutron capture on ^{147}Sm that the ORIGEN-S code did not accurately calculate. The ^{149}Sm abundance in the fuel samples is lower than predicted. This is expected due to its high thermal neutron capture cross section, but the lack of a corresponding ^{150}Sm discrepancy is interesting. One would expect the $^{147}\text{Sm} (n,\gamma) ^{148}\text{Sm}$ and $^{149}\text{Sm} (n,\gamma) ^{150}\text{Sm}$ systems to behave similarly due to the larger cross sections on $^{147,149}\text{Sm}$ compared to $^{148,150}\text{Sm}$. However, the ^{150}Sm abundance is in agreement with the model.

The isotope abundances of Sm and Nd in the fuel rods were also directly compared to each other as shown in Fig. 5.3. The direct comparison shows the higher effect of the neutron fluences on isotope abundances in Sm compared to Nd. The Sm isotopes have a larger range of capture cross sections than Nd isotopes and therefore experience greater enrichments and deviations. From a qualitative analysis of the differences in $^{147,149}\text{Sm}$ and $^{143,145}\text{Nd}$ between the three reactors it appears that MTR 2009 experienced the highest neutron fluence followed by MTR 2010 and MTR 2011. The enrichment of ^{142}Nd also supports this hierarchy of neutron fluences and the differences between starting and ending ^{235}U enrichment, listed in Table 5.6, show that the fuels that experienced the largest burnup also experienced the highest neutron fluences as expected.

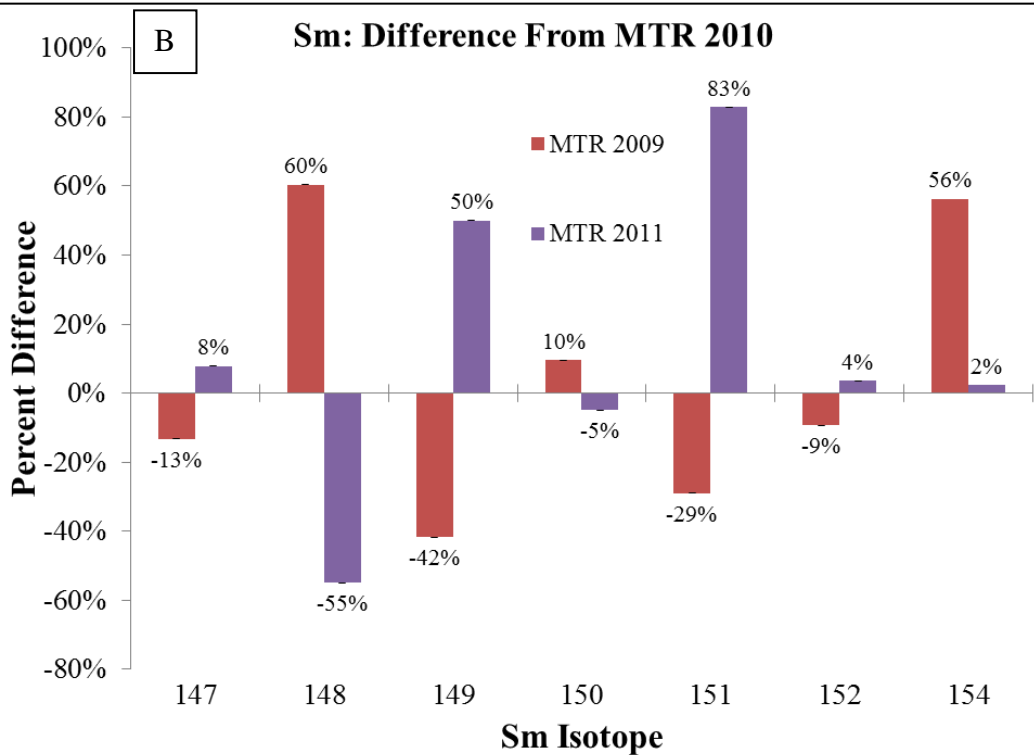
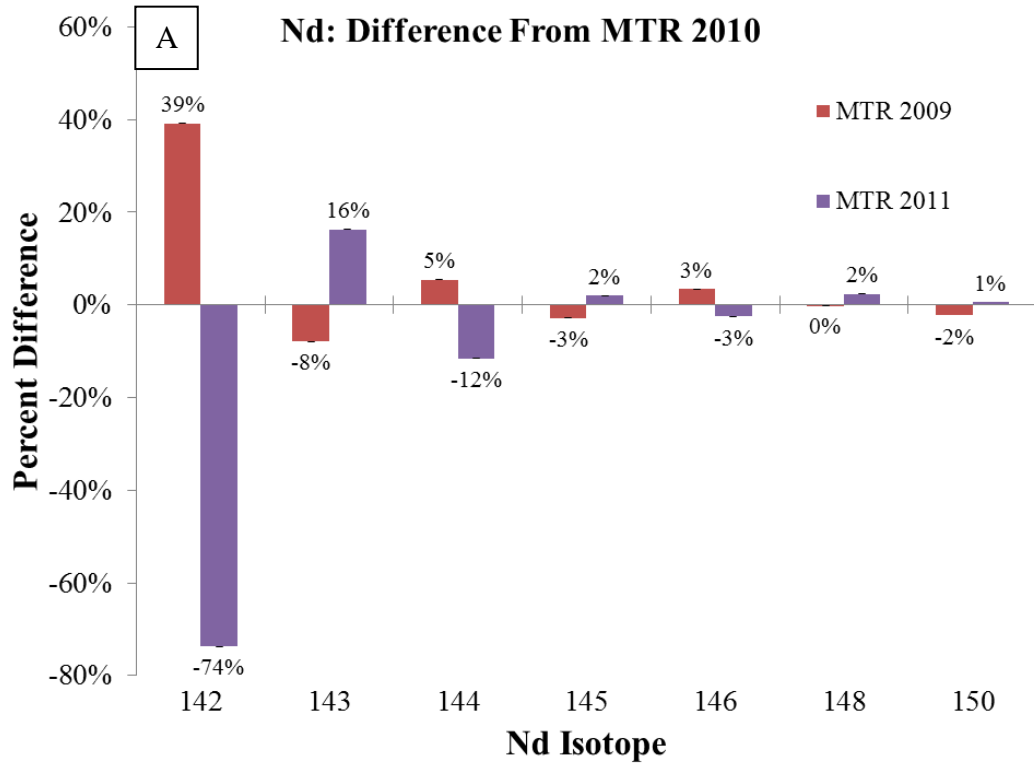


Figure 5.3: (A) Nd and (B) Sm isotope abundance percent differences in MTR 2009 and MTR 2011 compared to MTR 2010.

Table 5.6: Initial and final ^{235}U enrichment of the three MTR fuel rods.

	Initial ^{235}U	Final ^{235}U
MTR 2009	93%	70%
MTR 2010	93%	75%
MTR 2011	45%	33%

As the ORIGEN-S code does not have accurate MTR neutron flux spectrums a more advanced model using MONTEBURNS (Trellue, 2003) (a combination of ORIGEN2.2 and a Monte Carlo N-particle transport code) was used to model the MTR 2010 spent nuclear fuel. This model uses a Monte Carlo approach to calculate an appropriate flux energy spectrum which then initiates fission and neutron capture events. The percent difference of the MONTEBURNS model compared to ORIGEN-S is shown in Fig 5.4 for both Nd and Sm. Overall the uncertainties are reduced across all isotopic ratios with a few exceptions in $^{144,146}\text{Nd}$ and $^{148,152}\text{Sm}$. Notably the largest percent difference in ^{148}Sm has been reduced by half in the new model. Clearly there are still improvements to be made but overall the newer model more accurately predicts the Nd and Sm isotopic composition compared to ORIGEN-S.

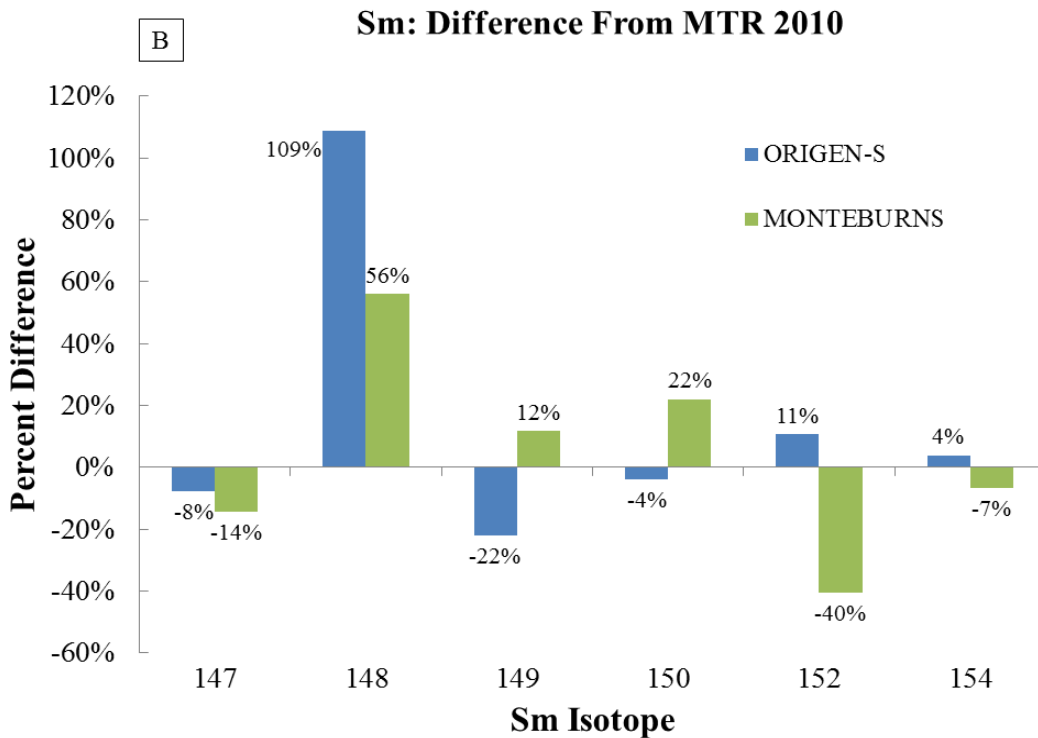
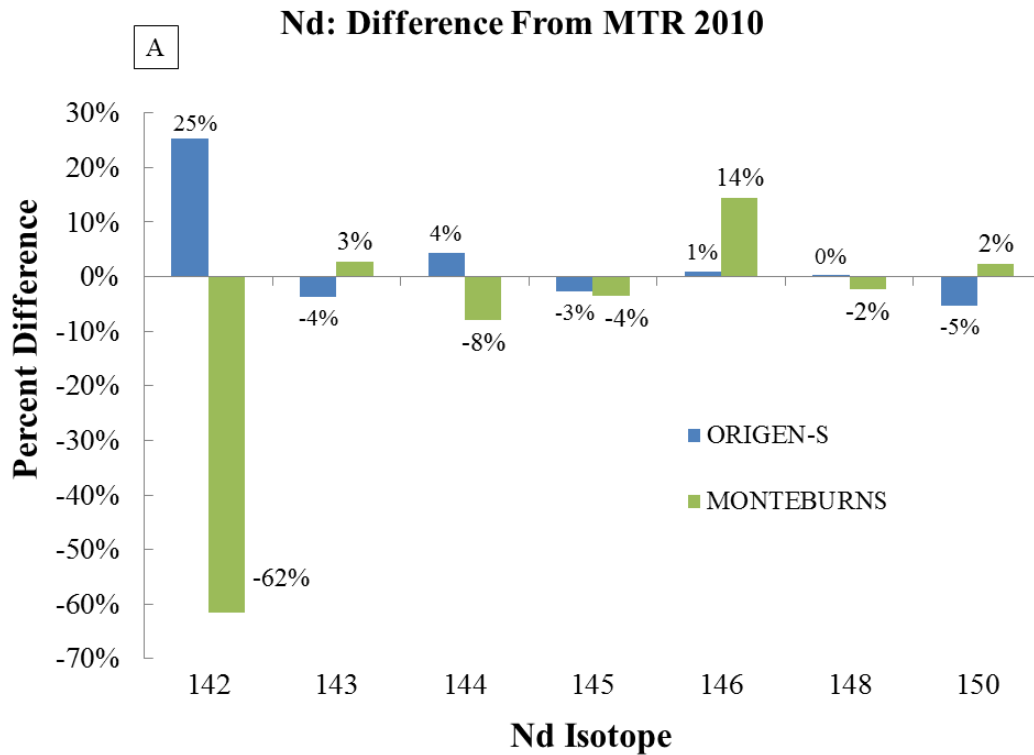


Figure 5.4: Percent difference of measured isotope abundance of (A) Nd and (B) Sm in MTR 2010 compared to ORIGEN-S and MONTEBURNS models.

The modeled predictions for Gd isotope abundances in the three fuel rods are shown in Fig. 5.5. Due to the lack of measured values for Gd the accuracy of the modeled abundances can not be commented on.

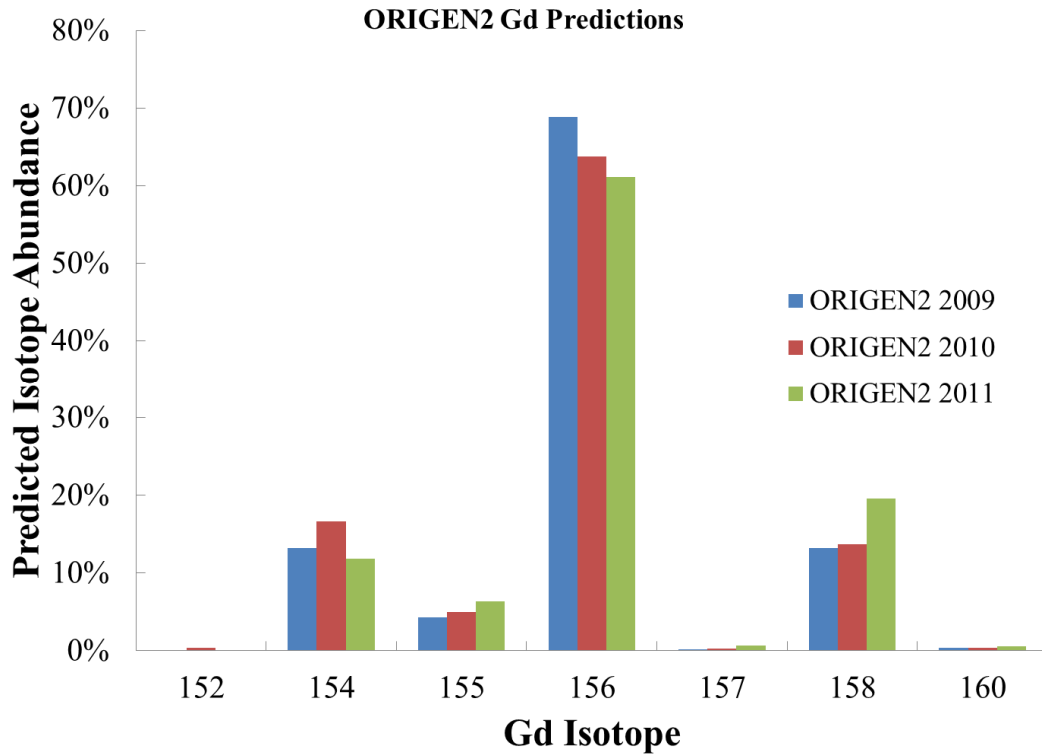


Figure 5.5: Modeled isotopic abundances of Gd in MTR 2009, 2010, and 2011 using ORIGEN-S.

5.4.3 Fluence Calculations

Neutron fluences have been calculated for samples collected at Oklo, Alligator River, the moon, and some meteorites by comparing Gd and Sm isotopic ratios (Maas and McCulloch, 1990; Hidaka et al., 2009; Hidaka, 1995; Hidaka and Masuda, 1988). These methods have all used the relationship between an isotope with a large (>100 b) neutron capture cross section and a low (~1 b) cross section of the resulting isotope. Typically the reactions of choice have been $^{155}\text{Gd} (n,\gamma) ^{156}\text{Gd}$,

^{157}Gd (n,γ) ^{158}Gd , and ^{149}Sm (n,γ) ^{150}Sm . However, for the fuel rod analyses the Gd isotopic data is unavailable and therefore only the ^{149}Sm (n,γ) ^{150}Sm system is available for use. Neutron fluence (ϕt) is calculated by using Eq 5-1 (Maas and McCulloch 1990):

$$\phi t = \frac{\left[\left(\frac{^{150}\text{Sm}}{^{149}\text{Sm}} \right)_m - \left(\frac{^{150}\text{Sm}}{^{149}\text{Sm}} \right)_n \right]}{\left[1 + \left(\frac{^{150}\text{Sm}}{^{149}\text{Sm}} \right)_n \right] * \sigma_{149}} \quad (5-1)$$

Subscripts m and n refer to measured and normal and the σ_{149} representing the thermal (0.025 eV) neutron capture cross section in cm^2 . For the MTR spent fuels, the ratio of $^{150}\text{Sm}/^{149}\text{Sm}$ fission yields for ^{235}U must be used instead of non-fission isotope abundance due to the Sm present being 100% produced from thermal neutron induced fission of ^{235}U .

The results of Eq. 5-1 are found in Table 5.7 and show that MTR 2009 did experience the highest neutron fluence; however, the calculated values do not match the reported total neutron fluences of MTR 2009 and 2010. To determine if the disagreement was due to using $^{150}\text{Sm}/^{149}\text{Sm}$ the fluences were calculated using $^{147}\text{Sm}/^{148}\text{Sm}$, $^{143}\text{Nd}/^{144}\text{Nd}$, and $^{145}\text{Nd}/^{146}\text{Nd}$ by adjusting Eq. 5-1. With the exception of the consistently high $^{147}\text{Sm}/^{148}\text{Sm}$ method, the values agree within 25% but are all consistently more than two orders of magnitude below the reported values. The very high uncertainties in the fluences from Sm isotopes are due to the modeled uncertainties in $^{148,150}\text{Sm}$. These two isotopes are shielded from production via $^{148,150}\text{Nd}$ resulting in $^{148,150}\text{Sm}$ having very small yields ($\sim 1 \times 10^{-9}\%$) and high relative uncertainties.

Table 5.7: Neutron fluence results using the listed isotopic ratios and Eq. 5-1.

	MTR 2009	MTR 2010	MTR 2011
$^{150}\text{Sm}/^{149}\text{Sm}$	$1(2) \times 10^{21}$	$7(9) \times 10^{20}$	$5(5) \times 10^{20}$
$^{148}\text{Sm}/^{147}\text{Sm}$	$1(2) \times 10^{21}$	$1(1) \times 10^{21}$	$4(5) \times 10^{20}$
$^{146}\text{Nd}/^{145}\text{Nd}$	$1.78(2) \times 10^{21}$	$1.15(1) \times 10^{21}$	$7.07(7) \times 10^{20}$
$^{144}\text{Nd}/^{143}\text{Nd}$	$1.11(1) \times 10^{21}$	$7.80(8) \times 10^{20}$	$2.39(2) \times 10^{20}$
Reported	5.21×10^{23}	3.26×10^{23}	Not Reported

A possible explanation for the low calculated neutron fluences could be due to the neutron fluence having an energy greater than 0.025 eV. Previous studies have also shown that the neutron energy can be estimated by using Eq. 5-2 (modified from Lingenfelter et al., (1972)):

$$\frac{\sigma_x}{\sigma_y} = \frac{\left[\left(\frac{x+1_A}{x_A} \right)_m - \left(\frac{x+1_A}{x_A} \right)_n \right]}{\left[1 + \left(\frac{x+1_A}{x_A} \right)_m \right]} * \left\{ \frac{\left[\left(\frac{y+1_B}{y_B} \right)_m - \left(\frac{y+1_B}{y_B} \right)_n \right]}{\left[1 + \left(\frac{y+1_B}{y_B} \right)_m \right]} \right\}^{-1} \quad (5-2)$$

With A and B referring two different or same elements with different masses, namely the four isotopic systems shown earlier. The ratio of their cross sections should give insight into the energy range of the neutron fluence so that appropriate cross sections can be used in Eq. 5-1. The ratios of $\frac{\sigma_{149}}{\sigma_{147}}$, $\frac{\sigma_{145}}{\sigma_{143}}$, and $\frac{\sigma_{149}}{\sigma_{143}}$ suggested neutron energies well outside the thermal energy range and outside of the reported energy range of the MTR 2010 reactor. Additionally the three ratios calculated energy ranges which were not in agreement, suggesting that this calculation method does not produce accurate values when using such altered materials.

If Eq. 5-2 does not produce accurate values for the fuel samples it is then the equation it is based on (Eq. 5-1) may also not be appropriate for these materials. The

exact cross section value required for Eq. 5-1 to calculate the reported neutron fluence for MTR 2009 and MTR 2010 was based on the results obtained and would require an neutron fluence energy range of 6.25 – 280 eV with all four isotopic systems requiring different energies. Given these results it is likely that Eq. 5-1 is unable to calculate fluences above 1×10^{21} n/cm². A method to calculate the fluence using more advanced mathematical equations is being proposed at SRNL. However, Eq. 5-1 combined with Fig. 5.3 provide a qualitative insight into the neutron fluence hierarchy of these three MTRs.

5.5 Conclusions

A two stage separation technique involving cation exchange chromatography has successfully separated Nd and Sm from three MTR spent nuclear fuels. The isotopic abundances of Nd and Sm are distinctively non-normal and show clear signs of the high neutron fluences produced by the MTRs. Modeled predictions involving the use of ORIGEN-S provide acceptable agreement with Nd isotopes, with the exception of ¹⁴²Nd, but fail to correctly account for neutron absorptions for many of the Sm isotopes. A more complicated model involving MONTEBURNS provides a better fit for Sm but room for improvement still exists. Previous methods for determining the neutron fluence that geologic materials have experienced was unable to accurately calculate the neutron fluences the MTR fuels experienced. Future work will be conducted to create a calculation method to accurately calculate the neutron fluence and energy spectrum the MTR samples have experienced.

Chapter 6: Summary

The goal of this dissertation was to develop a method of isolating pure samples of Nd, Sm, and Gd from other lanthanoids in pre and post-detonation nuclear materials. Logistical constraints on the project required that the method not use any pressurized systems and maintain a small enough apparatus footprint to perform work in Shielded Cells and radiation hoods at SRNL. Samples analyzed include trinitite (post-detonation material) and MTR spent nuclear fuel (pre-detonation material), both of which were analyzed for their isotopic abundances with MC-ICP-MS at SRNL and UMD. This chapter details results from method development and analysis results, and then identifies avenues for further work.

6.1 Lanthanoid Separation Method

A two-stage separation method was developed using cation exchange resin with HCl and HNO₃ acid to isolate the lanthanoids from the matrix elements followed by elution with α -HIBA to individually separate the lanthanoids. This method was developed and implemented successfully for the analysis of trinitite and three MTR spent nuclear fuels. The non-natural isotopic composition of all the samples required minimizing co-elution of neighboring isobaric lanthanoids such as separating Nd from Ce, Pr, Pm, and Sm. To that end only the central region of the lanthanoid elution peaks was collected, which minimized tailing of the neighboring elements (Ce/Pr and Pm/Sm in the case of Nd). Consequently yields for Nd, Sm, and Gd were only ~50%. This selective sampling protocol was effective in all the samples with the exception of Eu contamination in the Sm cut from the MTR fuel rods. However, the

presence of Eu was only a concern on ^{151}Sm and the low overall radiation from the other Eu radioisotopes was low enough to not be a safety hazard.

Although the method was successful, there is notable room for further improvement. The most pressing aspect to improve in future work is increasing the yield of the target lanthanoids. The most effective method to accomplish this involves increasing the separation of the lanthanoid elution peaks. This would require a column longer than 28 cm (while maintaining the current aspect ratio) or further adjusting of the concentration and pH of α -HIBA. Changing the physical dimensions of the column could ultimately result in requiring a pressurized system due to slow elution times and presents a challenge for setup in radiation hoods. Application of α -HIBA concentration gradient elution could be done with non-pressurized columns but the footprint for the column assembly would increase drastically (Zeligman, 1965; Maoliang et al., 1988). In radiation hoods it is paramount to keep the experimental footprint to a minimum due to cramped working areas and air-flow requirements.

Previous studies have shown that HPLC can provide rapid separations of the lanthanoids (Schwantes et al., 2006; Sivaraman, et al. 2002; Wang et al., 1995) while still maintaining good separation of the lanthanoid peaks (Campbell and Buxton, 1970). For our work the use of an HPLC system was ruled out due to logistical reasons. However, future work involving lanthanoid isotopic analyses of spent fuel samples or spent fuel rods would greatly benefit from the increased sample throughput and yields provided by HPLC methods.

6.2 Pre and Post-detonation Material Analyses

6.2.1 Trinitite

Separation of Nd and Gd from a piece of trinitite using the two-stage separation method developed here resulted in the detection of ~0.01% deviations from natural in several isotopic ratios. These deviations in Gd allowed the calculation of the thermal neutron flux that Trinity released. The results agreed well with previous measurements using different isotopic systems (Parekh et al., 2006; Bainbridge, 1976). The deviations in Nd identified the presence of ^{235}U fission along with the expected ^{239}Pu , which was the fissile material used in the Trinity device. Previous studies have identified other signs of ^{235}U fission (Bellucci et al., 2013c) and predicted that ^{235}U could have contributed up to 30% of Trinity's fissions (Semkow et al., 2006). Our observation of an enriched $^{150}\text{Nd}/^{144}\text{Nd}$ is a strong indicator for ^{235}U fission as ^{239}Pu and ^{238}U would produce depletions in $^{150}\text{Nd}/^{144}\text{Nd}$. The only fissile material that could have been present in significant quantities in the Trinity device and produce a positive $^{150}\text{Nd}/^{144}\text{Nd}$ deviation from natural is ^{235}U .

6.2.2 MTR Fuel

The isotopic composition of Nd and Sm was analyzed in three MTR spent nuclear fuel rods using the developed two-stage chromatographic separation method. The isotopic abundances for both elements showed clear deviations from natural materials. Predictions of the isotopic abundances of Sm and Nd from the ORIGEN-S and MONTEBURNS models disagreed with the measured values. The ORIGEN-S model overall had the largest percent differences. The models were able to predict

the isotope abundances of Nd fairly well (<10% differences) with the exception of ^{142}Nd due to its production solely through neutron capture on ^{141}Pr . The models did not predict the isotope abundances of Sm as well as Nd, with percent differences varying from 10% to 200%. The MONTEBURNS prediction performed better than the ORIGEN-S model, however the neutron capture events were still not well constrained with either model.

Attempts to calculate the neutron fluence using methods designed for natural materials was unsuccessful. The fluences calculated were 100x lower than the reported values. Multiple choices of neutron capture isotope pairs did not change the accuracy of the method. Interestingly, the four isotope ratios used in the neutron fluence calculations resulted in good agreement of fluence values. This agreement implies that perhaps this method is incapable of accurately calculating fluences as high as $5 \times 10^{23} \text{ n/cm}^2$ as it was designed for low fluence environments ($\sim 1 \times 10^{15} \text{ n/cm}^2$). Future work at SRNL to develop an improved method of determining the neutron fluence from these MTR spent fuels has been proposed.

6.3 Conclusions

The method developed here resulted in detecting and quantifying the effect of fission and neutron fluences on the isotopic composition of Nd, Sm, and Gd. Deviations ranging from the epsilon level (1 part in 10^4) to 800x natural were measured with high-precision MC-ICP-MS. The information gathered from the isotopic composition of these elements can provide significant aide to nuclear forensic investigators, whether they are analyzing post or pre-detonation materials.

Bibliography

- Angelone, M., F. Spaziani, C. Cremisini, and A. Salluzzo. (2007). Determination of PGE and REE in urban matrices and fingerprinting of traffic emission contamination. In *Highway and Urban Environment*, edited by Gregory M Morrison and Sébastien Rauch, 271-281. Springer Netherlands.
- Atkins, P., and J. de Paula. (2006). *Atkins' Physical Chemistry*. 343. Great Britain: W. H. Freeman and Company.
- Bainbridge, K. T. (1976). Trinity. Los Alamos Scientific Lab., NM USA.
- Baker, J., T. Waight, and D. Ulfbeck. (2002). Rapid and highly reproducible analysis of rare earth elements by multiple collector inductively coupled plasma mass spectrometry. *Geochimica Et Cosmochimica Acta* 66: 3635-3646.
- Belloni, F., J. Himbert, O. Marzocchi, and V. Romanello. (2011). Investigating incorporation and distribution of radionuclides in trinitite. *Journal of Environmental Radioactivity* 102: 852-862.
- Bellucci, J., and A. Simonetti. (2012). Nuclear forensics: Searching for nuclear device debris in trinitite-hosted inclusions. *Journal of Radioanalytical and Nuclear Chemistry*. 293: 313-319.
- Bellucci, J. J., A. Simonetti, C. Wallace, E. C. Koeman, and P. C. Burns. (2013a). Isotopic fingerprinting of the world's first nuclear device using post-detonation materials. *Analytical Chemistry* 85: 4195-4198.
- Bellucci, J. J., A. Simonetti, C. Wallace, E. C. Koeman, and P. C. Burns. (2013b). Lead isotopic composition of trinitite melt glass: Evidence for the presence of canadian industrial lead in the first atomic weapon test. *Analytical Chemistry* 85: 7588-7593.
- Bellucci, J. J., C. Wallace, E. C. Koeman, A. Simonetti, P. C. Burns, J. Kieser, E. Port, and T. Walczak. (2013c). Distribution and behavior of some radionuclides associated with the Trinity nuclear test. *Journal of Radioanalytical and Nuclear Chemistry* 295: 2049-2057.
- Berglund, M. and M. E. Wieser. (2009). Isotopic composition of the elements. *Pure Applied Chemistry* 83: 397-410.

- Bourgeois, M., H. Isnard, A. Gourgiotis, G. Stadelmann, C. Gautier, S. Mialle, A. Nonell, and F. Chartier. (2011). Sm isotope composition and Sm/Eu ratio determination in an irradiated Eu-153 sample by ion exchange chromatography-quadrupole inductively coupled plasma mass spectrometry combined with double spike isotope dilution technique. *Journal of Analytical Atomic Spectrometry* 26: 1660-1666.
- Brennetot, R., A. L. Becquet, H. Isnard, C. Caussignac, D. Vailhen, and F. Chartier. (2005). Optimisation of the operating conditions of a MC-ICP-MS for the isotopic analysis of gadolinium in spent nuclear fuel using experimental designs. *Journal of Analytical Atomic Spectrometry* 20: 500-507.
- Campbell, D. O., and S. R. Buxton. (1970). Rapid ion exchange separations. chromatographic lanthanide separations using a high-pressure ion exchange method. *Industrial & Engineering Chemistry Process Design and Development* 9: 89-94.
- Celo, V., E. Dabek-Zlotorzynska, J. Zhao, I. Okonskaia, and D. Bowman. (2011). An improved method for determination of lanthanoids in environmental samples by inductively coupled plasma mass spectrometry with high matrix introduction system. *Analytica Chimica Acta* 706: 89-96.
- Chadwick, M. B., M. Herman, P. Oblozinsky, M. E. Dunn, Y. Danon, A. C. Kahler, D. L. Smith, B. Pritychenko, G. Arbanas, R. Arcilla, R. Brewer, D. A. Brown, R. Capote, A. D. Carlson, Y. S. Cho, H. Derrien, K. Guber, G. M. Hale, S. Hoblit, S. Holloway, T. D. Johnson, T. Kawano, B. C. Kiedrowski, H. Kim, S. Kunieda, N. M. Larson, L. Leal, J. P. Lestone, R. C. Little, E. A. McCutchan, R. E. MacFarlane, M. MacInnes, C. M. Mattoon, R. D. McKnight, S. F. Mughabghab, G. P. A. Nobre, G. Palmiotti, A. Palumbo, M. T. Pigni, V. G. Pronyaev, R. O. Sayer, A. A. Sonzogni, N. C. Summers, P. Talou, I. J. Thompson, A. Trkov, R. L. Vogt, S. C. van der Marck, A. Wallner, M. C. White, D. Wiarda, and P. C. Young. (2011). ENDF/B-VII.1 Nuclear data for science and technology: Cross sections, covariances, fission product yields and decay data. *Nuclear Data Sheets* 112: 2887-2996.
- Chang, T.-L., Q.-Y. Qian, M.-T. Zhao, J. Wang, and Q.-Y. Lang. (1995). The absolute isotopic composition of cerium. *International Journal of Mass Spectrometry and Ion Processes* 142: 125-131.
- Choppin, G., J. O. Liljenzin, and J. Rydberg. (2002) Mechanisms and Models of Nuclear Reactions. In *Radiochemistry and Nuclear Chemistry*, 3rd ed.; Butterworth-Heinemann; Woburn, Massachusetts p 379.

- Choppin, G. R., and R. J. Silva. (1956). Separation of the lanthanides by ion exchange with alpha-hydroxy isobutyric acid. *Journal of Inorganic and Nuclear Chemistry* 3: 153-154.
- Cohen, A. B. (1971.) Concepts of Nuclear Physics, McGraw-Hill, New York, NY
- Dunford, C. L., and T. W. Burrows. (1999). Online nuclear data service. Upton, NY: Brookhaven National Laboratory.
- Depaolo, D. J., and G. J. Wasserburg. (1976). Nd isotopic variations and petrogenetic models. *Geophysical Research Letters* 3: 249-252.
- Eby, N., R. Hermes, N. Charnley, and J. A. Smoliga. (2010). Trinitite—the atomic rock. *Geology Today* 26: 180-185.
- Eugster, O., F. Tera, D. S. Burnett, and G. J. Wasserburg. (1970). Isotopic composition of gadolinium and neutron-capture effects in some meteorites. *Journal of Geophysical Research* 75: 2753-2768.
- Ezure, H. (1989). Validation of ORIGEN computer code by measurements on nuclear-fuels JPDR-1. *Journal of Nuclear Science and Technology* 26: 777-786.
- Fahey, A. J., C. J. Zeissler, D. E. Newbury, J. Davis, and R. M. Lindstrom. (2010). Postdetonation nuclear debris for attribution. *Proceedings of the National Academy of Sciences* 107: 20207-20212.
- Faure, G., T. M. Mensing. (2005). *Isotopes Principles and Applications*, 3rd ed. Wiley; hoboken, New Jersey, p 200.
- Fujii, Y., A. Iwamoto, T. Fukahori, T. Ohnuki, M. Nakagawa, H. Hidaka, Y. Oura, and P. Moller. (2000). The nuclear interaction at Oklo 2 billion years ago. *Nuclear Physics B* 573: 377-401.
- Gauld, I., S. M. Bowman, B. D. Murphy, and P. Schwalbach. (2006). Applications of ORIGEN to spent fuel safeguards and nonproliferation. Oak Ridge National Laboratory.
- Groff, A. G. (1980). ORIGEN-2: A revised and updated version of the Oak Ridge Isotope Generation and Development Code. *ORNL* 5621.
- Group, London Laboratory Services. (2012). ICPMS Ion Source Region. <http://www.lhsc.on.ca/lab/metals/icpms.htm>: LLSG

- Hermann, O. W., and R. M. Westfall. (1995). ORIGEN-S: SCALE system module to calculate fuel depletion, actinide transmutation, fission product buildup and decay, and associated radiation source terms. *Vol. II, Sect. F7 of SCALE: A Modular Code System for Performing Standardized Computer Analyses for Licensing Evaluation, NUREG/CR-0200, Rev 6.*
- Hermes, R.E., and W.B. Strickfaden. (2005). A new look at trinitite. *Nuclear Weapons Journal* 2: 2-7.
- Hidaka, H., M. Ebihara, and M. Shima. (1995). Determination of the Isotopic Compositions of Samarium and Gadolinium by Thermal Ionization Mass Spectrometry. *Analytical Chemistry* 67: 1437-1441.
- Hidaka, H., and A. Masuda. (1988). Nuclide analyses of rare earth elements of the Oklo uranium ore samples: A new method to estimate the neutron fluence. *Earth and Planetary Science Letters* 88: 330-336.
- Hidaka, H., S. Yoneda, and K. Nishiizumi. (2009). Cosmic-ray exposure histories of Martian meteorites studied from neutron capture reactions of Sm and Gd isotopes. *Earth and Planetary Science Letters* 288: 564-571.
- IAEA. (1975). Le Phenomene D'Oklo. In, *Proceedings of Symposium, Libreville, 23-27 June 1975.*
- IAEA. (2010). Research reactors: purpose and future. IAEA.
- Isnard, H., R. Brennetot, C. Caussignac, N. Caussignac, and F. Chartier. (2005). Investigations for determination of Gd and Sm isotopic compositions in spent nuclear fuels samples by MC ICPMS. *International Journal of Mass Spectrometry* 246: 66-73.
- ISO. (1999). 14644-1: Cleanrooms and associated controlled environments—Part 1: Classification of air cleanliness.
- ITDB. (2013). Incidents of nuclear and other radioactive material out of regulatory control: 2013 fact sheet. IAEA Incident and Trafficking Database.
- Jackson, S. (2008). LAMTRACE data reduction software for LA-ICP-MS. *Laser Ablation ICP-MS in the Earth Sciences: Current Practices and Outstanding Issues. Mineralogical Association of Canada, Short Course Series* 40: 305-307.
- Lamarsh, J. R. (1966.) Introduction to nuclear reactor theory. Addison-Wesley Publishing Company, Boston, MA

- Lingenfelter, R. E., E. H. Canfield, and V. E. Hampel. (1972). The Lunar neutron flux revisited. *Earth and Planetary Science Letters* 16: 355-369
- Loss, R. D., J. R. Delaeter, K. J. R. Rosman, T. M. Benjamin, D. B. Curtis, A. J. Gancarz, J. E. Delmore, and W. J. Maeck. (1988). The Oklo natural reactors - cumulative fission yields and nuclear characteristics of reactor zone-9. *Earth and Planetary Science Letters* 89: 193-206.
- Loveland, W., D., Morrissey., G. Seaborg. (2006). α Decay. In *Modern Nuclear Chemistry*; Wiley; Hoboken, New Jersey,; p 178
- Maas, R., and M. T. McCulloch. (1990). A search for fossil nuclear reactors in the Alligator River Uranium Field, Australia: Constraints from Sm, Gd and Nd isotopic studies. *Chemical Geology* 88: 301-315.
- Maoliang, L., L. Yongxiang, and F. Jingyi. (1988). Ion exchange separation of light rare earths by gradient elution. *Journal of Radioanalytical and Nuclear Chemistry* 123: 613-617.
- Marmier, P. and E. Sheldon. (1969). Physics of nuclei and particles, Volume 1; Academic Press.
- Marsh, S. F. (1967). Separation of lanthanide fission products from nuclear fuels by extraction chromatography and cation exchange for isotope dilution mass spectrometric analysis. *Analytical Chemistry* 39: 641-645.
- Moody, K., I. Hutcheon, and P. Grant. (2005). Nuclear Forensic Analysis. Boca Raton, FL: Taylor & Francis Group.
- Nichols, A. L., D.L. Aldama, M. Verpelli. (2008). Handbook of nuclear data for safeguards: database extensions. IAEA, INDC(NDS)-0534
- Parekh, P. P., T. M. Semkow, M. A. Torres, D. K. Haines, J. M. Cooper, P. M. Rosenberg, and M. E. Kitto. (2006). Radioactivity in Trinitite six decades later. *Journal of Environmental Radioactivity* 85: 103-120.
- Pin, C., and J. F. S. Zalduegui. (1997). Sequential separation of light rare-earth elements, thorium and uranium by miniaturized extraction chromatography: Application to isotopic analyses of silicate rocks. *Analytica Chimica Acta* 339: 79-89.
- Ross, C. S. (1948). Optical properties of glass from Alamogordo, New Mexico. *American Mineralogist* 33: 360-362.
- Rudnick, R. L., and S. Gao. (2003). Composition of the Continental Crust. *Treatise on Geochemistry* 3: 1-64.

- Schwantes, J. M., R. S. Rundberg, W. A. Taylor, and D. J. Vieira. (2006). Rapid, high-purity, lanthanide separations using HPLC. *Journal of Alloys and Compounds* 418: 189-194.
- Semkow, T. M., P. P. Parekh, and D. K. Haines. (2006). Modeling the effects of the trinity test. In, *Applied Modeling and Computations in Nuclear Science. ACS Symposium Series* 142-159.
- Sivaraman, N., R. Kumar, S. Subramaniam, and P. R. V. Rao. (2002). Separation of lanthanides using ion-interaction chromatography with HDEHP coated columns. *Journal of Radioanalytical and Nuclear Chemistry* 252: 491-495.
- Smith, H. L., and D. C. Hoffman. (1956). Ion-exchange separations of the lanthanides and actinides by elution with ammonium alpha-hydroxy-isobutyrate. *Journal of Inorganic and Nuclear Chemistry* 3: 243-247.
- Standards, ASTM. (1974). Part 45, Method E321-69. edited by American Society for Testing and Materials. Philadelphia.
- Strelow, F. W. E. (1959). Separation of thorium from rare earths, zirconium, and other elements by cation exchange chromatography. *Analytical Chemistry* 31: 1201-1203.
- Strelow, F. W. E. (1960). An ion exchange selectivity scale of cations based on equilibrium distribution coefficients. *Analytical Chemistry* 32: 1185-1188. doi: 10.1021/ac60165a042.
- Strelow, F. W. E., Rethemey, R., and C. J. C. Bothma. (1965). Ion exchange selectivity scales for cations in nitric acid and sulfuric acid media with a sulfonated polystyrene resin. *Analytical Chemistry* 37: 106-111.
- Tait, J. C., I. Gauld, and A. H. Kerr. (1995). Validation of the ORIGEN-S code for predicting radionuclide inventories in used CANDU fuel. *Journal of Nuclear Materials* 223: 109-121.
- Trellue, H. R. (2003). MONTEBURNS 2.0. *An Automated, Multi-Step Monte Carlo Burnup Code System, User's Manual Version 2.*
- Wallenius, M., K. Mayer, and I. Ray. (2006). Nuclear forensic investigations: Two case studies. *Forensic Science International* 156: 55-62.
- Wang, Q. Q., F. Gao, L. M. Yang, T. Shi, and Q. L. Xie. (1995). Study of the thermodynamic behavior of rare-earths in the system of R-SO₃H-Alpha-HIBA on HPLC and its application to analytical chemistry. *Microchemical Journal* 52: 236-245.

- Wasserburg, G. J., S. B. Jacobsen, D. J. Depaolo, M. T. McCulloch, and T. Wen. (1981). Precise determination of Sm/Nd ratios, Sm and Nd isotopic abundances in standard solutions. *Geochimica Et Cosmochimica Acta* 45: 2311-2323.
- Wasserburg, G. J., D. A. Papanastass, E. V. Nenow, and C. A. Bauman. (1969). A programmable magnetic field mass spectrometer with on-line data processing. *Review of Scientific Instruments* 40: 288-295.
- Weis, D., B. Kieffer, C. Maerschalk, W. Pretorius, and J. Barling. (2005). High-precision Pb-Sr-Nd-Hf isotopic characterization of USGS BHVO-1 and BHVO-2 reference materials. *Geochemistry Geophysics Geosystems* 6: 1-10.
- Wikimedia Commons (2009). Accessed from Wikimedia Commons in February 2014 from <http://en.wikipedia.org/wiki/File:Trinitite-detail2.jpg>
- Xulubana, V., C. Tippayakul, K. Ivanov, S. H. Levine, and M. Mahgerefteh. (2008). Accuracy evaluation of pin exposure calculations in current LWR core design codes. *Annals of Nuclear Energy* 35: 414-424.
- Zeligman, M. M. (1965). Ion exchange separation of fission product rare earths with alpha-hydroxyisobutyric acid. *Analytical Chemistry* 37: 524-525.